Gradient Modeling with Gravity and DEM

by

Lizhi Zhu

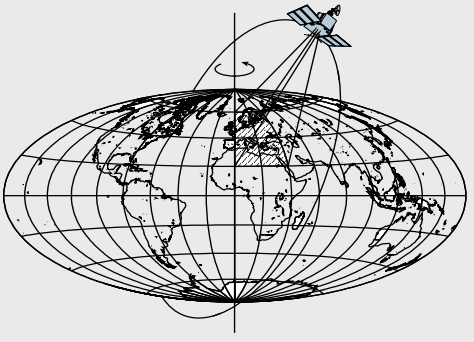

Report No. 483

Geodetic Science and Surveying

The Ohio State University
Columbus, Ohio 43210

June 2007

Gradient Modeling with Gravity and DEM

by

Lizhi Zhu

Report No. 483

Geodetic Science and Surveying

The Ohio State University
Columbus, Ohio 43210

June 2007

ABSTRACT

This study deals with the methods of forward gravity gradient modeling based on gravity data and densely sampled digital elevation data and possibly other data, such as crust density data. In this study, we develop an improved modeling of the gravity gradient tensors and study the comprehensive process to determine gravity gradients and their errors from real data and various models (Stokes' integral, radial-basis spline and LSC). Usually, the gravity gradients are modeled using digital elevation model data under simple density assumptions. Finite element method, FFT and polyhedral methods are analyzed in the determination of DEM-derived gravitational gradients. Here, we develop a method to model gradients from a combination of gravity anomaly and DEM data. Through a solution on the boundary value problem of the potential field, the gravity anomaly data are combined consistently with the forward model of DEM to yield nine components of the gravity gradient tensor. As a result, forward gravity gradients can be synthesized using both geodetic and geophysical data. We use two different methods to process gravity data. One is the regular griding method using kriging and least squares collocation, and the other one is based on fitting splines or wavelet functions. For DEM data, we use finite elements, polyhedra and wavelets or splines to compute the gradients. The second Helmert condensation principle and the remove-restore technique are used to connect DEM and gravity data in the determination of gravity gradients.

Modeling of the gradients thus, particularly at some altitude above ground, from surface gravity anomalies is based on numerical implementations of solutions to boundary-value problems in potential theory, such as Stokes' integral, least-squares collocation, and some Fourier transform methods, or even with radial-basis splines. Modeling of this type would offer a complementary if not alternative type of support in the validation of airborne gradiometry systems. We compare these various modeling techniques using FTG (full tensor gradient) data by Bell Geospace and modeled gradients, thus demonstrating techniques and principles, as well limitations and advantages in each. The Stokes' integral and the least-squares collocation methods are more accurate (about 3 E at altitude of 1200 m) than radial-basis splines in the determination of gravity gradient using synthetic data. Furthermore, the comparison between the modeled data and real data verifies that the high resolution (higher than 1 arcmin) gravity data is necessary to validate the gradiometry survey data.

Ground and airborne gradiometer systems can be validated by analyzing the spectral properties of modeled gradients. Also, such modeling allows the development of survey parameters for such instrumentation and can lead to refined high frequency power spectral density models in various applications by applying the appropriate filter.

PREFACE

This report was prepared for and submitted to the Graduate School of the Ohio State University as a dissertation in partial fulfillment of the requirements of the Ph.D. degree.

The work was supported with sponsorship from the National Geospatial-Intelligence Agency under contract no. NMA401-02-1-2005.

ACKNOWLEDGMENTS

I wish to express my sincere gratitude to my adviser Dr. Christopher Jekeli for proposing this topic of my dissertation and his patient support and guidance to complete this research.
I also want to thank Dr. C.K. Shum and Dr. Ralph R.B. von Frese for reviewing my dissertation.

TABLE OF CONTENTS

CHAPTER 1

INTRODUCTION

1.1 Gravity and Gradiometry

In geodesy, gravity data are used to define the shape of the earth; for exploration geophysics they constrain subsurface density variations to help understand the subsurface structure. Geodesists try to exploit the differences between the measured gravity data and the mathematically based gravity field model. But in geophysics, the aim is to remove global or large scale gravity effects that mask the local mass anomalies that are of real interest. Gravity gradient tensors are the second-rank derivatives of the gravity potential of the Earth, and they are more sensitive to underground mass anomalies near the surface than gravity data since the gravity gradient signal degenerates more quickly with distance than gravity. The gravity gradient data can be used to derive a fine subsurface structure of the Earth once we have a coarse subsurface structure (Hammond and Murphy, 2003).

Since Baron von Eötvös invented his torsion balance on the basis of the Coulomb balance for the purpose of mineral, oil and gas exploration, torsion balance surveys have been carried out in Hungary throughout the last century (Bod et al., 1990). There are more than 60000 torsion balance measurements made in Hungary and 20132 measurements have been processed in a computer database (Toth and Volgyesi, 2003). Due to its cumbersomeness, especially in rough terrain, and the lengthy observation sessions, the torsion balance instrument did not become prevalent in the world.

Now, the modern airborne gravity gradiometer system has been developed, such as the AGG (Airborne Gravity Gradiometer) on the BHP Falcon system (Asten, 2000) and the FTG (Full Tensor Gradient) system from Bell Geospace (Bell Geospace, 2004). The airborne systems can be deployed rapidly over any type of terrain, and this is the main reason for its rapid development in the recent 20 years. A review of the Falcon airborne gravity gradiometer by Asten (2000) showed that lateral wavelengths of 400 m can be routinely resolved, which corresponds to a bandwidth of zero to 0.15 Hz with an average airspeed of 60 m/s, and 150 m resolution also can be achieved in a detailed survey with 50m line spacing for diamond exploration. In these surveys the noise levels of airborne gradient data are typically in the range 7 to 9 E (1 E (Eötvös) $=10^{-9} s^{-2}$), and with a standard deviation as low as ± 5 E.

The airborne GGI (Gravity Gradient Instrument) technology was applied in the field for the first time in 1986 (Jekeli, 1988) by Bell Aerospace, under sponsorship from the US Air Force and the Defense Mapping Agency. This trial achieved a noise level of 30 to

$40\,\mathrm{E}/\sqrt{\mathrm{Hz}}$ due to problems in GPS positioning, temperature control and gyroscope drift. Since the noise level is much higher than required for effective mineral exploration, the trial did not demonstrate this capability for mineral exploration. Usually 7 $\mathrm{E}/\sqrt{\mathrm{Hz}}$ is desirable (Lee, 2001), and the sensitivities for future airborne gradiometers should achieve 1 $\mathrm{E}/\sqrt{\mathrm{Hz}}$ with a resolution of better than 100 m (van Kann, 2004; Matthews, 2002). The problems of sensor noise, sensor drift, and errors produced by aircraft motions (translation and rotation) are typical to every instrument system under design or in operation (van Kann, 2004). Advanced isolation systems have to be used to protect sensing elements from the motion of the aircraft (Tryggvason et al., 2004). In the meantime, quantifying and correcting for the remaining errors is a considerable challenge to obtain better gradient data, and the validation and calibration from external information could aid in identifying these systematic and random errors.

The Gravity field and steady-state Ocean Circulation Experiment (GOCE) mission is scheduled for launch in 2007. This mission is dedicated to estimate the global gravity field up to harmonic degree 200 by measuring the gravitational gradients at the satellite orbit, 250 km above the ground (Albertella et al., 2002). As with the airborne gradiometer system, the satellite system will be subjected to many errors, so that a calibration is necessary to correct them and obtain better quality data (Koop et al., 2001). The validation of the GOCE mission will be done by comparing the measurements with existing independent data or knowledge to assess their quality. At this time, only simulated GOCE data can be tested in this way. Several prelaunch studies were done in the last few years to support the validation objective. In these studies, the gravitational gradient was obtained at the altitude of GOCE through an upward continuation of the ground gravity data (Arabelos and Tscherning, 1998; Sunkel, 2002). Also, digital elevation data and a density model of the crust can be used in forward modeling the gravitational gradient at GOCE altitude (Asgharzadeh et al., 2007). Alternatively, the satellite gravity gradient data can be continued downward to be compared with the ground gravity data or independent gradiometer data (Zieliński and Petrovskaya, 2003). Flying at a very low altitude (250 km) with 96.5° orbital inclination, with drag-free control, and being tracked by GPS and ground laser stations, the satellite gradiometer system can yield a global gravity model with a resolution of 100 km at least (65 km at most) with the accuracy of 2.5 mm in the geoid or 0.08 mGal in the gravity (Balmino, et al., 1998). This resolution does not approach the 1~2 km obtained from airborne gradiometer systems, and similar studies on the validation of airborne gradiometer are needed and provide the main theme and motivation in the present study. Many of the techniques proposed for the validation of GOCE, as well as new ways to combine different data to model the gravitational gradient at the altitude of the airborne gradiometer system are developed and tested, and the results are analyzed.

1.2 Background

Forward gradient modeling is a method to compute the gravitational gradient using known mass anomalies on the basis of Newtonian gravitational potential theory. For example, a constant crust density and a given boundary for the mass of the terrain could be assumed to generate these anomalies. Although it never exists exactly, an elevation

model can be determined quite accurately by SAR (Synthetic Aperture Radar) and LiDAR (light detection and ranging) techniques. The Shuttle Radar Topography Mission data is being used to generate a digital topographic map of the Earth surface with data points spaced every arc second, about 30 meters, with a horizontal accuracy of 20 meters and a vertical accuracy of 16 meters (USGS, 2006). However, the density of the underground masses generally has unknown variations. So the problem of defining the forward gravity gradient model is uncertain to some degree. Since the most accessible density constraint we can provide is in the form of densely sampled gravity data, we could estimate the rough density structure by inverting the gravity data. As an old problem in geophysics, the inversion of gravity data to obtain density is not unique, and many methods yield good results wherein agreement is achieved between gravity anomaly data and other geophysical information obtained by techniques, such as sounding, radar radiometer and magnetometer techniques. An iterative 3-D solution of gravity anomaly data (Cordell and Henderson, 1968), an equivalent source technique (Dampney, 1969), a non-linear optimal method (Loncarevic et al., 1992) and the linear least-squares method (Salem et al., 2004) are the main inversion methods used for the density anomaly under the earth's surface from gravity data. Due to the ill-posed nature of the inversion, however, the density estimates are not stable enough to be used in forward modeling of gravity gradients, though they could still contribute some knowledge on the subsurface structure. In practice, we would use some practical density contrast model and possibly other empirical constraints such as the ratio between the vertical depth and the horizontal extent of the anomalous mass in the model (Li, 2001).

The alternative and simpler method to derive the gravity gradient tensor from gravity data was addressed by Agarwal and Lal (1972), Gunn (1975), and Mickus and Hinojosa (2001). Agarwal and Lal applied a mathematical smoothing operator, $e^{-\lambda\rho^2}$, λ and ρ being the smoothing parameter and radial frequency, respectively, in the theoretical frequency response of the second derivative operation on the field potential and evaluated its vertical-vertical gradient from the Bouguer gravity anomaly. Gunn in his article showed that the gravity and magnetic fields are the result of a convolution of factors which depend on the geometry of the causative body, the physical properties of the body and the type of the field being observed, and gave a relationship between the spectral representation of the gravity and magnetic fields and their respective derivatives. The vertical and horizontal derivatives of potential fields can be calculated from convolutions of factors with appropriate filters. Mickus and Hinojosa computed the Fourier transform of the vertical gravity component and from this determined the spectra of all elements of the gravity gradient tensor. Subsequently, the gradients are computed through an inverse Fourier transform. Though the gradients could thus be simply evaluated from gravity data, this procedure generally does not meet our needs. Since the accuracy of the gradients derived from the gravity signal is dependent on the resolution of the gravity data, usually a few kilometers, gravity alone can not be used for accurate computation of high-frequency gradient signals needed, e.g. in the calibration of gradiometer data.

We can combine gravity and topographic data in order to increase the resolution of the model since the latter are normally available at very high spatial frequency. Since the gravity measurement incorporates topographic effects, we need to extract the topographic effect from the gravity data. This is done on the basis of the well known remove-restore

reduction technique. As an important part of the gravity reduction in geodesy, the topographic effect computations are addressed widely in the literature (e.g., Chinnery, 1961; Forsberg, 1984; Tziavos et al, 1988; Tsoulis, 2001, 2003). Based on assumed density values over the region, the topographic effect can be subtracted from the gravity signal. Topographic-isostatic models (Toth, 1996), surface density variation models (Tziavos et al, 1996), and mass density contrast models for geological layers (Strykowski, 1998; Papp, 1996) have also been applied.

Given densely sampled gravity data and high-resolution elevation data (e.g. a digital elevation model; DEM), we shall develop a consistent integration for the gravity gradient model. The reduction model is based on the assumption of constant crust density and a given boundary. Our goal is to formulate mostly the short wavelength gravity gradient signal, focusing on the application of interpreting the local geophysical information, instead of the long wavelength gravity field.

We may also consider different types of model representation for the gravitational gradient. Nowadays, spherical splines (Schreiner, 1997; Freeden et. al, 1998; Jekeli, 2005) and spherical wavelets (Freeden and Schneider, 1998; Schimidt, et al., 2002; Roland and Denker, 2005) are introduced in geopotential modeling. From a mathematical viewpoint, splines and wavelets can be used for multi-resolution modeling which reflects the different resolutions of input data. Gravity data are usually scattered over a region, so some pre-processing of these scattered data may be necessary. The methods to preprocess these data fall into two major categories, one is the interpolation to a grid, and the other is fitting scattered data with constructive approximations (Freeden et al., 1998) or multiquadrics (Mautz et al., 2005). However, splines and wavelets can be applied with either gridded data or scattered data in modeling the gravitational gradient, and have advantages applied to scattered data over interpolation onto regular grids. In our case, splines and wavelets must be based on the solution of the boundary-value problem in geodesy so that vertical derivatives and upward continuation can be applied. Thus we use spherical splines that are reproducing kernels in a Hilbert space of interpolation functions defined on a unit sphere, and on the basis of potential theory, can be readily extended to three dimensions such that the upward continuation is incorporated to evaluate the gradients at arbitrary altitude. Similarly, wavelet modeling could be incorporated in the solution of the boundary-value problem, so the upward continuation is implemented, e.g. using a generalized Stokes function in the Stokes integral. (This type of representation is not considered in this work and is left for future investigations.)

1.3 Chapter descriptions

This first chapter motivates gravity gradient modeling in geodesy and geophysics and defines the overall scope of this study. The second chapter develops the forward modeling of the gravitational gradient using elevation data. We briefly discuss the right rectangular prism and polyhedral methods as well as other numerical integration methods. Two Fourier transform techniques are also evaluated in the modeling of gravitational gradients from the terrain data. In the third chapter, we describe the forward gradient modeling based on gravity data. The Stokes' integral method, radial-basis spline methods and least-squares collocation are considered. We investigate altitude, data spacing, and signal magnitude for the gradient modeling from gravity data. In the fourth chapter, we

combine the gravity and DEM (digital elevation model) data to model the gravitational gradient. The fundamental ideas are presented in this chapter, including Helmert condensation, the remove-restore technique and the layer effect. We apply this combination method to data in the Parkfield, CA area for which we have high-resolution gravity, elevation, and airborne gradiometer data. The errors of the modeled gradients with respect to the actual gradiometer survey data are analyzed. In the fifth chapter some conclusions are made and the prospects for gradient modeling are discussed.

CHAPTER 2

FORWARD GRADIENT MODEL BASED ON DEM

2.1 Gravitational Gradient

The gravitational potential V at x due to a volume mass v' can be expressed as (Heiskanen and Moritz, 1967)

$$V = G\iiint_{v'} \frac{\rho}{|x - x'|} dv', \tag{2.1}$$

where $|x - x'| = \sqrt{(x_1 - x_1')^2 + (x_2 - x_2')^2 + (x_3 - x_3')^2}$, is the distance between the element point (x_1', x_2', x_3') and the computation point (x_1, x_2, x_3), defined in the local coordinate system with axes pointing in the east, north, and up directions. ρ is the mass density, $dv' = dx_1' dx_2' dx_3'$ is the volume element, and G is Newton's gravitational constant. The gravitational acceleration vector is given by

$$g = (g_1, g_2, g_3)^T = \left(\frac{\partial V}{\partial x_1}, \frac{\partial V}{\partial x_2}, \frac{\partial V}{\partial x_3} \right)^T . \tag{2.2}$$

The gravitational gradient is a tensor

$$\Gamma^V = \nabla g^T = \begin{pmatrix} \frac{\partial g_1}{\partial x_1} & \frac{\partial g_1}{\partial x_2} & \frac{\partial g_1}{\partial x_3} \\ \frac{\partial g_2}{\partial x_1} & \frac{\partial g_2}{\partial x_2} & \frac{\partial g_2}{\partial x_3} \\ \frac{\partial g_3}{\partial x_1} & \frac{\partial g_3}{\partial x_2} & \frac{\partial g_3}{\partial x_3} \end{pmatrix} = \begin{pmatrix} \frac{\partial^2 V}{\partial x_1^2} & \frac{\partial^2 V}{\partial x_1 \partial x_2} & \frac{\partial^2 V}{\partial x_1 \partial x_3} \\ \frac{\partial^2 V}{\partial x_2 \partial x_1} & \frac{\partial^2 V}{\partial x_2^2} & \frac{\partial^2 V}{\partial x_2 \partial x_3} \\ \frac{\partial^2 V}{\partial x_3 \partial x_1} & \frac{\partial^2 V}{\partial x_3 \partial x_2} & \frac{\partial^2 V}{\partial x_3^2} \end{pmatrix} . \tag{2.3}$$

The gradient tensor is symmetric. The trace of the tensor satisfies Poisson's equation, $\nabla^2 V = -4\pi G\rho(x)$. When the density is zero, the right side of this equation is zero and it becomes Laplace's equation. Thus there are only 5 independent components, three off-diagonal and two diagonal components.

Gravity is the acceleration of a resultant force acting on a body at rest on the earth's surface, being the combination of gravitational force and centrifugal force due to earth's rotation. The gravity potential, W, is the sum of the gravitational potential, V, and centrifugal potential, Φ, respectively,

$$W = V + \Phi . \tag{2.4}$$

The gradient vector of W,

$$\tilde{g} = \nabla W = \left(\frac{\partial W}{\partial x_1}, \frac{\partial W}{\partial x_2}, \frac{\partial W}{\partial x_3} \right), \tag{2.5}$$

is the gravity vector. A rotating ellipsoid of revolution is chosen to approximate the earth and it is assumed to be an equipotential surface of a normal gravity field with potential, U. The difference between the actual gravity potential W and the normal gravity potential is denoted by T, such that

$$W = U + T. \tag{2.6}$$

T is called the disturbing potential (Heiskanen and Moritz, 1967, 2-137). The normal gravity potential and its gradient are known for a specified ellipsoid, i.e. GRS80, so we need only to determine the disturbing potential and its gradient from measurements. The gradient disturbance is defined as

$$\delta\Gamma = \begin{pmatrix} \frac{\partial^2 T}{\partial x_1^2} & \frac{\partial^2 T}{\partial x_1 \partial x_2} & \frac{\partial^2 T}{\partial x_1 \partial x_3} \\ \frac{\partial^2 T}{\partial x_2 \partial x_1} & \frac{\partial^2 T}{\partial x_2^2} & \frac{\partial^2 T}{\partial x_2 \partial x_3} \\ \frac{\partial^2 T}{\partial x_3 \partial x_1} & \frac{\partial^2 T}{\partial x_3 \partial x_2} & \frac{\partial^2 T}{\partial x_3^2} \end{pmatrix}. \tag{2.7}$$

Generally, gravity anomaly and elevation data are typical data that can be used to model the disturbing gradient in the local area. Due to lack of crust density anomaly data or its poor resolution, we usually use the constant density assumption for the topographic masses. In addition, we use flat earth approximation for this local gradient modeling. This chapter describes the gradient modeled from the topographic masses with the constant density. The following chapter presents the gradient disturbances modeled from gravity anomaly data. These two models are combined in the fifth chapter using the remove/restore and Helmert condensation techniques. This combination accomplishes modeling the gradient disturbances to meet with the required resolution with respect to real gradient data.

2.2 Gradients from Terrain Elevation

Gravitational gradients are often modeled using elevation data. Usually we make an assumption that the crust density is constant for the whole mass of the terrain, such that we can easily use Newton's integral to derive the gravitation and its gradient for a specified area with some finite elements methods.

One purpose of this study is to derive and analyze the modeling of the gravitational gradient tensor at aircraft altitude or at ground level from elevation data. The forward models based on elevation data can be categorized according to finite elements methods, including right rectangular prisms, polyhedra, and direct numerical integral methods. These methods for the most part (not necessarily the polyhedral method) are based on a grid of regularly spaced elevation data. The grid points determine the elements, and we operate on each element and sum them to get the final result. In the polyhedral method,

we divide the surface of the DEM into triangles where, for a regular rectangular grid, the orientation for the diagonals is specified in some way.

Several studies have shown that the gravitational gradient can be evaluated with different finite elements on the basis of the given data. Dransfield (1994) used the right rectangular prism method to compute the gravitational gradient, mostly for applications in mining and exploration geophysics. Li and Chouteau (1998) reviewed analytical algorithms for computing the gravitational gradient field in all space due to a right rectangular prism, a right polygonal prism and a polyhedron and discussed the validity, singularities and consistency of different algorithms that have been used in the calculation of the gradients at ground level. They also estimated the rounding error due to the finite computer floating precision in the computation of the gravitation and its vertical gradient in three dimensions due to a cubic model using different types of algorithms. They focused on the investigation of gravity and gradient modeling when the computation points are on the ground level of a three-dimensional body with specified geometry.

When a large quantity of elevation data is used in the computation, the conventional algorithms based on the finite elements methods are time consuming, and the Fast Fourier Transform (FFT) technique may be used to compute the terrain effect efficiently for any gravitational field quantity. Parker (1972) demonstrated that a series of Fourier transforms can be used to calculate the potential due to the ocean-bottom topography. Forsberg (1984) outlined the practical computation of the terrain effect on the gravity anomaly, geoid undulation and vertical deflections with the FFT method. The Fourier techniques are based on the linearization and series expansions of the basically nonlinear terrain effect integrals, specifically involving transform of the heights and their powers. Schwarz et al. (1990) summarized the use of FFT techniques in the determination of the terrain effect on the gravity and gradient, and illustrated the accuracies of the FFT method using numerical examples. Tziavos et al. (1988) developed algorithms based on the FFT and used them to study the effect on airborne gravity and gradiometry due to the terrain representation (mass lines or prisms), height data resolution and the number of expansion terms required to approximate the nonlinear terrain effect integrals. Their comparisons of results for height data grid spacings of 0.1, 0.2, 0.5, and 1 km indicated that a 0.5 km grid is necessary to obtain gravitational gradient effects with accuracies of 1 E for a flying altitude of 1 km above the topography. This test reveals that the accuracy of gradient model depends on the resolution of elevation data and the computation altitude.

In this chapter we compare methods of computing the gravitational gradient due to masses of the topography. The chapter is organized as follows. First, the concepts of the gravitational gradient and its model due to terrain masses are introduced. Second, finite elements (rectangular prisms & other polyhedra), Fourier transforms, and direct numerical integral methods are developed. Third, they are compared using a grid of elevation data. Finally, some conclusions are obtained on the basis of a statistical analysis, where the main objective is to compare and analyze different modeling techniques. Since the airborne gradient signals depend on the local mass anomalies, the flat earth approximation is adequate for the gradient modeling from the topographic masses in the local area. For large area, it would be necessary to consider spherical prism for the topography (Smith, et al., 2001; Asgharzadeh, et al., 2007), and this study is beyond the current scope of the research.

2.3 Finite elements

2.3.1 DEM data

Current elevation data sets distributed from USGS' seamless data distribution system include the National Elevation Dataset (NED) and the Shuttle Radar Topography Mission (SRTM) data (USGS, 2006). NED is a seamless raster product derived primarily from US 30-meter Digital Elevations Models (DEMs), along with higher resolution data where available. They are horizontally referenced to the North American Datum of 1983 (NAD83) and vertically referenced to the North American Vertical Datum of 1988 (NAVD88). The resolution is one arc-second (approximately 30 meters). NED data are also available at 1/3 arc-second resolution (approximately 10 meters) for some areas of the conterminous United States. The vertical accuracy of NED is ±7~15 meters. DEMs consist of a geographical grid of regularly spaced elevation values that have been primarily derived from the USGS topographic map series. USGS produces 5 types of elevation data, 7.5-Minute DEMs (1 by 1 arc second spacing, latitude by longitude), 7.5-Minute Alaska DEMs (1 by 2 arc second spacing), 15-Minute Alaska DEMs (2 by 3 arc second spacing), 30-Minute DEMs (2 by 2 arc second spacing), and 1-Degree DEMs (3 by 3 arc second spacing). 7.5-Minute DEMs correspond to the USGS 1:24,000- and 1:25,000-scale topographic quadrangle maps, and are available for all of the U.S. and its territories. They are cast to the Universal Transverse Mercator (UTM) projection system and are referenced to either the North American Datum (NAD) of 1927 (NAD27) or the NAD of 1983 (NAD83). The accuracy of DEMs is dependent on its source and spatial resolution.

SRTM data consist of a raster grid of regularly spaced elevation values derived from the products of the Shuttle Radar Topography Mission (SRTM) sponsored by the National Aeronautics and Space Administration (NASA) and the National Geospatial-Intelligence Agency (NGA) in February 2000. This mission successfully collected Interferometric Synthetic Aperture Radar (INSAR) data over 80 percent of the landmass of the Earth between 60 degrees North and 56 degrees South latitudes. SRTM data contributed the most to a high-resolution digital topographic database of Earth on a near-global scale (Rodriguez et al., 2005). The horizontal datum is the World Geodetic System 1984 (WGS84) and the vertical datum is the mean sea level determined by the WGS84 Earth Gravitational model (EGM96) geoid. The absolute horizontal and vertical accuracy of SRTM data are 20 meters (circular error at 90% confidence) and 16 meters (linear error at 90% confidence), respectively. Since SRTM is the most recent DEM, we use it to model gradients in a local area; and again, we apply these data with the flat-earth approximation.

2.3.2 The right rectangular prisms

For local gradient modeling, one option is to represent the terrain as bounded by a bottom plane (the geoid in planar approximation) and the topographic surface defined by the elevation data (Figure 2.1a). Thus one can set up a local Cartesian coordinate system, with the origin at the center of the bottom plane and axes pointing to the east, north and

up directions, respectively. Specifically, we define the terrestrial mass as bounded by the horizontal $(x_1^{'}, x_2^{'})$ plane, by planes perpendicular to this plane, e.g. $x_1^{'} = a_0$, $x_1^{'} = a_{NM}$, $x_2^{'} = b_0$ and $x_2^{'} = b_{NM}$ (which define the integration area, A, in the $(x_1^{'}, x_2^{'})$ plane, and by a topographic surface, $x_3^{'} = h(x_1^{'}, x_2^{'})$. In practice the surface, $x_3^{'} = h(x_1^{'}, x_2^{'})$ is known only approximately from a collection of data that represent measurements of heights at discrete points. For example, the SRTM (point value) data are on a 30-m grid. The area under consideration is split into $N \times M$ rectangles each of which has an associated elevation at the center of the rectangle from the database and thus defines a right rectangular prism (Figure 2.1b). The horizontal coordinates of the grid point are (a_i, b_i), $i = 0,1,\ldots, NM$. The dimensions of ith prism are defined as Δx_1, Δx_2 and h_i. The computation point, P, is always a point above the terrain since we only study the gravitational gradient outside of the mass.

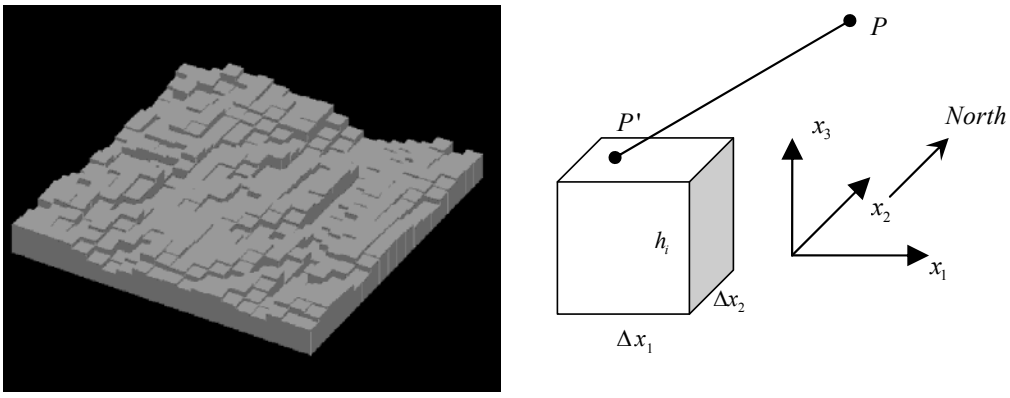

a b

Figure 2.1: The block representation of the terrain (a) and the right rectangular prism (b).

From (2.1) and (2.3), we can readily get the gravitational gradient at P due to the *ith* prism,

$$\Gamma_{jk}^{i} = G\rho \int_0^{h_i} \int_{b_i-\Delta x_2/2}^{b_i+\Delta x_2/2} \int_{a_i-\Delta x_1/2}^{a_i+\Delta x_1/2} \frac{\partial^2}{\partial x_j \partial x_k} \frac{1}{r} dx_1^{'} dx_2^{'} dx_3^{'}, \tag{2.8}$$

where $r = \sqrt{(x_1 - x_1^{'})^2 + (x_2 - x_2^{'})^2 + (x_3 - x_3^{'})^2}$. Performing the differentiation, the in-line gradients are

$$\Gamma_{jj}^{i} = G\rho \int_0^{h_i} \int_{b_i-\Delta x_2/2}^{b_i+\Delta x_2/2} \int_{a_i-\Delta x_1/2}^{a_i+\Delta x_1/2} \frac{3(x_j - x_j^{'})^2 - r^2}{r^5} dx_1^{'} dx_2^{'} dx_3^{'}, \tag{2.9}$$

and the cross gradients are

$$\Gamma_{jk}^{i} = G\rho \int_0^{h_i} \int_{b_i-\Delta x_2/2}^{b_i+\Delta x_2/2} \int_{a_i-\Delta x_1/2}^{a_i+\Delta x_1/2} \frac{3(x_j - x_j^{'})(x_k - x_k^{'})}{r^3} dx_1^{'} dx_2^{'} dx_3^{'}. \tag{2.10}$$

Because of the symmetry of the kernel functions and the constant integration limits, we need to consider only two gradients, Γ_{12}^{i} and Γ_{11}^{i}, when determining analytic expressions for these integrals. Once we have derived these gradients, the other gradients can be obtained by cyclically permuting the indices on the coordinates. Integrating (2.10) with respect to $x_1^{'}$, we get the gradient, Γ_{11}^{i},

$$\Gamma_{11}^{i}(x_1,x_2,x_3)=G\rho\int_0^{h_i}\int_{b_i-\Delta x_2/2}^{b_i+\Delta x_2/2}\frac{(x_1-x_1^{'})}{r^3}\Big|_{x_1^{'}=a_i-\Delta x_1/2}^{a_i+\Delta x_1/2}dx_2^{'}dx_3^{'}. \tag{2.11}$$

We have

$$\int_{x_2^{'}}\int_{x_3^{'}}\frac{1}{r^3}dx_3^{'}dx_2^{'}=\frac{1}{x_1^{'}}\tan^{-1}\frac{x_2^{'}x_3^{'}}{x_1^{'}r}, \tag{2.12}$$

and one can obtain

$$\Gamma_{11}^{i}=G\rho\tan^{-1}\frac{(x_2-x_2^{'})(x_3-x_3^{'})}{(x_1-x_1^{'})r}\Big|_{x_1^{'}=a_i-\Delta x_1/2}^{a_i+\Delta x_1/2}\Big|_{x_2^{'}=b_i-\Delta x_2/2}^{b_i+\Delta x_2/2}\Big|_{x_3^{'}=0}^{h_i}. \tag{2.13}$$

Since we have

$$\Gamma_{12}^{i}=G\rho\int_0^{h_i}\int_{b_i-\Delta x_2/2}^{b_i+\Delta x_2/2}\int_{a_i-\Delta x_1/2}^{a_i+\Delta x_1/2}\frac{\partial^2}{\partial x_1\partial x_2}\frac{1}{r}dx_1^{'}dx_2^{'}dx_3^{'}=G\rho\int_0^{h_i}\int_{b_i-\Delta x_2/2}^{b_i+\Delta x_2/2}\int_{a_i-\Delta x_1/2}^{a_i+\Delta x_1/2}\frac{\partial^2}{\partial x_1^{'}\partial x_2^{'}}\frac{1}{r}dx_1^{'}dx_2^{'}dx_3^{'}, \tag{2.14}$$

From (2.14) the gradient Γ_{12}^{i} is straightforwardly

$$\Gamma_{12}^{i}(x_1,x_2,x_3)=G\rho\int_0^{h_i}\frac{1}{r}\Big|_{x_1^{'}=a_i-\Delta x_1/2}^{a_i+\Delta x_1/2}\Big|_{x_2^{'}=b_i-\Delta x_2/2}^{b_i+\Delta x_2/2}dx_3^{'}. \tag{2.15}$$

Because $x_3>x_3^{'}$, let $x_3-x_3^{'}=\sqrt{\left(x_1-x_1^{'}\right)^2+\left(x_2-x_2^{'}\right)^2}\tan\alpha$. Then we have

$$\int_{x_3^{'}}\frac{1}{r}dx_3^{'}=\int_{\alpha}\frac{-1}{\sec\alpha}\sec^2\alpha d\alpha=-\int_{\alpha}\sec\alpha d\alpha=-\ln\left(\sec\alpha+\tan\alpha\right)\Big|_{\alpha}=-\ln\left(x_3-x_3^{'}+r\right)\Big|_{x_3^{'}}. \tag{2.16}$$

Therefore, (2.15) can be further integrated as

$$\Gamma_{12}^{i}(x_1,x_2,x_3)=-G\rho\ln(x_3-x_3^{'}+r)\Big|_{x_1^{'}=a_i-\Delta x_1/2}^{a_i+\Delta x_1/2}\Big|_{x_2^{'}=b_i-\Delta x_2/2}^{b_i+\Delta x_2/2}\Big|_{x_3^{'}=0}^{h_i}. \tag{2.17}$$

Now we get the other gradients by cyclically permuting the indices on the coordinates,

$$\Gamma_{13}^{i}=-G\rho\ln(x_2-x_2^{'}+r)\Big|_{x_1^{'}=a_i-\Delta x_1/2}^{a_i+\Delta x_1/2}\Big|_{x_2^{'}=b_i-\Delta x_2/2}^{b_i+\Delta x_2/2}\Big|_{x_3^{'}=0}^{h_i}, \tag{2.18}$$

$$\Gamma_{22}^{i}=G\rho\tan^{-1}\frac{(x_3-x_3^{'})(x_1-x_1^{'})}{(x_2-x_2^{'})r}\Big|_{x_1^{'}=a_i-\Delta x_1/2}^{a_i+\Delta x_1/2}\Big|_{x_2^{'}=b_i-\Delta x_2/2}^{b_i+\Delta x_2/2}\Big|_{x_3^{'}=0}^{h_i}, \tag{2.19}$$

$$\Gamma_{23}^{i}=-G\rho\ln(x_1-x_1^{'}+r)\Big|_{x_1^{'}=a_i-\Delta x_1/2}^{a_i+\Delta x_1/2}\Big|_{x_2^{'}=b_i-\Delta x_2/2}^{b_i+\Delta x_2/2}\Big|_{x_3^{'}=0}^{h_i}, \tag{2.20}$$

$$\Gamma_{33}^{i}=G\rho\tan^{-1}\frac{(x_1-x_1^{'})(x_2-x_2^{'})}{(x_3-x_3^{'})r}\Big|_{x_1^{'}=a_i-\Delta x_1/2}^{a_i+\Delta x_1/2}\Big|_{x_2^{'}=b_i-\Delta x_2/2}^{b_i+\Delta x_2/2}\Big|_{x_3^{'}=0}^{h_i}. \tag{2.21}$$

Using (2.13), (2.17)-(2.21), we can compute the gravitational gradients at the point P due to one prism with constant density.

Dransfield (1994) derived similar expression for the cross gradients, except for a negative sign, since he defined the potential with a negative sign. Dransfield's expressions for the in-line gradients include the arctangent terms, and several other terms which do not exist in the results derived here. So his expressions for the in-line gradients do not agree with the above results.

However, the cross and in-line gradients derived here agree with Forsberg's (1984) and Nagy's (2000) formula, except for the sign in the in-line gradient since Forsberg and Nagy put the computation point at the coordinate origin. Putting the computation point at the origin implies a coordinate transformation. After applying this transformation, the expressions derived here are in agreement with Forsberg's and Nagy's formula.

We separately calculate the gravity gradient for each rectangular prism and then sum all of them to obtain the gravitational gradient due to the whole topographic mass in Area A,

$$\Gamma_{jk} = \sum_{i=1}^{NM} \Gamma_{jk}^{i} \,. \tag{2.22}$$

If we choose a different reference (e.g. mean elevation) other than the geoid as the bottom of the prisms, residual gradients can be derived from a residual terrain model (subtracting the reference elevation from original elevation for each grid point) and a reference terrain model. Denoting $\bar{h}$ is the reference elevation, if $\bar{h}$ is constant in the area, thus according to (2.8), the gravitational gradient at P due to the *ith* prism (mean elevation reference) is

$$\bar{\Gamma}_{jk}^{i} = G\rho \int_{\bar{h}}^{h_i} \int_{b_i-\Delta x_2/2}^{b_i+\Delta x_2/2} \int_{a_i-\Delta x_1/2}^{a_i+\Delta x_1/2} \frac{\partial^2}{\partial x_j \partial x_k} \frac{1}{r} dx_1' dx_2' dx_3' \,, \tag{2.23}$$

Comparing (2.23) to (2.8), we have

$$\Delta\bar{\Gamma}_{jk}^{i} = \Gamma_{jk}^{i} - \bar{\Gamma}_{jk}^{i} = G\rho \int_{0}^{\bar{h}_i} \int_{b_i-\Delta x_2/2}^{b_i+\Delta x_2/2} \int_{a_i-\Delta x_1/2}^{a_i+\Delta x_1/2} \frac{\partial^2}{\partial x_j \partial x_k} \frac{1}{r} dx_1' dx_2' dx_3' \,. \tag{2.24}$$

$\Delta\bar{\Gamma}_{jk}^{i}$ is the gradients due to the part of the *ith* prism which is between the reference surface and the geoid. Assuming that P is the center of the area with the coordinate, $(0, 0, x_3)$, and the extent of the area in both directions is X, this part becomes a slab. According to (2.22), we have the gradients at P due to this slab

$$\Delta\bar{\Gamma}_{jk} = \sum \Delta\bar{\Gamma}_{jk}^{i} = \sum \left(\Gamma_{jk}^{i} - \bar{\Gamma}_{jk}^{i} \right) = G\rho \int_{0}^{\bar{h}} \int_{-\mathrm{X}/2}^{\mathrm{X}/2} \int_{-\mathrm{X}/2}^{\mathrm{X}/2} \frac{\partial^2}{\partial x_j \partial x_k} \frac{1}{r} dx_1' dx_2' dx_3' \,. \tag{2.25}$$

Using (2.13), (2.17)-(2.21), (2.25) can be derived as:

$$\Delta\bar{\Gamma}_{11} = 4G\rho \left(\tan^{-1} \frac{\left(x_3 - \bar{h} \right)}{\sqrt{\mathrm{X}^2/2 + \left(x_3 - \bar{h} \right)^2}} - \tan^{-1} \frac{x_3}{\sqrt{\mathrm{X}^2/2 + {x_3}^2}} \right),$$

$$\Delta\bar{\Gamma}_{22} = 4G\rho \left(\tan^{-1} \frac{\left(x_3 - \bar{h} \right)}{\sqrt{\mathrm{X}^2/2 + \left(x_3 - \bar{h} \right)^2}} - \tan^{-1} \frac{x_3}{\sqrt{\mathrm{X}^2/2 + {x_3}^2}} \right),$$

$$\Delta\bar{\Gamma}_{33} = 4G\rho\left(\tan^{-1}\frac{\mathrm{X}^2/4}{\left(x_3-\bar{h}\right)\sqrt{\mathrm{X}^2/2+\left(x_3-\bar{h}\right)^2}} - \tan^{-1}\frac{\mathrm{X}^2/4}{x_3\sqrt{\mathrm{X}^2/2+x_3^{\,2}}} \right),$$

$$\Delta\bar{\Gamma}_{12} = \Delta\bar{\Gamma}_{13} = \Delta\bar{\Gamma}_{23} = 0\,. \tag{2.26}$$

If $\mathrm{X} \gg \bar{h}$, the in-line gradients can be approximated as

$$\Delta\bar{\Gamma}_{33} = -2\Delta\bar{\Gamma}_{11} = -2\Delta\bar{\Gamma}_{22} \approx 4G\rho\tan^{-1}\frac{2\sqrt{2}\bar{h}}{\Delta x}\,. \tag{2.27}$$

Supposing $\bar{h}$ is 500 m, when X is 10, 25, 50, and 100 km, $\Delta\bar{\Gamma}_{33}$ is 50.2 E, 20.1 E, 10.1 E, and 5.0 E respectively. The cross gravitational gradients due to a slab at points above the slab are exactly zero since the slab is symmetric with respect to its center (computation point), and the in-line gradients converge to zero with an increase in the width of the slab. As we know, the gravitational acceleration due to an infinite slab with fixed height is constant; and the gravitational gradients are the derivatives of the gravitational acceleration, so they are zero.

Alternatively, $\bar{h}$ can be synthesized by a spherical harmonic model:

$$\bar{h}(P) = \sum_{n,m} H_{nm}Y_{nm}(P)\,, \tag{2.28}$$

where Y_{nm} are surface spherical harmonics, and H_{nm} are spherical harmonic coefficients of the height function $\bar{h}$:

$$H_{nm} = \frac{1}{4\pi}\iint_{\sigma}\bar{h}Y_{nm}d\sigma\,. \tag{2.29}$$

Let the gravitational potential at point P due to the topographic mass bounded by $\bar{h}$ be approximated by

$$V(P) = \frac{GM}{R}\sum_{n=0}\sum_{m=0}^{n}\left(\frac{R}{r}\right)^{n+1}V_{nm}Y_{nm}(P)\,. \tag{2.30}$$

According to (Tsoulis, 1999), the relation between V_{nm} and H_{nm} is approximately

$$V_{nm} = \frac{3}{2l+1}\frac{\rho}{\bar{\rho}}\left\{\frac{H_{nm}}{R} + \frac{l+2}{2}\frac{H2_{nm}}{R^2} + \frac{(l+2)(l+1)}{6}\frac{H3_{nm}}{R^3}\right\}, \tag{2.31}$$

where ρ and $\bar{\rho}$ are the crust density and the mean earth density, respectively, and $H2_{nm}$ and $H3_{nm}$ are spherical harmonic coefficients of the high-order height function:

$$H2_{nm} = \frac{1}{4\pi}\iint_{\sigma}\bar{h}^2Y_{nm}d\sigma\,, \tag{2.32}$$

$$H3_{nm} = \frac{1}{4\pi}\iint_{\sigma}\bar{h}^3Y_{nm}d\sigma\,. \tag{2.33}$$

Thus the gradient due to a spherical harmonic model of the topography can be obtained from the harmonic coefficients derived from global topography data. This is similar to EGM96-derived gradients, which is given in Appendix B. Thus the gradients due to the topographic mass can be modeled by a spherical harmonic elevation model and a corresponding residual terrain model. We first construct a global spherical harmonic

model for the topography and derive the gradients due to this spherical harmonic model. And we model the gradients by the residual topography with respect to the spherical harmonic model. Combining these two parts, we obtain the final gravitational gradients due to the topographic mass.

2.3.2 Direct Numerical Integral

Considering again, formulas (2.1) and (2.3), we can easily get alternative formulas for the six gradients due to the volume bounded by Area A and the topographical surface $x_3^{'} = h(x_1^{'}, x_2^{'})$ under the constant density assumption and in flat earth approximation. Let

$$\Gamma_{jk}(x) = G\rho \iint_A \int_0^{h(x_1^{'}, x_2^{'})} F_{jk} dx_3^{'} dA = G\rho \iint_A T_{jk} dA, \tag{2.34}$$

where F_{jk} and T_{jk} are, respectively, defined as

$$F_{jk} = \frac{\partial^2}{\partial x_j \partial x_k} \frac{1}{r}, \tag{2.35}$$

$$T_{jk} = \int_0^{h(x_1^{'}, x_2^{'})} F_{jk} dx_3^{'}. \tag{2.36}$$

F_{jk} can be expanded analytically as:

$$F_{11} = -\frac{1}{r^3} + \frac{3(x_1 - x_1^{'})^2}{r^5}, F_{12} = \frac{3(x_1 - x_1^{'})(x_2 - x_2^{'})}{r^5}, F_{13} = \frac{3(x_1 - x_1^{'})(x_2 - x_2^{'})}{r^5},$$

$$F_{22} = -\frac{1}{r^3} + \frac{3(x_2 - x_2^{'})^2}{r^5}, F_{23} = \frac{3(x_2 - x_2^{'})(x_3 - x_3^{'})}{r^5},$$

$$F_{33} = -\frac{1}{r^3} + \frac{3(x_3 - x_3^{'})^2}{r^5}. \tag{2.37}$$

T_{jk} is easily derived with a change of variable to α by $\tan\alpha = (x_3 - x_3^{'})/s$, where $s^2 = (x_1 - x_1^{'})^2 + (x_2 - x_2^{'})^2$. Letting $h \equiv h(x_1^{'}, x_2^{'})$, we get

$$T_{11} = \begin{cases} -\dfrac{1}{2(x_3 - x_3^{'})^2}\Big|_{x_3^{'}=0}^{h}, s = 0 \\ \dfrac{1}{s^4}\left(\left(s^2 - 3(x_1 - x_1^{'})^2\right)\dfrac{(x_3 - x_3^{'})}{r} + \dfrac{(x_1 - x_1^{'})^2 (x_3 - x_3^{'})^3}{r^3}\right)\Big|_{x_3^{'}=0}^{h}, s \neq 0 \end{cases},$$

$$T_{12} = \begin{cases} 0, s = 0 \\ \dfrac{(x_1 - x_1^{'})(x_2 - x_2^{'})}{s^4}\left(\dfrac{(x_3 - x_3^{'})^3}{r^3} - \dfrac{3(x_3 - x_3^{'})}{r}\right)\Big|_{x_3^{'}=0}^{h}, s \neq 0 \end{cases},$$

$$T_{13} = \frac{x_1 - x_1^{'}}{r^3}\Big|_{x_3^{'}=0}^{h},$$

$$T_{22}=\begin{cases}-\dfrac{1}{2(x_3-x_3')^2}\Big|_{x_3'=0}^{h}, s=0\\ \dfrac{1}{s^4}\left(\left(s^2-3(x_2-x_2')^2\right)\dfrac{(x_3-x_3')}{r}+\dfrac{(x_2-x_2')^2(x_3-x_3')^3}{r^3}\right)\Big|_{x_3'=0}^{h}, s\neq 0\end{cases},$$

$$T_{23}=\frac{x_2-x_2'}{r^3}\Big|_{x_3'=0}^{h},$$

$$T_{33}=\frac{x_3-x_3'}{r^3}\Big|_{x_3'=0}^{h}, \tag{2.38}$$

(2.38) shows that all six functions, T_{jk}, are not singular at $s=0$ if $x_3 > x'_{3,\max}$. The limiting values of T_{11}, T_{12} and T_{22} at $s=0$ are given in (2.38) for practical computational purposes. Choosing DEM data in Central Colorado (Figure 2.6a) with 30 m grid spacing, examples of T_{jk} are shown in Figure 2.2 for the central point $(x_1=0, x_2=0, x_3=x'_{3,\max}+10m)$ and the topography within the range of ± 4.5 km.

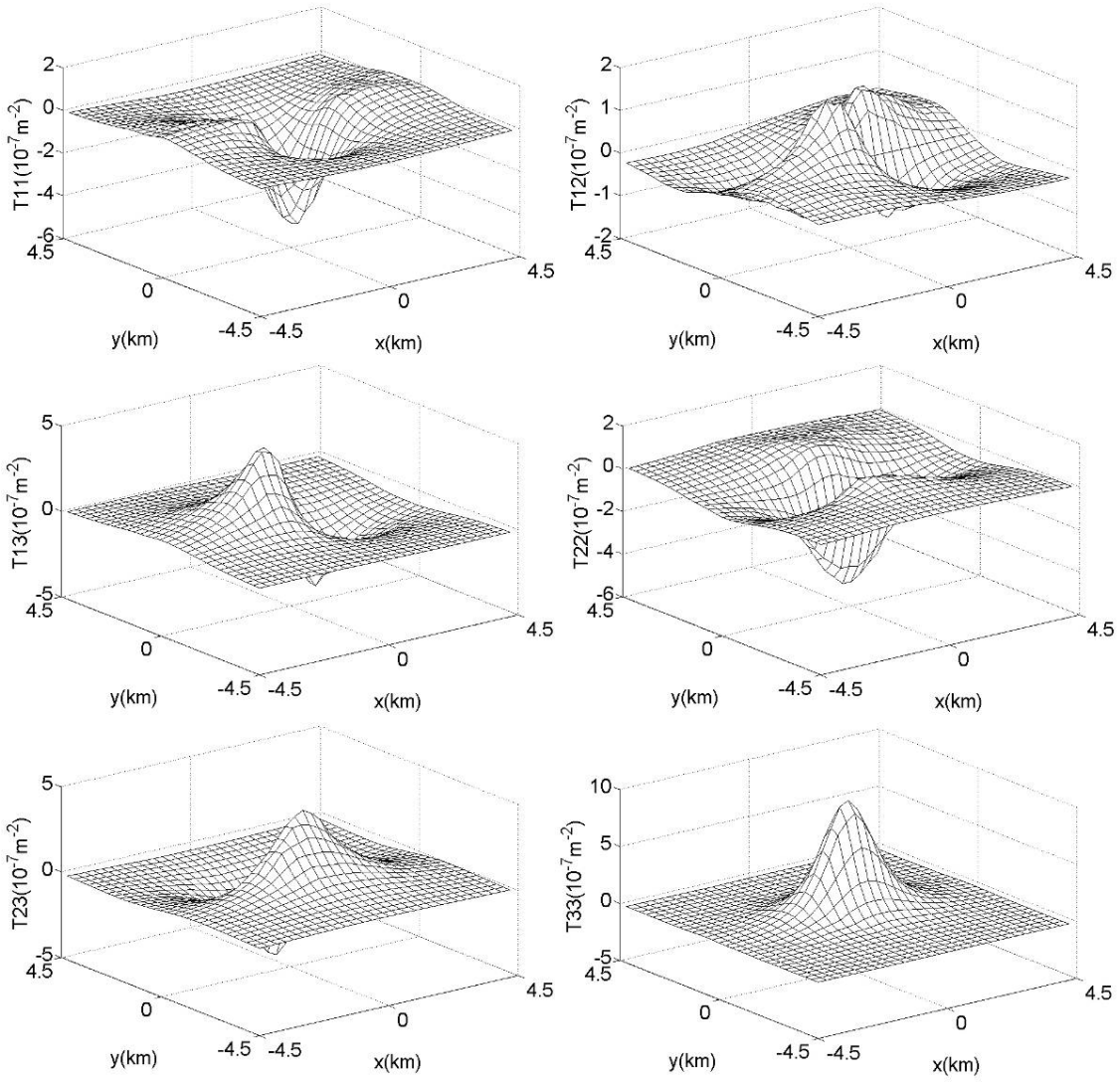

Figure 2.2: Functions, T_{ij}, for a typical topography.

From (2.34), the gravitational gradient can be approximated in a way similar to the right rectangular prism method.

$$\Gamma_{jk} = G\rho \sum_{i=1}^{NM} T_{jk}(x_1 - x'_{1,i}, x_2 - x'_{2,i}, h_i, x_3)\Delta A_i \ , \tag{2.39}$$

where for a regular rectangular grid, $\Delta A_i = \Delta x'_1 \Delta x'_2$, and $h_i = h(x_{1,i}, x_{2,i})$. We also find that (2.39) can be used when the density function is variable in the plane and is constant over the grid intervals in the vertical. Thus one can have

$$\Gamma_{jk} = G\sum_{i=1}^{NM} T_{jk}(x_1 - x_{1,i}^{'}, x_2 - x_{2,i}^{'}, h_i, x_3)\rho(x_{1,i}^{'}, x_{2,i}^{'})\Delta A_i \,. \tag{2.40}$$

One can also construct a model of the topographic surface using spline functions. Splines are piecewise continuous polynomials of order, n=0, 1, 2 … The elevation can be constructed by splines in terms of the horizontal coordinates: $h(x_1, x_2) = h_i + b(x_1 - x_{1,i}) + c(x_2 - x_{2,i}) + \cdots$, where b and c are the coefficients of splines. In any case it might be possible that we analytically integrate the integrand, T_{jk}, over the grid interval in (2.34), instead of using approximation like (2.39). Prisms are a special case of splines. When n=0, they are a set of step functions which represents a flat top approximation for the topography. Both the right rectangular prisms and the direct numerical integration (2.39) are based on this approximation, but they are different in the way of computing gradient where the former is computed over the grid interval and the latter is evaluated on the grid point.

For the rectangular grid spacing of SRTM data, one can decompose a rectangle into two triangles and each triangle has three vertices. Let $(i1, i2, i3)$ denote three vertices of the ith triangle and denote $(x_{1,i1}^{'}, x_{2,i1}^{'}, h_{i1})$, $(x_{1,i2}^{'}, x_{2,i2}^{'}, h_{i2})$ and $(x_{1,i3}^{'}, x_{2,i3}^{'}, h_{i3})$ as the coordinates of the vertices. Letting $T_{jk,i} = T_{jk}(x_1 - x_{1,i}^{'}, x_2 - x_{2,i}^{'}, h_i, x_3)$, we compute $T_{jk,i1}$, $T_{jk,i2}$, and $T_{jk,i3}$ and use their average, $\frac{T_{jk,i1} + T_{jk,i2} + T_{jk,i3}}{3}$, to replace $T_{jk}(x_1 - x_{1,i}^{'}, x_2 - x_{2,i}^{'}, h_i, x_3)$ in (2.39). Thus a numerical integration of (2.39) with respect to one triangle is analogous to the trapezoidal rule and is given by

$$\Gamma_{jk} = \frac{G\rho}{3}\sum_{i=1}^{2NM}\left(T_{jk,i1} + T_{jk,i2} + T_{jk,i3}\right)\Delta B_i \,, \tag{2.41}$$

where ΔB_i is the area of the ith triangle with corners represented by $(i1, i2, i3)$. For triangles dividing rectangles, we obviously have $\Delta B_i = \Delta A_i / 2$.

2.3.3 Polyhedron Method

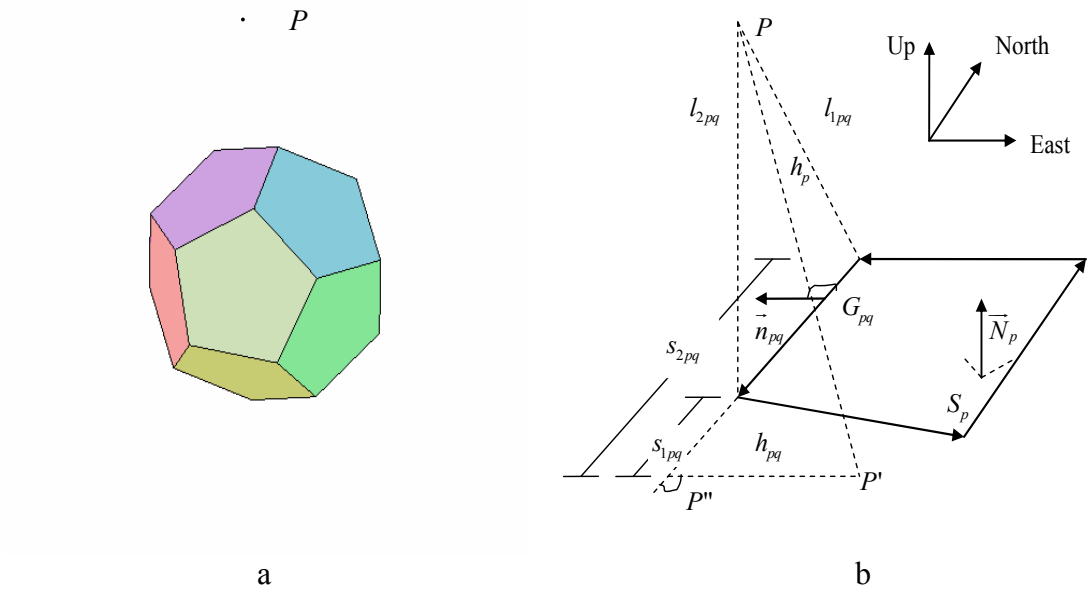

a b

Figure 2.3: Polyhedron (a) and geometrical definitions of the quantities (b) in the polyhedral method.

To determine the potential and its derivatives due to irregular inhomogeneous bodies, they can be decomposed into polyhedral parts with homogeneous density. The potential and its derivatives due to these polyhedral parts can be efficiently determined using a transformation of volume integral into line integrals. Petrovic (1996) gave analytical formulas to compute the potential and its first and second derivatives due to such bodies. Figure 2.3a presents a polyhedral body. Assuming that it has n faces, each having m sides. according to formula (32) (Petrovic, 1996), the gravitational gradient at P due to this polyhedral body is given by

$$\Gamma_{jk} = G\rho \sum_{p=1}^{n} \cos\left(\vec{N}_p, \vec{e}_j\right) \left[\sum_{q=1}^{m} \cos\left(\vec{n}_{pq}, \vec{e}_k\right) LN_{pq} + \sigma_p \cos\left(\vec{N}_p, \vec{e}_k\right) \sum_{q=1}^{m} \sigma_{pq} AN_{pq} + SING_{\beta_{pk}} \right], \tag{2.42}$$

where $LN_{pq} = \ln \dfrac{s_{2pq} + l_{2pq}}{s_{1pq} + l_{1pq}}$, (2.43)

$$AN_{pq} = \arctan\frac{h_p s_{2pq}}{h_{pq} l_{2pq}} - \arctan\frac{h_p s_{1pq}}{h_{pq} l_{1pq}}, \tag{2.44}$$

and $\beta_{pk} = \sum_{q=1}^{m} \cos\left(\vec{n}_{pq}, \vec{e}_k\right) LN_{pq} + \sigma_p \cos\left(\vec{N}_p, \vec{e}_k\right) \sum_{q=1}^{m} \sigma_{pq} AN_{pq}$. (2.45)

For the notation refer to Figure 2.3b. Here S_p is the plane containing the *pth* face, and P is the computation point. P' is the perpendicular projection of P onto the plane of S_p. e_j and e_k are unit vectors representing coordinate axes (East, North, and Up coordinate system). $\vec{N}_p$ is the outward pointing unit normal of the face of S_p. σ_p is -1 when $\vec{N}_p$ points to the half space containing the point P and +1 when it points to the other half space. $\vec{n}_{pq}$ is the outward unit normal of the segment G_{pq} and σ_{pq} is -1 when $\vec{n}_{pq}$ points to the half plane containing P' and +1 when it points to the other half plane. P'' is the orthogonal projection of P' onto the straight line defined by the segment G_{pq}. s_{1pq} and s_{2pq} are the distances between P'' and the two end points of G_{pq}. l_{1pq} and l_{2pq} are the distances between P and the two end points of segment G_{pq}. $SING_{\beta pk}$ is the singularity term defined for different situations of P' lying at the corner, on a line segment, or in the interior of the face S_p. Tsoulis and Petrovic (2001) elaborated on the singularity term appearing in the numerical evaluations. When P' lies at a corner, the singularity term is $-\vartheta\cos(N_P, e_k)\sigma_P$, where ϑ is the angle between the two segments meeting at P'; when P' is on a line segment, the singularity term is $-\pi\cos(N_P, e_k)\sigma_P$; π is the half circle angle; when P' is inside of face S_p, the singularity term is $-2\pi\cos(N_P, e_k)\sigma_P$.

Suppose we have a set of DEM data in the area A. The DEM data are composed by a series of regularly spaced discrete points, D_i, $i = 1, \ldots, NM$. N and M are the grid numbers in the east and the north direction. Let $\left(x_{1,i}, x_{2,i}, h_i\right)$ be the coordinate of D_i. Each four surrounding points, D_i, D_{i+1}, D_{i+N} and D_{i+N+1}, construct a rectangle like Figure 2.4b. If the southwest-northeast triangulation is used, we connect D_i and D_{i+N+1}. Thus we have two triangles composed by two sets of vertices, $\left(D_i, D_{i+N}, D_{i+N+1}\right)$ and $\left(D_i, D_{i+1}, D_{i+N+1}\right)$. Using either southwest-northeast or northwest-southeast cross diagonals, each rectangle of the grid (Figure 2.4b) can be separated into 2 triangle faces. Thus we have $2NM$ triangle faces to represent the topographic surface. Thus assuming constant density throughout, the terrain mass is a polyhedron with $2NM$ triangle faces (each with 3 sides), the bottom horizontal reference face and four perpendicular faces (each with $3+N$, or $3+M$ edges,) defining Area A (Figure 2.4 a). Thus we apply Petrovic's method to compute the gradients due to this one polyhedral body.

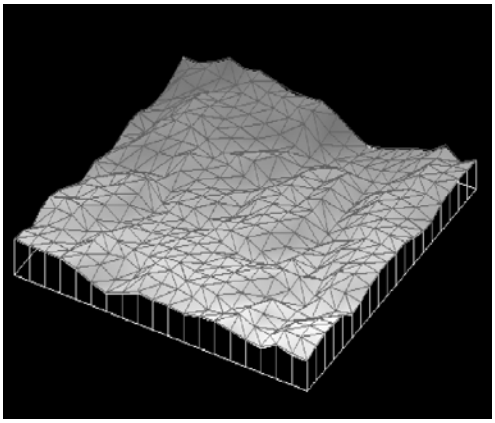

a: Triangulated topographic surface

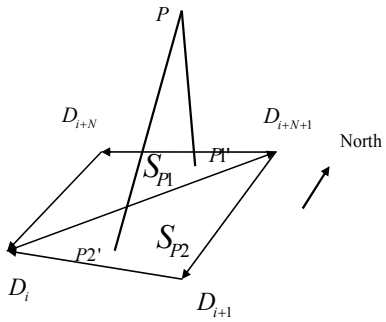

b: Southwest-northeast triangle

Figure 2.4: Adopted geometrical definitions.

This kind of surface triangulation is a first order approximation for the topographic surface instead of the step function approximation used in the right rectangular prism method. Choosing different diagonals for the rectangular grid can lead to different results for the computed gradient. Delaunay triangulation is a way to choose the optimal triangulation (Quak and Schumaker, 1990). The criterion in this case is that the minimal angle in a triangulation is bigger than that in other triangulations. This triangulation is thus determined by this property and long thin triangles are avoided with this criterion.

2.3.4 The extent of DEM and the reference surface

Besides the method of triangulation for the topographical surface, we need to consider the extent of Area A and the horizontal reference surface in practical modeling. We choose the set of SRTM data in central Colorado shown in Figure 2.5 to study the extent for a particular required accuracy. The left part of Figure 2.5 is the topography with 30 meter resolution. The maximum, mean and minimum elevations are 4409.4 m, 3008.1 m and 1900.2 m, respectively. First, a constant mean elevation surface was used as reference surface. Thus a residual terrain model was obtained by subtracting the reference value, 3008.1 m, from the original elevation data. We use direct numerical integral to compute gradients due to each block in (2.23). It is done by changing the lower limit in (2.38) from 0 to $\bar{h}$. $\bar{h}$ can be the mean elevation or the minimum elevation. Final gradients are obtained by summing gradients due to each block (if $h < \bar{h}$, the gradients due to that block is negative). The computation is carried out at 300 points around the area center (on the black line in Figure 2.5). Their coordinates are ($\varphi_i = 39^\circ.5$, $\lambda_i = 253^\circ.5 + (i-150)/3600$, $h_i = 4419.4m$), $i = 1,\ldots,300$. We compute the gradients due to the topographic mass enclosed by a square rectangle area centered on the computation point. The extent of area is defined as the width of the square rectangle. We assume the gradients due to the topography with 50 arcmin extent are the "true" values,

and compare them with the gradients derived from smaller extents. Let $\Delta\Gamma_{jk}$ be the difference between "true" gradient and gradients derived from smaller extents. The rms values of the differences are shown in Table 2.1. The extent of 30 arcmin for all gradient components is necessary to achieve an accuracy of 1 E when compared to the extent of 50 arcmin. For each component, $\Delta\Gamma_{11}$, $\Delta\Gamma_{12}$,…, $\Delta\Gamma_{33}$, the extents are respectively 24, 30, 10, 24, 18 and 30 arcmin, where the rms error is less than 1 E. The minimum elevation is also used to compare gradients due to different extents. We still use direct numerical integration model to compute the gradients in this case. The result is shown in Table 2.2. The rms values of the differences of in-line gradients are larger than those in Table 2.1, but the rms values of the differences of cross gradients are equal to those in Table 2.1. For each component, $\Delta\Gamma_{11}$, $\Delta\Gamma_{12}$,…, $\Delta\Gamma_{33}$, the extents are, respectively, 48, 30, 10, 46, 18, 48 arcmin where the rms is less than or around 1 E. This result shows that choosing different reference surfaces only has greatest impact on the in-line gradients, but not on off-line gradients.

Instead of using a constant reference surface, we use 360 degree spherical harmonic elevation surface as a reference surface. This elevation surface is synthesized by a spherical harmonic global elevation model (Tsoulis, 1999). Global $0^{\circ}.5 \times 0^{\circ}.5$ mean elevation data are obtained from ETOPO2, 2 arcmin global topography data. This spherical harmonic elevation surface is shown on the right of Figure 2.5. The maximum, mean and minimum elevations are 3087.2 m, 2769.8 m and 2434.8 m. We compute the gradients due to the topographic masses enclosed by 360 degree spherical harmonic surface and the geoid at 3600 grid points (computation altitude: 4419.4 m) with the resolution of 1 arc min in this area. The statistics of these gradients are given in Table 2.3. Let $\Gamma_{jk}\big|_{ETM}$ be the gradients due to the global topography model. The variation of $\Gamma_{33}\big|_{ETM}$ is between 1.4 E and 7.9 E and its mean is 5.3 E. The standard deviation for all gradient components is less than 1.3 E. The spherical harmonic surface is lower than the constant mean surface in most of the area from Figure 2.5, and it means that more topographic masses are considered for the residual gradient computation. The rms values of the differences of gradients due to different extents are larger than the first case where the constant mean surface (3008.1 m) is used. Table 2.4 shows that the rms of $\Delta\Gamma_{33}$ is as high as 3.85 E when the extent of 32 arc min is used. For each component, $\Delta\Gamma_{11}$, $\Delta\Gamma_{12}$,…, $\Delta\Gamma_{33}$, the extents are respectively 40, 32, 12, 38, 16 and 44 arc min when the rms is less than 1 E.

In summary, for relatively rough terrain of about 2000 m in elevation variations, an area extent of a half degree is needed to achieve the accuracy of 1 E when the computation altitude is at 10 m above the maximum elevation, provided that we use the mean topographical surface as the reference surface.

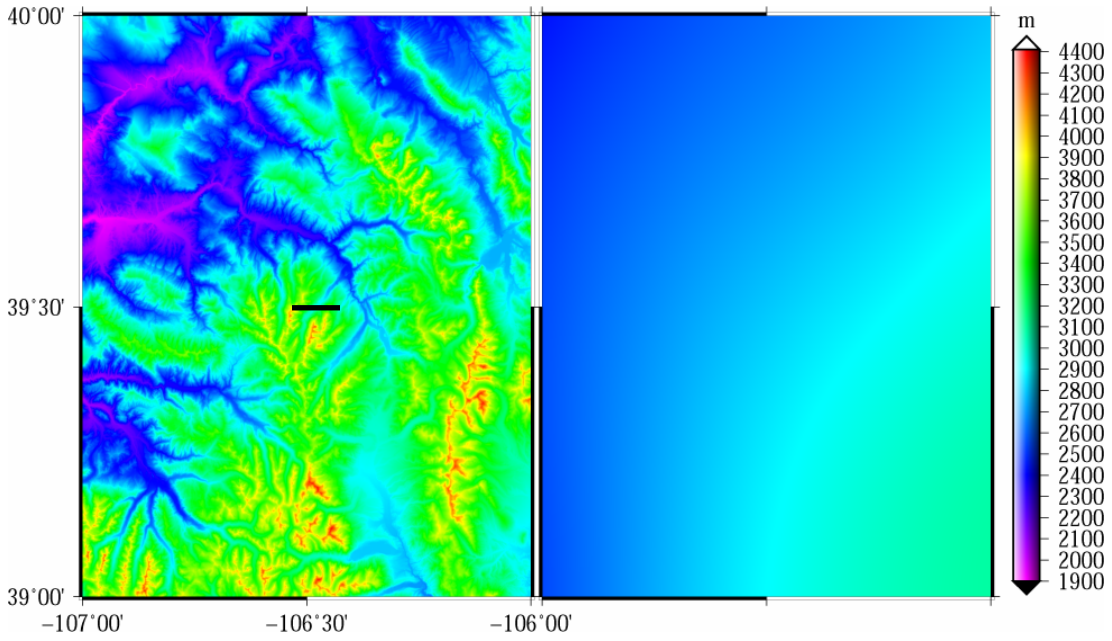

Figure 2.5: Digital terrain model (left: 1"×1"; right: 360 degree spherical harmonic model).

Table 2.1: The RMS of the differences of gradients derived from different extents of residual DEM with respect to the constant reference surface (3008.1m) (unit: E).

Extent(arc min)	ΔΓ11	ΔΓ12	ΔΓ13	ΔΓ22	ΔΓ23	ΔΓ33
10	8.47	5.28	0.83	1.77	3.66	6.97
12	6.00	4.27	0.39	1.64	2.57	4.78
14	4.06	3.54	0.76	0.70	1.79	3.67
16	2.59	3.16	0.93	0.36	1.19	2.9
18	1.74	2.88	0.93	0.94	0.81	2.56
20	1.25	2.63	0.86	1.18	0.62	2.28
22	1.01	2.34	0.78	1.07	0.51	1.96
24	0.89	2.06	0.68	0.79	0.43	1.63
26	0.71	1.72	0.59	0.66	0.38	1.36
28	0.58	1.34	0.50	0.55	0.33	1.11
30	0.51	0.95	0.41	0.44	0.28	0.89
32	0.43	0.57	0.33	0.33	0.24	0.68

Table 2.2: The RMS of the differences of gradients derived from different extents of residual DEM with respect to the constant reference surface (1900.2 m) (unit: E).

Extent(arc min)	ΔΓ11	ΔΓ12	ΔΓ13	ΔΓ22	ΔΓ23	ΔΓ33
12	53.37	4.28	0.43	30.5	2.58	83.84
14	42.90	3.55	0.79	25.76	1.79	68.63
16	35.04	3.17	0.95	22.28	1.19	57.3
18	29.14	2.89	0.94	19.43	0.81	48.56
20	24.57	2.64	0.87	16.85	0.62	41.41
22	20.94	2.34	0.78	14.41	0.51	35.35
24	18.00	2.06	0.69	12.17	0.43	30.17
26	15.42	1.72	0.59	10.37	0.38	25.79
28	13.17	1.34	0.50	8.80	0.33	21.98
30	11.20	0.95	0.41	7.44	0.28	18.63
32	9.45	0.57	0.33	6.23	0.24	15.68
34	7.87	0.25	0.27	5.18	0.20	13.05
36	6.45	0.08	0.21	4.25	0.17	10.70
38	5.20	0.08	0.17	3.37	0.14	8.58
40	4.09	0.10	0.13	2.60	0.11	6.69
42	3.08	0.10	0.10	1.93	0.09	5.01
44	2.17	0.07	0.07	1.34	0.07	3.51
46	1.36	0.05	0.04	0.84	0.04	2.19
48	0.64	0.03	0.02	0.39	0.02	1.03

Table 2.3: The statistics of the gradients due to the topographic masses enclosed by the 360 degree spherical harmonic surface (unit: E).

Gradients	Γ11	Γ12	Γ13	Γ22	Γ23	Γ33
Mean	-1.4	2.3	0.8	-3.9	-4.5	5.3
Std	0.8	0.5	0.7	0.8	0.9	1.3
Min	-2.5	1.1	-1.0	-5.5	-6.9	1.4
Max	0.8	3.2	1.9	-1.8	-3.0	7.9

Table 2.4: The RMS of the differences of gradients derived from different extents of residual DEM with respect to the 360 degree spherical harmonic surface (unit: E).

Extent(arc min)	ΔΓ11	ΔΓ12	ΔΓ13	ΔΓ22	ΔΓ23	ΔΓ33
10	20.33	5.80	1.75	6.56	3.01	26.87
12	15.17	4.80	0.66	5.05	2.06	20.16
14	11.36	4.06	0.11	4.86	1.37	16.13
16	8.64	3.67	0.32	4.88	0.84	13.47
18	6.86	3.37	0.42	4.81	0.53	11.64
20	5.65	3.09	0.43	4.49	0.38	10.12
22	4.82	2.76	0.41	3.90	0.31	8.71
24	4.23	2.44	0.36	3.22	0.26	7.44
26	3.66	2.07	0.32	2.74	0.24	6.40
28	3.15	1.66	0.26	2.32	0.21	5.46
30	2.69	1.23	0.21	1.94	0.18	4.62
32	2.27	0.83	0.16	1.59	0.15	3.85
34	1.86	0.48	0.12	1.31	0.13	3.16
36	1.49	0.25	0.09	1.05	0.11	2.53
38	1.17	0.12	0.07	0.78	0.09	1.95
40	0.90	0.08	0.06	0.54	0.08	1.44
42	0.65	0.07	0.04	0.36	0.06	1.01
44	0.44	0.06	0.03	0.22	0.05	0.65

2.4 Fourier Transform

The previous section described three finite elements methods. If many gradient values are needed and a large height data set is used, these methods can be very time consuming. Fourier transform techniques can be applied to reduce the computation time significantly if a raster grid of DEM data is used and the computation points are on a grid with the same spacing and projected to a constant height above the terrain. Parker's and Forsberg's methods are two Fourier transform algorithms to compute the gravitational gradient due to the topographic mass.

2.4.1 Parker's method

Parker (1972) worked with the spectral relationship between potential and vertical gravitation; however, one can extend his method for the gravitational gradients.

Under the planar approximation, we can get the gravitational potential due to the volume mass bounded by the Area A (geoid approximated as a plane) and the topographical surface is given by (2.1), written more explicitly as

$$V(x_1, x_2, x_3) = G\rho \iint_A \int_0^h \frac{1}{r} dx_3' dA \,, \tag{2.46}$$

where $h = h(x_1', x_2')$, and $r = \sqrt{(x_1 - x_1')^2 + (x_2 - x_2')^2 + (x_3 - x_3')^2}$. Assuming $g(x_1, x_2)$ is a finite energy function in two dimensions:

$$\int_{-\infty}^{\infty}\int_{-\infty}^{\infty}\left(g\left(x_1, x_2\right)\right)^2 dx_1 dx_2 < \infty, \tag{2.47}$$

we have the following 2D continuous Fourier transform pair:

$$G\left(f_1, f_2\right) = \Im\left(g\left(x_1, x_2\right)\right) = \int_{-\infty}^{\infty}\int_{\infty}^{\infty} g\left(x_1, x_2\right)\cdot e^{-i2\pi(f_1 x_1 + f_2 x_2)} dx_1 dx_2 , \tag{2.48}$$

$$g\left(x_1, x_2\right) = \Im^{-1}\left(G\left(f_1, f_2\right)\right) = \int_{-\infty}^{\infty}\int_{\infty}^{\infty} G\left(f_1, f_2\right)\cdot e^{i2\pi(f_1 x_1 + f_2 x_2)} df_1 df_2 , \tag{2.49}$$

where (f_1, f_2) are the frequencies corresponding to the spatial coordinates, (x_1, x_2) . Applying (2.48) to the potential in (2.46), we have

$$\Im(V) = G\rho\iint_A\int_0^h \Im\left(\frac{1}{r}\right) dx_3' dA . \tag{2.50}$$

This integral can be analytically computed by using polar coordinates and a little algebra (Bracewell, 1965; Parker, 1972), and we obtain

$$\Im(V) = G\rho\iint_A\int_0^{h(x_1', x_2')} \frac{1}{f} e^{-2\pi(x_3 - x_3')f} dx_3' e^{-2\pi i(f_1 x_1' + f_2 x_2')} dA , \ f \neq 0 , \tag{2.51}$$

where $f = \sqrt{f_1^2 + f_2^2}$. Integrating (2.51) with respecting to x_3' , we have

$$\Im(V) = \frac{G\rho}{2\pi f^2} e^{-2\pi x_3 f}\iint_A (e^{2\pi h(x_1', x_2')f} - 1) e^{-2\pi i(f_1 x_1' + f_2 x_2')} dA , \ f \neq 0 . \tag{2.52}$$

From $e^{2\pi f h(x_1', x_2')} = 1 + 2\pi f h(x_1', x_2') + \frac{1}{2!}(2\pi f h(x_1', x_2'))^2 + \cdots$, (2.52) can be expanded as follows:

$$\begin{aligned}\Im(V) &\approx 2\pi G\rho e^{-2\pi x_3 f}\sum_{n=1}^{\infty}\frac{1}{n!}(2\pi f)^{n-2}\iint_A h(x_1', x_2') e^{-i2\pi(f_1 x_1' + f_2 x_2')} dA \\ &= 2\pi G\rho e^{-2\pi x_3 f}\sum_{n=1}^{\infty}\frac{1}{n!}(2\pi f)^{n-2}\Im\left(\left(h(x_1', x_2')\right)^n\right)\end{aligned} \quad , f \neq 0 , \tag{2.53}$$

provided that $A = (-\infty, \infty)\times(-\infty, \infty)$. However, A is the finite area that we choose to compute the gravitational gradient due to the topographic mass, so (2.53) is an approximation. Furthermore, we assume the Fourier transforms of the powers of *h* exist. In practice, *h* is given at grid points, so discrete approximations of the continuous Fourier transform and a finite Taylor series are used in the numerical evaluation of (2.53). In (2.53), we find that $\Im(V)$ is singular at the frequency origin, which is a property of the potential in planar approximation (the Newtonian potential of an infinite flat slab does not exist).

Now we use the relationships in the frequency domain between the potential and its second-order derivatives (Jekeli, 2003):

$$\Im\left(\Gamma_{jk}\right) = \mu_{jk}\Im(V) , \tag{2.54}$$

where

$$\mu_{11} = -(2\pi)^2 f_1^2 , \quad \mu_{12} = -(2\pi)^2 f_1 f_2 , \quad \mu_{13} = -i(2\pi)^2 f_1 f ,$$

$$\mu_{22} = -(2\pi)^2 f_2^2 \ , \qquad \mu_{23} = -i(2\pi)^2 f_2 f \ ,$$
$$\mu_{33} = (2\pi)^2 f^2 \ . \tag{2.55}$$

From (2.54) and (2.55), we find that the Fourier transform of the gravitational gradient is not singular at the origin since

$$\lim_{f_1 \to 0, f_2 \to 0} \Im\left(\Gamma_{jk}\right) = 0 \text{, for all } j,k \ . \tag{2.56}$$

Finally we get the gravitational gradient by applying the inverse Fourier transform to the spectra of the gradients given in (2.54).

$$\Gamma_{jk} = 2\pi G\rho \Im^{-1}\left(\mu_{jk} e^{-2\pi x_3 f} \sum_{n=1}^{\infty} \frac{1}{n!} (2\pi f)^{n-2} \Im\left(h^n\right) \right). \tag{2.57}$$

The density is assumed as constant for simplicity, but can be allowed to vary horizontally. In that case, the inner Fourier transform would be applied to ρh^n. Tziavos et al. (1996) studied the effect of surface density variation on terrain correction using terrain and density data with resolution of $11".25 \times 18".75$ in Australia.

2.4.2 Forsberg's method

Forsberg (1985) introduced a different Fourier transform method that is based on the series expansions of the nonlinear integrals, T_{jk} in (2.36). This method makes use of the convolution theorem in spectral analysis instead of the direct derivation of an analytical form as in Parker's method.

Considering the same mass volume as before, we start from (2.34) and form a Taylor expansion of $F_{jk}(x_3')$ with respect to $x_3' = 0$,

$$F_{jk}(x_3') = F_{jk}(0) + F_{jk}'(0) \cdot x_3' + \frac{F_{jk}''(0)}{2} \cdot \left(x_3'\right)^2 + \frac{F_{jk}'''(0)}{6} \cdot \left(x_3'\right)^3 + \cdots + \frac{F_{jk}^{(n)}(0)}{n!} \cdot \left(x_3'\right)^n . \tag{2.58}$$

$F_{jk}^{(n)}(0)$ can be easily derived, for example,

$$F_{33}(0) = \frac{1}{r_0^3} - \frac{3x_3^2}{r_0^5} \ ,$$

$$F_{33}'(0) = \frac{9x_3}{r_0^5} - \frac{15x_3^3}{r_0^7} \ ,$$

$$F_{33}''(0) = \frac{-9}{r_0^5} + \frac{90x_3^2}{r_0^7} - \frac{105x_3^4}{r_0^9} \ ,$$

$$F_{33}'''(0) = \frac{-225x_3}{r_0^7} + \frac{1050x_3^3}{r_0^9} - \frac{945x_3^5}{r_0^{11}} \ ,$$

$$F_{33}^{(4)}(0) = \frac{225}{r_0^7} - \frac{4725x_3^2}{r_0^9} + \frac{14175x_3^4}{r_0^{11}} - \frac{10395x_3^6}{r_0^{13}} \ , \tag{2.59}$$

where $r_0 = \sqrt{\left(x_1 - x_1'\right)^2 + \left(x_2 - x_2'\right)^2 + x_3^2}$. Substituting (2.58) into (2.34), and then integrating with respect to x_3' from 0 to h, we get

$$\Gamma_{jk} = G\rho \iint_A \left(F_{jk}(0)\cdot h + \frac{F_{jk}^{'}(0)}{2}\cdot h^2 + \frac{F_{jk}^{''}(0)}{6}\cdot h^3 + \cdots + \frac{F_{jk}^{n}(0)}{(n+1)!}\cdot h^{n+1} \right) dA$$
$$= G\rho \sum_{n=1}^{\infty} \iint_A \frac{F_{jk}^{(n-1)}(0)}{n!}\cdot h^n dA \qquad (2.60)$$

Again, assuming $A = (-\infty,\infty)\times(-\infty,\infty)$, and letting $g_{jk}^{(n-1)} = \frac{F_{jk}^{(n-1)}}{n!}$, we have

$$\iint_A \frac{F_{jk}^{(n-1)}(0)}{n!}\cdot h^n dA = \int_{-\infty}^{\infty}\int_{-\infty}^{\infty} g_{jk}^{(n-1)}\left(x_1 - x_1^{'}, x_2 - x_2^{'}, x_3\right) h^n\left(x_1^{'}, x_2^{'}\right) dx_1^{'} dx_2^{'}. \qquad (2.61)$$

Provided x_3 = constant for all $\left(x_1^{'}, x_2^{'}\right)$, the integral in (2.61) becomes a convolution, and we have:

$$\Gamma_{jk}(x) = G\rho \sum_{n=1}^{\infty} g_{jk}^{(n-1)} * h^n = G\rho \sum_{n=1}^{\infty} \Im^{-1}\left(\Im\left(g_{jk}^{(n-1)}\right)\Im\left(h^n\right)\right), \qquad (2.62)$$

where "*" denotes convolution as defined in (2.61). The density is assumed constant, but can be combined with the power of h if a surface density file is used. Thus we get alternative formula of (2.62):

$$\Gamma_{jk}(x) = G \sum_{n=1}^{\infty} g_{jk}^{(n-1)} * (\rho h^n) = G \sum_{n=1}^{\infty} \Im^{-1}\left(\Im\left(g_{jk}^{(n-1)}\right)\Im\left(\rho h^n\right)\right). \qquad (2.63)$$

2.4.3 Discrete Fourier transform

In the previous section, Parker's and Forsberg's Fourier transform are introduced to compute the gravitational gradient from the topographic function, h. Discrete Fourier transforms (Schwarz, et al., 1990) are used in the numerical evaluation of these two methods if a grid of DEM data is available. The discrete Fourier transform, or Fast Fourier transform, operates on discrete and periodic functions. Let $g_{m1,m2}$ and $h_{m1,m2}$ be such functions. The FFT and its inverse are defined as follows

$$FFT(g_{m_1,m_2}) = G_{p_1,p_2} = \Delta x_1^{'}\Delta x_2^{'} \sum_{m_1=0}^{M_1-1}\sum_{m_2=0}^{M_2-1} g_{m_1,m_2} e^{-i2\pi\left(\frac{p_1 m_1}{M_1} + \frac{p_2 m_2}{M_2}\right)},$$
$$p_1 = 0,\ldots,M_1-1,\ p_2 = 0,\ldots,M_2-1, \qquad (2.64)$$
$$FFT^{-1}(G_{p_1,p_2}) = g_{m_1,m_2} = \frac{1}{M_1\Delta x_1^{'} M_2 \Delta x_2^{'}} \sum_{p_1=0}^{M_1-1}\sum_{p_2=0}^{M_2-1} G_{p_1,p_2} e^{i2\pi\left(\frac{p_1 m_1}{M_1} + \frac{p_2 m_2}{M_2}\right)},$$
$$m_1 = 0,\ldots,M_1-1,\ m_2 = 0,\ldots,M_2-1, \qquad (2.65)$$

where M_1 and M_2 are the total sample numbers in both dimensions, Δx_1 and Δx_2 are the sample intervals in both dimensions, and $A = \left[0,\left(M_1-1\right)\Delta x_1\right]\times\left[0,\left(M_2-1\right)\Delta x_2\right]$. The convolution of g_{m_1,m_2} and h_{m_1,m_2} is defined as

$$c_{n_1,n_2} = \sum_{m_1=0}^{M_1-1}\sum_{m_2=0}^{M_2-1} g_{m_1-n_1,m_2-n_2} h_{m_1,m_2} \Delta x_1^{'}\Delta x_2^{'},$$

$$n_1 = 0,\ldots,M_1-1,\ n_2 = 0,\ldots,M_2-1, \tag{2.66}$$

(2.66) can be evaluated using the Fast Fourier transform by applying the convolution theorem.

$$c_{n_1,n_2} = FFT^{-1}(FFT(g)_{p_1,p_2}\ FFT(h)_{p_1,p_2}). \tag{2.67}$$

The numerical implementations of Parker's and Forsberg's methods are

$$\Gamma_{jk}(n_1,n_2) = 2\pi G\rho FFT^{-1}\left(\mu_{jk_{p_1,p_2}} e^{-2\pi x_3 f_{p_1,p_2}} \sum_{n=1}^{\infty} \frac{1}{n!}\left(2\pi f_{p_1,p_2}\right)^{n-2} FFT\left(h^n\right)_{p_1,p_2}\right),$$

$$p_1 = 0,\ldots,M_1-1,\ p_2 = 0,\ldots,M_2-1, \tag{2.68}$$

$$\Gamma_{jk}(n_1,n_2) = G\rho FFT^{-1}\left(\sum_{n=1}^{\infty} FFT\left(g_{jk}^{(n-1)}\right)_{p_1,p_2}\ FFT\left(h^n\right)_{p_1,p_2}\right),$$

$$p_1 = 0,\ldots,M_1-1,\ p_2 = 0,\ldots,M_2-1, \tag{2.69}$$

In (2.68), it is important to define

$$\chi_{p_1,p_2}^{(n)} = \mu_{jk_{p_1,p_2}} e^{-2\pi x_3 f_{p_1,p_2}} \frac{1}{n!}\left(2\pi f_{p_1,p_2}\right)^{n-2}, \tag{2.70}$$

where the frequency is defined as

$$f_{p_1,p_2} = \sqrt{f_{1_{p1}}^2 + f_{2_{p1}}^2},$$

$$f_{1_{p1}} = \frac{p_1}{\Delta x_1' M_1},\ f_{2_{p1}} = \frac{p_2}{\Delta x_2' M_2}, \text{ for } p_1 = 0,\ldots,\frac{M_1}{2}-1,\ p_2 = 0,\ldots,\frac{M_2}{2}-1, \tag{2.71}$$

$$f_{1_{p1}} = \frac{p_1 - M_1}{\Delta x_1' M_1},\ f_{2_{p1}} = \frac{p_2 - M_2}{\Delta x_2' M_2}, \text{ for } p_1 = \frac{M_1}{2},\ldots,M_1-1, p_2 = \frac{M_2}{2},\ldots,M_2-1,$$

such that it is like the result of the FFT applied to a discrete, periodic function. Only this will ensure that the computed gradients are real numbers. The periodicity is ensured by

$$\chi_{M_1+p_1,p_2}^{(n)} = \chi_{p_1,p_2}^{(n)},\ p_1 = 0,\ldots,M_1-1 \text{ all } p_2; \tag{2.72}$$

$$\chi_{p_1,M_2+p_2}^{(n)} = \chi_{p_1,p_2}^{(n)},\ p_2 = 0,\ldots,M_2-1 \text{ all } p_1. \tag{2.73}$$

Furthermore, the spectral component, $\chi_{p_1,p_2}^{(n)}$ must satisfy conjugate symmetry (to obtain real-number gradients):

$$\chi_{M_1-p_1,M_2-p_2}^{(n)} = \left(\chi_{p_1,p_2}^{(n)}\right)^*,\ p_1 = 0,\ldots,M_1-1;\ p_2 = 0,\ldots,M_2-1. \tag{2.74}$$

Thus four spectral component values must be real:

$$\chi_{0,0}^{(n)} = \left(\chi_{0,0}^{(n)}\right)^*, \qquad \chi_{0,\frac{M_2}{2}}^{(n)} = \left(\chi_{0,\frac{M_2}{2}}^{(n)}\right)^*,$$

$$\chi_{\frac{M_1}{2},0}^{(n)} = \left(\chi_{\frac{M_1}{2},0}^{(n)}\right)^*,\ \chi_{\frac{M_1}{2},\frac{M_2}{2}}^{(n)} = \left(\chi_{\frac{M_1}{2},\frac{M_2}{2}}^{(n)}\right)^*, \tag{2.75}$$

In addition, there is conjugate symmetry in p_1 for $p_2 = 0$ and $p_2 = M_2/2$:

$$\chi_{M_1-p_1,0}^{(n)} = \left(\chi_{p_1,0}^{(n)}\right)^*,\quad \chi_{M_1-p_1,M_2/2}^{(n)} = \left(\chi_{p_1,M_2/2}^{(n)}\right)^*; \tag{2.76}$$

and in p_2 for $p_1 = 0$ and $p_1 = M_1/2$

$$\chi^{(n)}_{0,M_2-p_2} = \left(\chi^{(n)}_{0,p_2}\right)^*, \quad \chi^{(n)}_{M_1/2,M_2-p_2} = \left(\chi^{(n)}_{M_1/2,p_2}\right)^*. \tag{2.77}$$

In fact, the quantity $\chi^{(n)}_{p_1,p_2}$ defined by (2.70) with the coefficients, μ_{jk}, satisfies the conjugate symmetry property provided that one sets

$$\chi^{(n)}_{-M_1/2,-M_2/2} = 0, \tag{2.78}$$

in the case when it is an imaginary number. Note that $\chi^{(n)}_{0,0} = 0$ in all cases. $\chi^{(n)}_{p_1,p_2}$ can be obtained for $p_1 = 0,\ldots,M_1-1$, $p_2 = 0,\ldots,M_2-1$ by first computing its values from (2.70) for $p_1 = 0,\ldots,M_1-1,$ and $p_2 = 0,\ldots,M_2-1,$, and then using (2.74) (if $\chi^{(n)}_{p_1,p_2}$ is imaginary).

2.5 Numerical analysis

We applied these methods to model the gravitational gradient using digital elevation data in the western and mid-western U.S. Figure 2.6 presents the terrain variations given by 1"×1" SRTM data. The previous results in Section 2.3 show that about half a degree for the extent of DEM is needed to obtain an accuracy of 1 E in the computation of gradients due to the residual terrain model. Since we only compare different methods to model gradients without considering the absolute accuracies, we limit the extent of the two areas to 10 arcmin. Thus, each area is a 10'×10'spherical patch that is approximated as a plane with grid intervals given, in meters, by $\Delta x_1 = 1''\eta\cos\varphi_m[m]$, $\Delta x_2 = 1''\eta[m]$, where φ_m is the mean latitude of the patch and η is the arcsec-to-meter conversion factor for a sphere of radius, $R = 6371$ km. The density of the topographic mass is assumed to be a constant value, $\rho = 2670\ kgm^{-3}$.

Here we still use the minimum elevation as the height reference in the area, so that it does not introduce a complicated geometric structure for the polyhedral method. The computation points are located at constant height, Δx_3, above the maximum elevation of the area: $x = \left(x_1, x_2, x_3^0\right)$, where $x_3^0 = h_{\max} + \Delta x_3$; in these tests, $\Delta x_3 = 10$ m (Figure 2.6). The computation altitudes are 4275.2 m and 1325.2 m for two tests respectively. The computation points have the same horizontal coordinates, (x_1, x_2), as the grid points of the terrain elevation data, and lie along a single profile at constant latitude across the center of each area, as shown in Figure 2.6. The heights of the two computation profiles with the underlying topography are shown in Figure 2.7, which also shows the gradient, Γ_{33}, at x_3^0; the other gradients have roughly similar magnitude. The topographic profile for Area 1 has a larger height variation than that for Area 2, but the gradient on the profile for Area 1 is smoother because the computation profile for Area 1 is further away from the underlying topographic surface.

An internal consistency check of all models is based on Laplace's equation. (Poisson's equation with zero density): $\Gamma_{11} + \Gamma_{22} + \Gamma_{33} = 0$. In all numerical computations discussed below we found that the maximum of the sum of the diagonal gradient components was no greater than 4×10^{-5} E (1 E =1 Eötvös $= 10^{-9}s^{-2}$), which can be attributed to accumulated computer round-off error.

An external evaluation of the gradient model requires a truth model that represents the actual gradients due to the topographic masses. One might consider using the triangulated terrain to represent the actual topographic surface. Petrovic's formulas (Petrovic, 1996; Tsoulis & Petrovic, 2001) provide exact corresponding gradients. On the other hand, this representation depends on the type of triangulation. For regular gridded elevation data, such as in this case, a straightforward triangulation yields grid diagonals either in the southeast-northwest direction, or in the southwest-northeast direction, or a combination of these. Figure 2.8 shows the differences in the gradients generated by these two alternative triangulations, where all diagonals are either in one or the other direction. The noticeably dissimilar character of the differences in these two areas is an artifact of the computation altitude and the properties of the terrain models. The differences reach 10-20 E for some of the gradients in the rough Area 1 even though the computation points are substantially further from the generating masses than in the smooth Area 2, where the differences are less than 1 E. These distinctive discrepancies in the two cases are caused by the properties of two terrain models. Figure 2.9 gives the reason for the large discrepancies in Area 1, showing that with all diagonals in the southeast-northwest orientation, the height differences along the diagonals are relatively more uniform than with the alternative orientation. In the smoother Area 2, the distribution of height differences along diagonals is almost independent of their orientation and the gradient differences are close to zero (see Figure 2.8). The essential conclusion is that a truth model eludes our present analysis. Such a model would have to depend uniquely on the data in a manner that best represents the consequent gravitational gradients. Data-dependent triangulation methods may be found in (Dyn et al., 1989), but additional analyses must determine if they optimally represent the gradients. Furthermore, one can reconstruct the topographic surface using B-spline functions such that an optimal topographic model can be used in deriving the gravitational gradients. Such studies are beyond the present scope of this research.

Figure 2.10 compares the gradients computed according to the right rectangular prism model against those generated by the polyhedron model (triangulated surface) using the southeast-northwest diagonal orientation. The right rectangular prism is centered on the grid points of the DEM data, so that for every grid point $(x'_{1,i}, x'_{2,i})$, the dimensions of prism are: Δx_1, Δx_2, and $h(x'_{1,i}, x'_{2,i}) - h_{\min}$ (we use the minimum elevation as the lower bound of the topographic mass). $h_{\min}$ is 1900.2 m and 1069.6 m for Area 1 and Area 2, respectively. Combining the results of Figure 2.8 and 2.10, we find that in Area 1 the rectangular prism model yields gradients much closer to those generated by the southeast-northwest diagonal triangulation than the alternative triangulations. This indicates that the former is perhaps a better truth representation of the topographic surface (for Area 1), if the rectangular prisms tend to represent an average of the terrain. The gradients should be computed from DEM extending a certain distance from the computation point (see Section 2.3.4). Since we only use a 10'×10' DEM data to compute the gradients at 600 points on the profile, there are big differences near the endpoints of the profiles (Figure 2.10). This can be avoided using a larger area for these points or disregarding points to the edges. Here we neglect 60 points at each end of the profiles in further statistical analysis of the results.

Figure 2.11 shows differences between the gradients derived from the rectangular numerical integration (RNI) according to (2.39) and those generated by the right rectangular prisms (RRP) according to (2.22) in Area 1 and Area 2. The differences between RNI and RRP in Area 2 are relatively larger (RMS: 0.2 E vs. 0.01 E) because the computation profile is closer to the terrain. For the same reason, the differences are smoother in Area 1 than those in Area 2. Differences between the rectangular numerical integration (2.39) and the triangular numerical integration (2.41) are presented in Figure 2.12 and show that they are significant at the few-Eötvös level only near the edge of the integration areas. The same results are obtained whether we choose either SE-NW or SW-NE diagonals in the triangular numerical integration. It verifies that the triangular numerical integration is almost independent of the orientation of the diagonals used in the triangulation (only the corner points of the overall rectangular area are weighted differently). Table 2.5 contains the statistics of the differences shown in Figs 2.10-2.12 (60 points are neglected at each side of the profiles such that the analysis is not contaminated by the edge effect).

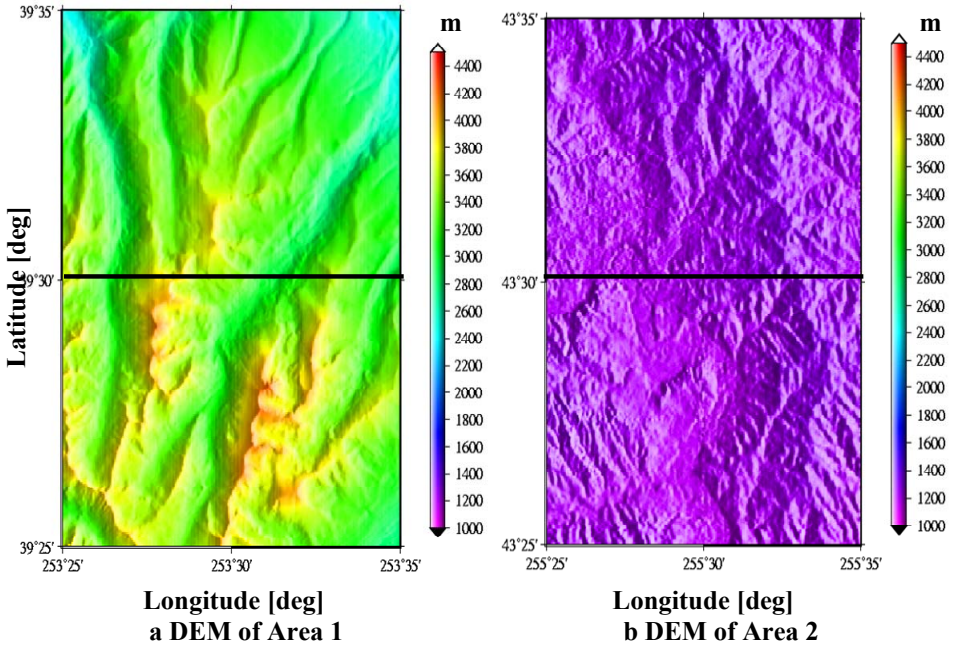

Figure 2.6: DEM for Area 1(central Colorado) and Area 2 (east Wyoming).

The statistics of Figure 2.12 shows that the RMS of differences between the rectangular and triangular numerical integration in Area 1 is much bigger than those in Area 2. The different terrain character that Area 1 is much rougher than Area 2 can contribute this difference between Area 1 and Area 2.

The prism and polyhedral methods and the numerical integrations could easily generate the gradients at points with arbitrary altitudes above the topographic surface. The point can be below the maximum elevation of the area as long as it is above the topographic surface. The FFT methods used here are more efficient only if all computation points lie on a regular grid at a constant altitude, and they require that this grid is above the entire terrain. The accuracy of these models can be assessed absolutely since in theory (if the series converge) the FFT method is identical to the rectangular numerical integration (provided that the circular convolution error is eliminated in Forsberg's method (Jekeli 1998; Haagmans et al., 1993), as done here). Figure 2.13 compares Parker's FFT method, (2.68), to the rectangular numerical integration model; while Forsberg's FFT method, (2.69), is assessed similarly in Figure 2.14. The critical parameter in these comparisons is the expansion order of the series. Clearly, there is a direct correlation between the required order of expansion (for comparable accuracy) and the roughness of the terrain. The RMS of differences between the FFT and rectangular numerical integration methods becomes smaller with an increase in the order of series expansion. Since Area 1 is rougher than Area 2, the FFT method needs higher orders of series expansion in order to obtain the same accuracy in Areas 1 than 2.

In Figure 2.13, the diagonal and off-diagonal gradients computed using partial series by Parker's FFT method behave in different ways. The off-diagonal gradients converge to those determined by the rectangular numerical integration, while the diagonal gradients fail to converge to the correct values. This is caused by the use of continuous, global Fourier transforms in (2.40). We derived the analytical form of the Fourier transform of $\frac{1}{r}$, and applied it to only discrete and locally extended data. The inconsistency between continuous, global Fourier transform and discrete Fourier transform contributes to biases for the diagonal gradients. Figure 2.14 shows that all gradients computed by Forsberg's FFT method converge as required to those determined by the rectangular numerical integration method

Table 2.5: Statistics for the differences in gradients shown in Figures 2.10, 2.11, and 2.12 along the profiles from 26 arcmin to 34 arcmin. All units are Eötvös [E].

	Difference between	Gradients	Mean	Rms	Min.	Max.
Area 1	Triangular (SE-NW	$\Delta\Gamma_{11}$	-0.2	0.23	-0.47	0.01
	diagonals) and rectangular	$\Delta\Gamma_{12}$	0.01	0.04	-0.12	0.14
	prisms (Fig 2.10, top)	$\Delta\Gamma_{13}$	-0.06	0.33	-1.35	0.67
		$\Delta\Gamma_{22}$	-0.02	0.04	-0.29	0.08
		$\Delta\Gamma_{23}$	-0.02	0.08	-0.95	0.93
		$\Delta\Gamma_{33}$	0.21	0.24	-0.01	0.44
	Rectangular prisms &	$\Delta\Gamma_{11}$	0	0.01	-0.01	0.02
	rectangular numerical	$\Delta\Gamma_{12}$	0	0.01	-0.01	0.02
	integration (Fig 2.11, top)	$\Delta\Gamma_{13}$	0	0.01	-0.03	0.01
		$\Delta\Gamma_{22}$	0	0.01	-0.02	0.02
		$\Delta\Gamma_{23}$	0	0.01	-0.02	0.04
		$\Delta\Gamma_{33}$	0	0.01	-0.03	0.01
	Rectangular & triangular	$\Delta\Gamma_{11}$	-0.20	0.22	-0.46	-0.01
	numerical integration	$\Delta\Gamma_{12}$	0.01	0.04	-0.03	0.14
	(Figure 2.12, top)	$\Delta\Gamma_{13}$	-0.06	0.33	-1.34	0.68
		$\Delta\Gamma_{22}$	-0.02	0.03	-0.05	0.08
		$\Delta\Gamma_{23}$	-0.02	0.03	-0.13	-0.01
		$\Delta\Gamma_{33}$	0.2	0.23	0.03	0.42
Area2	Triangular (SE-NW	$\Delta\Gamma_{11}$	-0.03	0.08	-0.33	0.26
	diagonals) and rectangular	$\Delta\Gamma_{12}$	0	0.07	-0.27	0.25
	prisms (Fig 2.10, bottom)	$\Delta\Gamma_{13}$	0	0.09	-0.28	0.36
		$\Delta\Gamma_{22}$	-0.12	0.24	-0.91	0.23
		$\Delta\Gamma_{23}$	0.07	0.32	-1.69	1.65
		$\Delta\Gamma_{33}$	0.15	0.28	-0.27	0.95
	Rectangular prisms &	$\Delta\Gamma_{11}$	0	0.06	-0.17	0.29
	rectangular numerical	$\Delta\Gamma_{12}$	0	0.05	-0.18	0.23
	integration (Fig 2.11,	$\Delta\Gamma_{13}$	0	0.08	-0.24	0.27
	bottom)	$\Delta\Gamma_{22}$	-0.11	0.22	-0.7	0.23
		$\Delta\Gamma_{23}$	0.02	0.13	-0.34	0.65
		$\Delta\Gamma_{33}$	0.11	0.23	-0.32	0.83
	Rectangular & triangular	$\Delta\Gamma_{11}$	-0.03	0.04	-0.16	-0.01
	numerical integration	$\Delta\Gamma_{12}$	0	0	0	0.02
	(Figure 2.12, bottom)	$\Delta\Gamma_{13}$	0	0.01	-0.03	0.03
		$\Delta\Gamma_{22}$	-0.01	0.01	-0.02	0
		$\Delta\Gamma_{23}$	0	0	0	0
		$\Delta\Gamma_{33}$	0.04	0.05	0.02	0.17

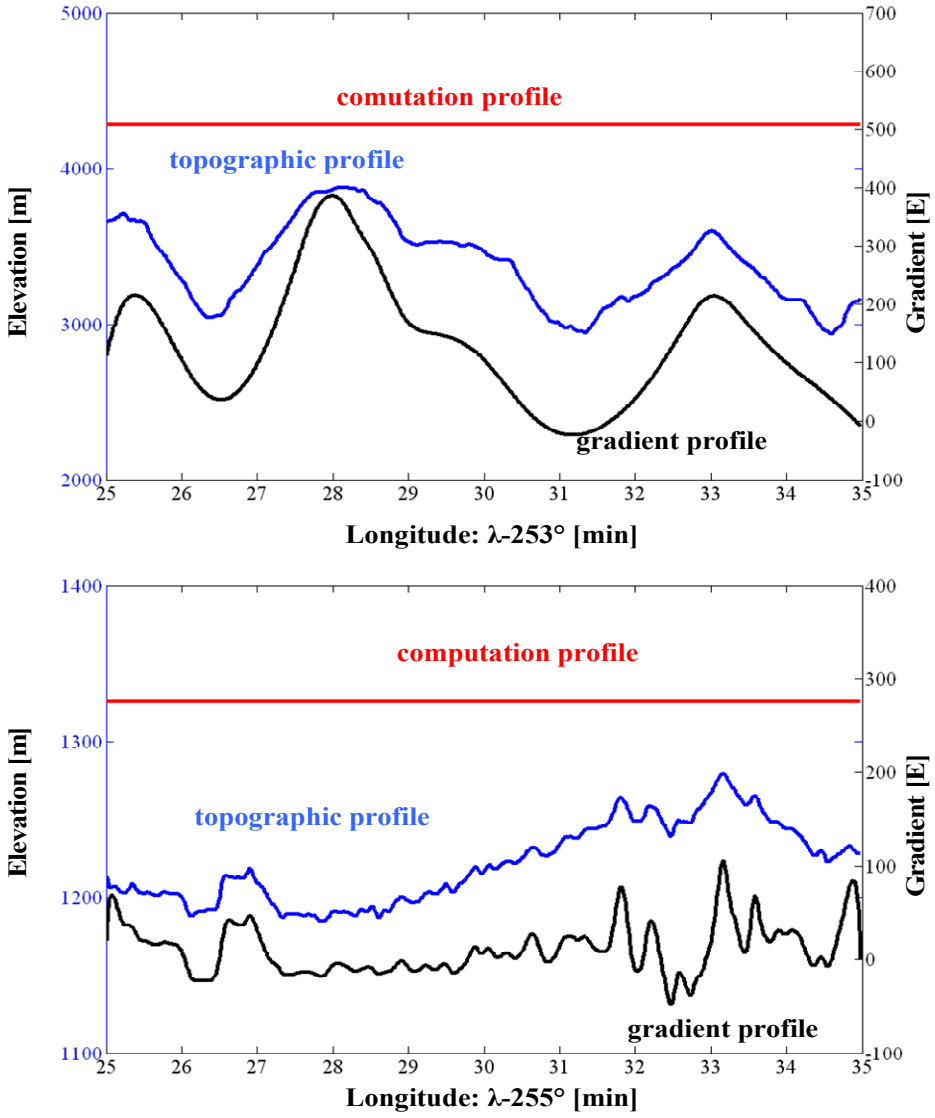

Figure 2.7: Topographic and fight profile.

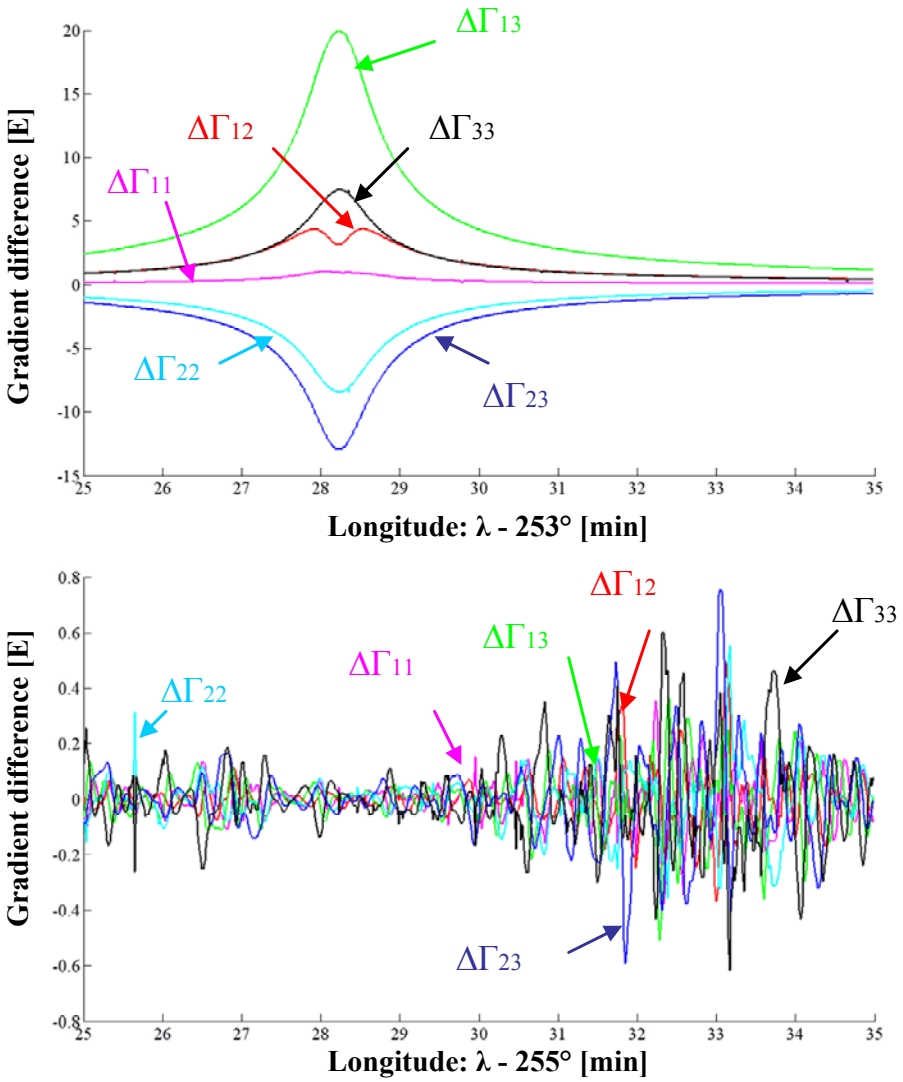

Figure 2.8: Differences between gradients derived from triangulated prisms of DEM using southwest-northeast and southeast-northwest diagonals. Top: profile in Aea 1; bottom: profile in Area 2.

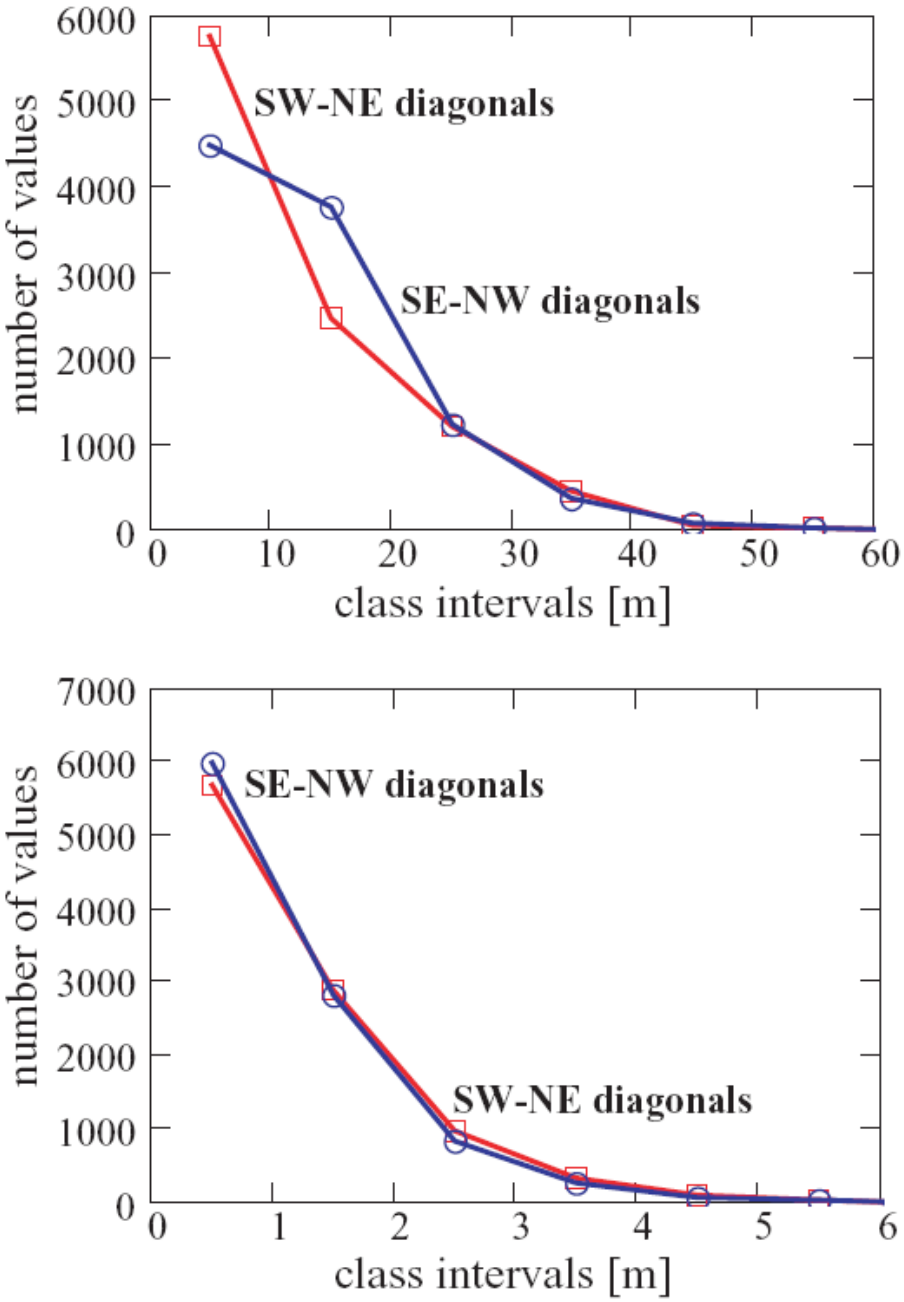

Figure 2.9: Histograms of height differences of diagonal endpoints for southwest-northeast and for southeast-northwest triangulations. The height differences are computed for the 100"×100" area centered on the profile point (with longitude difference from the west end of 28.3 arcmin) of the computation profile in Area 1 and on (with longitude difference from the west end of 28.3 arcmin) in Area 2 (bottom).

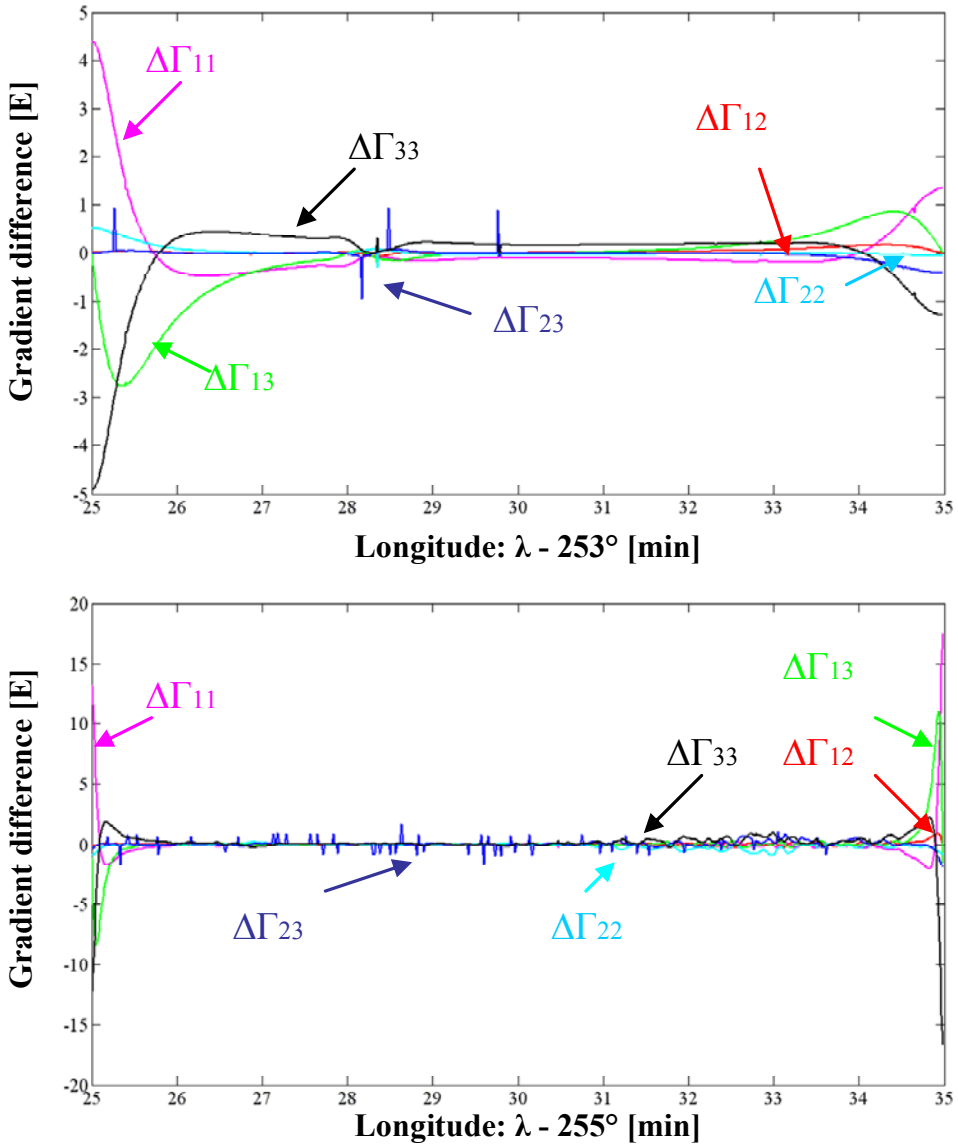

Figure 2.10**:** Differences along the computation profile between gradients derived from polyhedron model (southeast-northwest diagonals) and from rectangular prisms for Area 1 (top) and Area 2 (bottom).

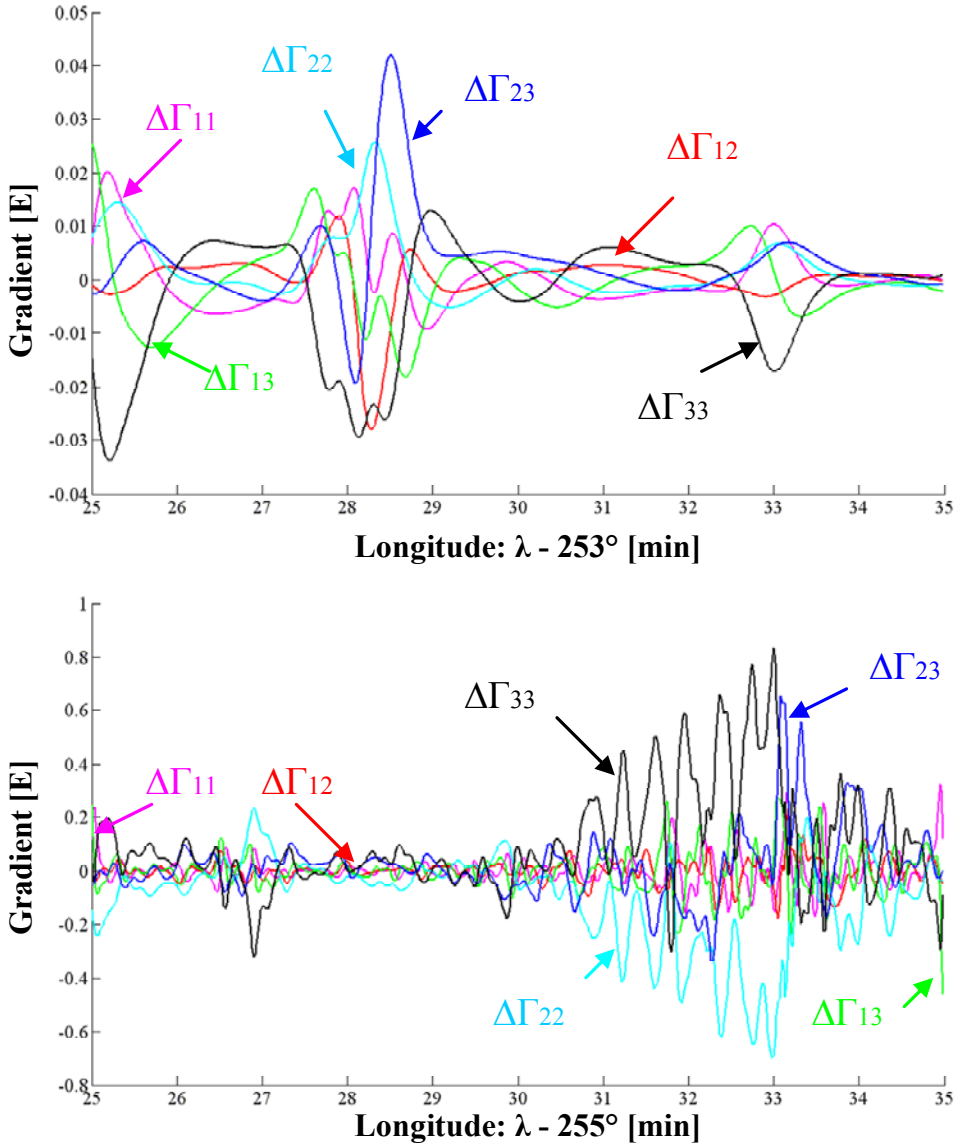

Figure 2.11: Differences along the computation profile between gradients derived from rectangular prisms and from the rectangular numerical integration for Area 1 (top) and Area 2 (bottom).

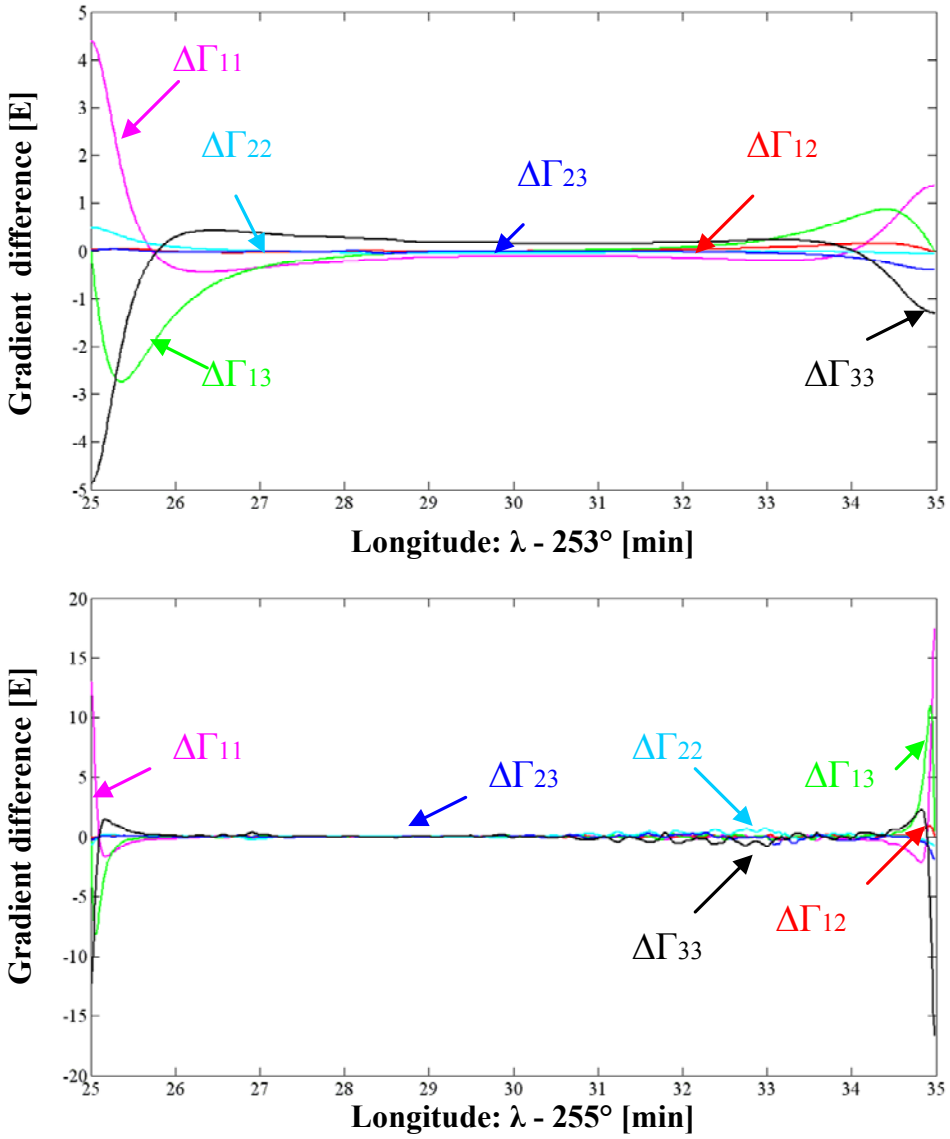

Figure 2.12: Differences along the computation profile between gradients derived from rectangular and triangular numerical integration for Area 1 (top) and Area 2 (bottom).

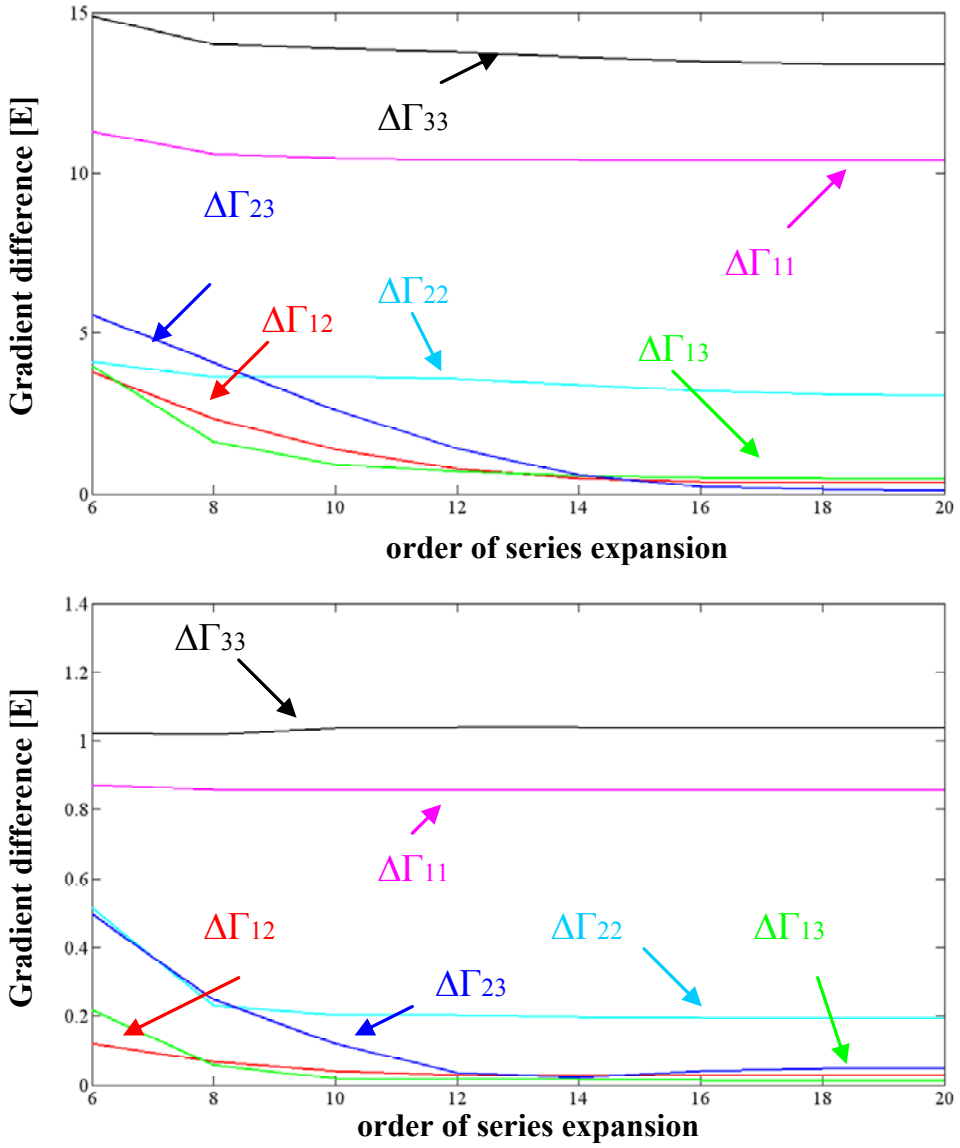

Figure 2.13: Root-Mean-Square (RMS) of the differences between gradients computed by rectangular numerical integration and by Parker's FFT method, as a function of the order of the series expansion of the latter, for Area 1 (top) and Area 2 (bottom).

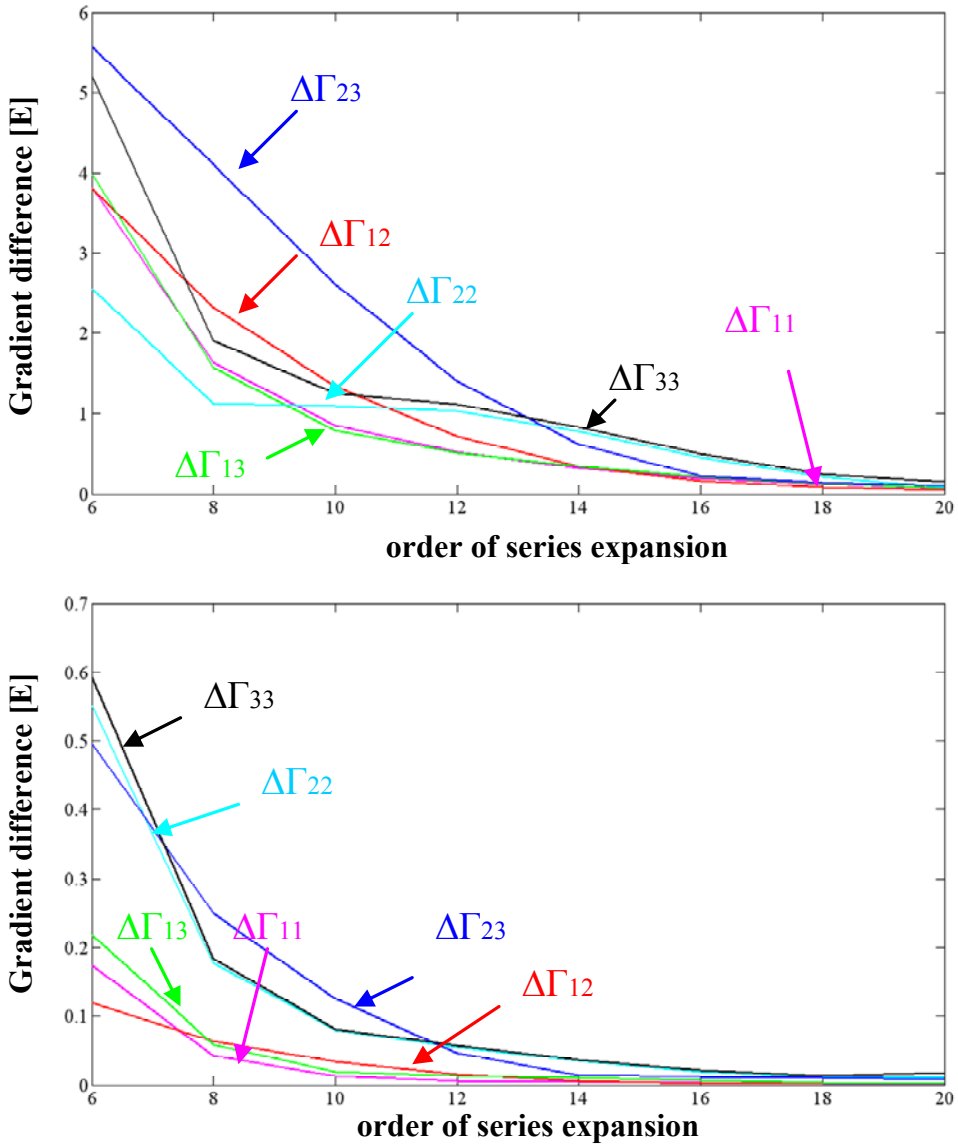

Figure 2.14: Root-mean-square (RMS) of the differences between gradients computed by rectangular numerical integration and by Forsberg's FFT method, as function of the order of the series of the latter for Area 1 (top) and Area 2 (bottom).

Finally we show in Table 2.6 the computation times required for each model. Such comparisons are at best of relative value since they are specific to the computer platform (in this case, dual Itanium 733MHz processors with 4 Gbyte RAM). Furthermore, the computer code is not necessarily equally efficient for all models, and some adaptive methods could be implemented for the numerical integrations that take advantage of the diminishing contributions of distant zones. Clearly, however, the FFT methods, automatically yielding results for all points on the data grid, are orders of magnitude faster than any of the other methods (if the latter would be used to compute gradients on the entire grid, not just a profile).

Table 2.6. Computation times for various gradient models based on topographic sources.

Method	Computation time [s]	Number of points*	Expansion order
Rectangular prisms	2875	600	N/A
Polyhedron (Petrovic)	2701	600	N/A
Rectangular numerical integration	1463	600	N/A
Triangular numerical integration	5733	600	N/A
Forsberg's FFT	1395	360000	20
Parker's FFT	168	360000	20

* Non-FFT methods compute gradients on a profile, FFT methods compute on the area.

2.6 Conclusion

A number of models can be used to represent the gravitational gradients generated by masses that are implied by topographic data. We investigated both finite element (fully analytic integration per elements) methods as well as hybrid analytical/numerical integration of Newtonian potential integrals. The numerical integration can be facilitated by implementing discrete Fourier transforms of the elevation data, if these and the evaluation points are on a regular Cartesian grid. Different formulations have different requirements, and they rely on a series expansion of the height.

For two test areas representing rough and moderate topographies, we analyzed these methods for computation points along profiles at constant altitude (above all the terrain). We found only small differences in the gradients between rectangular and triangular numerical integration (≤ 0.33 E (rms) along the profile in Area 1; ≤ 0.05 E (rms) along the profile in Area 2; see Figure 2.12). Triangulated finite element representations of the topographic masses, however, can generate significantly different gradients depending on the triangulation of the domain points (see Figure 2.8). On the other hand, very small differences were found between the rectangular prism and the rectangular numerical integration methods (≤ 0.01 E (rms) along the profile in Area 1; ≤ 0.23 E (rms) along the closer profile in Area 2; see Fig 2.11).

The FFT techniques ostensibly are faster, despite the many transforms that are evaluated in the series expansion with respect to topographic heights. Two types of expansion were tested and the one by Parker (1972) was found to yield unacceptable biases (see Figure 2.13) in the computed in-line gradients (compared to the rectangular integration method that it approximates). Both Tziavos et al. (1988) and Schwarz et al. (1990) also used the Parker FFT expansion, but were unaware of such biases since they made no comparison to the more rigorous rectangular numerical integration (or rectangular finite element method). For evaluation points close to rough terrain, quite high orders of expansion are required (14, in our case) to achieve sub-Eötvös accuracy with the alternative FFT method by Forsberg (1985); see Figure 2.14.

Forsberg's FFT method is consistent with the rectangular numerical integration method in computing the gravitational gradient of the topography. Petrovic's polyhedral method is identical to triangular prism method and yields less than one Eötvös difference (RMS) of the difference when compared to the rectangular prism and numerical integration methods. However, the results depend on the type of triangulation of the data points.

For applications in the cases like Area 1 and Area 2, it is recommended that the numerical integration and right rectangular prism methods be used to compute the gradients. If a large regular grid of elevation data is available and many points of the computation are needed, then Forsberg's FFT method can be an efficient way provided the computation altitude is constant.

CHAPTER 3

GRADIENT MODEL BASED ON GRAVITY

3.1 Introduction

In the previous chapter, we modeled the gravity gradients using digital elevation models through a forward computation based on straightforward Newtonian potential formulas and their derivatives. These models commonly neglect density variations within the topography as well as potentially significant density anomalies below the geoid. The mass anomaly is unknown, so we need to use additional information to account for the density anomalies of masses. In this chapter, we consider the determination of gravity gradients from a dense grid of gravity anomalies, which by definition represent the total mass density variation, limited only in the resolution that is determined by the data grid spacing. Modeling of the gradients, particularly at some altitude above ground, from surface gravity anomalies is based on numerical implementations of solutions to boundary-value problems in potential theory, such as Stokes' integral, least-squares collocation, and some Fourier transform methods, or even with radial-basis splines. Depending on the resolution, modeling the gravity gradient from gravity will account at least for the long wavelength density anomalies, which can then be combined with DEM modeling methods described in the last chapter. Furthermore, modeling of this type would offer a complementary if not alternative type of support in the validation of airborne gradiometry systems. We compare these various modeling techniques using simulated data, thus demonstrating techniques and principles, as well as limitations and advantages in each.

The gradient modeling in this chapter is based on the traditional solution to the boundary-value problem in geodesy, namely, Stokes' integral, and operational variations thereof, including spherical splines and least-squares collocation. The objective is to determine the full gradient tensor at aircraft altitude from ground gravity data and to assess the modeling methods using both real airborne gradiometer data and simulated fields.

3.2 Stokes' integral in spherical approximation

The disturbing potential, T, in the spherical approximation, is given by the Stokes integral (Heiskanen and Moritz, 1967),

$$T(r,\theta,\lambda)=\frac{R}{4\pi}\iint_{\sigma}\Delta g\left(\theta',\lambda'\right)S\left(r,\psi\right)d\sigma\,, \tag{3.1}$$

where $\Delta g\left(\theta',\lambda'\right)$ is the gravity anomaly on the geoid with the coordinates $\left(\theta',\lambda'\right)$, R is the mean radius of the earth, σ is the integration area on the unit sphere, $d\sigma=\sin\theta' d\theta' d\lambda'$, S is the generalized Stokes function, given by

$$S(\psi,r)=\frac{2R}{l}+\frac{R}{r}-\frac{3Rl}{r^2}-\frac{R^2}{r^2}\cos\psi\left(5+3\ln\frac{r-R\cos\psi+l}{2r}\right), \tag{3.2}$$

where $l=\sqrt{r^2+R^2-2Rr\cos\psi}$, and ψ is the spherical distance between the computation point, $\left(r,\theta,\lambda\right)$ and the integration point, $\left(\theta',\lambda'\right)$, given by

$$\psi=\cos^{-1}\left(\cos\theta\cos\theta'+\sin\theta\sin\theta'\cos(\lambda-\lambda')\right). \tag{3.3}$$

According to (2.7), we get the disturbing gradient

$$\delta\Gamma_{jk}=\frac{R}{4\pi}\frac{\partial^2}{\partial x_j\partial x_k}\iint_{\sigma}\Delta g\left(\theta',\lambda'\right)S\left(r,\psi\right)d\sigma\,. \tag{3.4}$$

The generalized Stokes function is used to incorporate the upward continuation mechanism for the evaluation of gradients at aircraft altitude. It is in terms of spherical coordinates, but the gradient operator is given in the local Cartesian coordinate system. A transformation of derivatives from spherical coordinates to the Cartesian coordinates is necessary. (3.5) and (3.6) show this transformation of spherical coordinates into local Cartesian coordinates with axes pointing east, north, and up. The gradient operator is:

$$\nabla=\begin{pmatrix}\dfrac{\partial}{\partial x_1}\\[2mm]\dfrac{\partial}{\partial x_2}\\[2mm]\dfrac{\partial}{\partial x_3}\end{pmatrix}=\begin{pmatrix}\dfrac{1}{r\sin\theta}\dfrac{\partial}{\partial\lambda}\\[2mm]-\dfrac{1}{r}\dfrac{\partial}{\partial\theta}\\[2mm]\dfrac{\partial}{\partial r}\end{pmatrix}. \tag{3.5}$$

The second-order derivatives are (Rummel, 1997)

$$\frac{\partial^2}{\partial x_1^{\,2}}=\frac{\cot\theta}{r^2}\frac{\partial}{\partial\theta}+\frac{1}{r}\frac{\partial}{\partial r}+\frac{1}{r^2\sin^2\theta}\frac{\partial^2}{\partial\lambda^2},$$

$$\frac{\partial^2}{\partial x_1\partial x_2}=\frac{\partial^2}{\partial x_2\partial x_1}=\frac{\cot\theta}{r^2\sin\theta}\frac{\partial}{\partial\lambda}-\frac{1}{r^2\sin\theta}\frac{\partial^2}{\partial\theta\partial\lambda},$$

$$\frac{\partial^2}{\partial x_1\partial x_3}=\frac{\partial^2}{\partial x_3\partial x_1}=-\frac{1}{r^2\sin\theta}\frac{\partial}{\partial\lambda}+\frac{1}{r\sin\theta}\frac{\partial^2}{\partial\lambda\partial r},$$

$$\frac{\partial^2}{\partial x_2^{\,2}}=\frac{1}{r}\frac{\partial}{\partial r}+\frac{1}{r^2}\frac{\partial^2}{\partial\theta^2},$$

$$\frac{\partial^2}{\partial x_2\partial x_3}=\frac{\partial^2}{\partial x_3\partial x_2}=\frac{1}{r^2}\frac{\partial}{\partial\theta}-\frac{1}{r}\frac{\partial^2}{\partial\theta\partial r},$$

$$\frac{\partial^2}{\partial x_3^{\,2}} = \frac{\partial^2}{\partial r^2}\,. \tag{3.6}$$

According to (3.6), the gradients can be implemented from the derivatives of Stokes' function with respect to spherical coordinates. Those derivatives can be easily derived from the relation between the spherical distance ψ and the spherical coordinates (see figure 3.1). The derivation can be found in Appendix A.

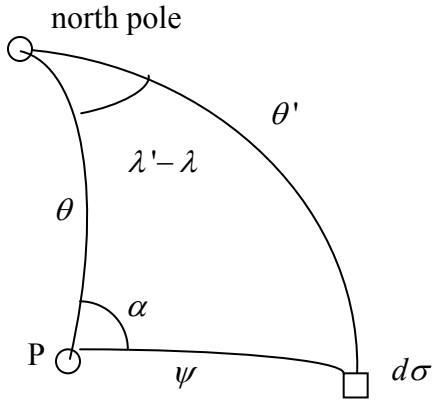

Figure 3.1: The relation between spherical and polar coordinates (ψ,α) on the sphere.

Inserting (A.29) ~ (A.35) into (3.6) and then applying (3.6) into (3.4), finally we obtain the disturbing gradient tensor elements as follows:

$$\frac{\partial^2 T(\theta,\lambda,r)}{\partial x_1^{\,2}} = \frac{R}{4\pi}\iint_\sigma \Delta g(\theta',\lambda')\left(\frac{1}{r}\frac{\partial}{\partial r} + \frac{\cot\psi\cos^2\alpha}{r^2}\frac{\partial}{\partial\psi} + \frac{\sin^2\alpha}{r^2}\frac{\partial^2}{\partial\psi^2}\right)S(\psi,r)\,d\sigma\,,$$

$$\frac{\partial^2 T(\theta,\lambda,r)}{\partial x_1\partial x_2} = \frac{R}{4\pi}\iint_\sigma \Delta g(\theta',\lambda')\left(\frac{\cot\psi\cos\alpha\sin\alpha}{r^2}\frac{\partial}{\partial\psi} - \frac{\cos\alpha\sin\alpha}{r^2}\frac{\partial^2}{\partial\psi^2}\right)S(\psi,r)\,d\sigma\,,$$

$$\frac{\partial^2 T(\theta,\lambda,r)}{\partial x_1\partial x_3} = \frac{R}{4\pi}\iint_\sigma \Delta g(\theta',\lambda')\left(-\frac{\sin\alpha}{r^2}\frac{\partial}{\partial\psi} + \frac{\sin\alpha}{r}\frac{\partial^2}{\partial\psi\partial r}\right)S(\psi,r)\,d\sigma\,,$$

$$\frac{\partial^2 T(\theta,\lambda,r)}{\partial x_2^{\,2}} = \frac{R}{4\pi}\iint_\sigma \Delta g(\theta',\lambda')\left(\frac{1}{r}\frac{\partial}{\partial r} + \frac{\sin^2\alpha\cot\psi}{r^2}\frac{\partial}{\partial\psi} + \frac{\cos^2\alpha}{r^2}\frac{\partial^2}{\partial\psi^2}\right)S(\psi,r)\,d\sigma\,,$$

$$\frac{\partial^2 T(\theta,\lambda,r)}{\partial x_2\partial x_3} = \frac{R}{4\pi}\iint_\sigma \Delta g(\theta',\lambda')\left(-\frac{\cos\alpha}{r}\frac{\partial^2}{\partial\psi\partial r} + \frac{\cos\alpha}{r^2}\frac{\partial}{\partial\psi}\right)S(\psi,r)\,d\sigma\,,$$

$$\frac{\partial^2 T(\theta,\lambda,r)}{\partial x_3^{\,2}} = \frac{R}{4\pi}\iint_\sigma \Delta g(\theta',\lambda')\frac{\partial^2 S(\psi,r)}{\partial r^2}\,d\sigma\,. \tag{3.7}$$

where the generalized Stokes function, $S(\psi,r)$, is independent of the azimuth, α, so the derivatives with respect to α are omitted. For simplicity, we denote with an appropriate subscript symbol the derivative of the Stokes function. Then these derivatives can be straightforwardly derived:

$$S_r = \frac{\partial S}{\partial r} = \frac{-2R(r-R\cos\psi)}{l^3} - \frac{R}{r^2} - \frac{3R}{lr} + \frac{6Rl}{r^3} + \frac{R^2\cos\psi(13+6\ln\frac{r-R\cos\psi+l}{2r})}{r^3}, \quad (3.8)$$

$$S_{r^2} = \frac{\partial^2 S}{\partial r^2} = \frac{R}{l^3} + \frac{6R(r-R\cos\psi)^2}{l^5} + \frac{2R}{r^3} + \frac{9R}{lr^2} - \frac{18Rl}{r^4} - \frac{45R^2\cos\psi}{r^4} - \frac{3R^2\cos\psi}{l^3 r}$$
$$- \frac{18R^2\cos\psi\ln\frac{r-R\cos\psi+l}{2r}}{r^4}, \quad (3.9)$$

$$S_\psi = \frac{\partial S}{\partial \psi} = -\frac{2R^2 r\sin\psi}{l^3} - \frac{3R^2\sin\psi}{lr} + \frac{R^2\sin\psi(5+3\ln\frac{r-R\cos\psi+l}{2r})}{r^2}$$
$$- \frac{3R^3\cos\psi\sin\psi}{r^2(r-R\cos\psi+l)} - \frac{3R^3\cos\psi\sin\psi}{rl(r-R\cos\psi+l)}, \quad (3.10)$$

$$S_{\psi^2} = \frac{\partial^2 S}{\partial \psi^2} = \frac{6R^3 r^2\sin^2\psi}{l^5} + \frac{3R^3\sin^2\psi - 2R^2 r\cos\psi}{l^3} - \frac{3R^2\cos\psi}{lr}$$
$$+ \frac{R^2\cos\psi(5+3\ln\frac{r-R\cos\psi+l}{2r})}{r^2} + \frac{3R^3(l+r)(2\sin^2\psi-\cos^2\psi)}{r^2 l(r-R\cos\psi+l)}, \quad (3.11)$$
$$+ \frac{3R^4\cos\psi\sin^2\psi(l+r)^2}{r^2 l^2(r-R\cos\psi+l)^2} + \frac{3R^4\cos\psi\sin^2\psi}{l^3(r-R\cos\psi+l)}$$

$$S_{r\psi} = \frac{\partial^2 S}{\partial \psi \partial r} = \frac{R^2\sin\psi}{l^3} + \frac{6R^2 r\sin\psi(r-R\cos\psi)}{l^5} + \frac{6R^2\sin\psi}{lr^2} - \frac{13R^2\sin\psi}{r^3}$$
$$- \frac{6R^2\sin\psi\ln\frac{r-R\cos\psi+l}{2r}}{r^3} + \frac{6R^3\cos\psi\sin\psi}{(r-R\cos\psi+l)r^3} + \frac{6R^3\cos\psi\sin\psi}{(r-R\cos\psi+l)lr^2}. \quad (3.12)$$

Similar derivations for the first derivatives of Stokes function can also be found in Eqn.6-41 and Eqn.6-42 (Heiskanen and Moritz, 1967). We reformulate (3.7) to clarify the numerical evaluation:

$$\frac{\partial^2 T(\theta,\lambda,r)}{\partial x_1^{\,2}} = \frac{R}{4\pi}\iint_\sigma \Delta g(\theta',\lambda')\left(C_{1,\psi}S_\psi + C_{1,r}S_r + C_{1,\psi^2}S_{\psi^2}\right)d\sigma,$$

$$\frac{\partial^2 T(\theta,\lambda,r)}{\partial x_1 \partial x_2} = \frac{R}{4\pi}\iint_\sigma \Delta g(\theta',\lambda')\left(C_{2,\psi}S_\psi + C_{2,\psi^2}S_{\psi^2}\right)d\sigma,$$

$$\frac{\partial^2 T(\theta,\lambda,r)}{\partial x_1 \partial x_3} = \frac{R}{4\pi}\iint_\sigma \Delta g\left(\theta',\lambda'\right)\left(C_{3,\psi}S_\psi + C_{3,r\psi}S_{r\psi}\right)d\sigma,$$

$$\frac{\partial^2 T(\theta,\lambda,r)}{\partial {x_2}^2} = \frac{R}{4\pi}\iint_\sigma \Delta g(\theta',\lambda')\left(C_{4,r}S_r + C_{4,\psi^2}S_{\psi^2} + C_{4,\psi}S_\psi\right)d\sigma,$$

$$\frac{\partial^2 T(\theta,\lambda,r)}{\partial x_2 \partial x_3} = \frac{R}{4\pi}\iint_\sigma \Delta g(\theta',\lambda')\left(C_{5,r\psi}S_{r\psi} + C_{5,\psi}S_\psi\right)d\sigma,$$

$$\frac{\partial^2 T(\theta,\lambda,r)}{\partial {x_3}^2} = \frac{R}{4\pi}\iint_\sigma \Delta g\left(\theta',\lambda'\right)C_{6,r^2}S_{r^2}d\sigma, \tag{3.13}$$

where

$$C_{1,r} = \frac{1}{r}$$

$$C_{1,\psi} = \frac{\cot\psi\cos^2\alpha}{r^2}, \tag{3.14}$$

$$C_{1,\psi^2} = \frac{\sin^2\alpha}{r^2}$$

$$C_{2,\psi} = \frac{\cot\psi\cos\alpha\sin\alpha}{r^2}, \tag{3.15}$$

$$C_{2,\psi^2} = -\frac{\cos\alpha\sin\alpha}{r^2}$$

$$C_{3,\psi} = -\frac{\sin\alpha}{r^2}, \tag{3.16}$$

$$C_{3,r\psi} = \frac{\sin\alpha}{r}$$

$$C_{4,r} = \frac{1}{r}$$

$$C_{4,\psi} = \frac{\sin^2\alpha\cot\psi}{r^2}, \tag{3.17}$$

$$C_{4,\psi^2} = \frac{\cos^2\alpha}{r^2}$$

$$C_{5,\psi} = \frac{\cos\alpha}{r^2}$$

$$C_{5,r\psi} = -\frac{\cos\alpha}{r}, \tag{3.18}$$

$$C_{6,r^2} = 1 \tag{3.19}$$

Clearly, when $\psi = 0$ and $r = R$, there are singularities in (3.13). A way to solve these singularities would be separating the effect of the inner zone from the computation of gradients (Heiskanen and Moritz, 1967). This is developed in the next section.

In summary, the gradient disturbances can be obtained from Stokes' integral by taking the derivatives of Stokes' function. In this way, the ground gravity data can be used to compute gradients at an arbitrary altitude. When (3.13) is used to compute the gradients, the integral is approximated numerically using discrete data values, usually on

a grid. This approximation will depend on the spacing and extent of the data, and on the altitude of the computation point. Further discussions will be given in the following section.

3.3 Stokes' integral in planar approximation

Because the gradient disturbances are primarily a local signal, we can usually use the planar surface to replace the geoid if the local geoid surface is smooth enough. The Stokes function can be expressed in terms of the local Cartesian coordinates in planar approximation degenerates into

$$S(\psi, r) \approx \frac{2R}{l_0}, \tag{3.20}$$

where $l_0 = \sqrt{\left(x_1 - x_1^{'}\right)^2 + \left(x_2 - x_2^{'}\right)^2 + {x_3}^2}$. It still incorporates the upward continuation to evaluate the gradient at an airborne altitude, a few hundred meters to several kilometers. Now the planar approximation for Stokes' integral formula is

$$T(x_1, x_2, x_3) = \frac{1}{4\pi R} \iint_E \Delta g(x_1^{'}, x_2^{'}) S\left(x_1, x_2, x_3, x_1^{'}, x_2^{'}\right) dx_1^{'} dx_2^{'}, \tag{3.21}$$

where E is the integration area, and $S\left(x_1, x_2, x_3, x_1^{'}, x_2^{'}\right) = \frac{2R}{l_0}$. The gradient disturbances can be expressed as

$$\delta\Gamma_{jk} = \frac{1}{2\pi} \iint_E \Delta g\left(x_1^{'}, x_2^{'}\right) \frac{\partial^2}{\partial x_j \partial x_k} \left(\frac{1}{l_0}\right) dx_1^{'} dx_2^{'}, \tag{3.22}$$

with the diagonal and off-diagonal gradients components being

$$\delta\Gamma_{jj} = \frac{1}{2\pi} \iint_E \Delta g\left(x_1^{'}, x_2^{'}\right) \frac{\left(3\left(x_j - x_j^{'}\right)^2 - {l_0}^2\right)}{{l_0}^5} dx_1^{'} dx_2^{'}, \tag{3.23}$$

and

$$\delta\Gamma_{jk} = \frac{1}{2\pi} \iint_E \Delta g\left(x_1^{'}, x_2^{'}\right) \frac{\left(3\left(x_j - x_j^{'}\right)\left(x_k - x_k^{'}\right)\right)}{{l_0}^5} dx_1^{'} dx_2^{'}. \tag{3.24}$$

In practice, gravity data are given at discrete points on a regular grid on the geoid. The intervals of the grid are Δx_1 and Δx_2. Gravity data are $\Delta g_{n,m}$ at grid point $\left(x_{1,n} = (n-1)\Delta x_1, x_{2,m} = (m-1)\Delta x_2, x_3 = 0\right)$ with $n = 1, ..., N$ and $m = 1, ..., M$. We may either approximate the integral as in (2.40), or assume $\Delta g_{n,m}$ is constant over a grid compartment and analytically integrate the derivatives of Stokes' function over the compartments. Employing the second method, the discretization of (3.22) can be formulated as follows:

$$\delta\Gamma_{jk} = \sum_{n=1}^{N} \sum_{m=1}^{M} \frac{\Delta g_{n,m} \cdot K_{n,m}^{jk}}{2\pi}, \tag{3.25}$$

with $K_{nm}^{jk} = \int_{x_{2,m}-\Delta x_2/2}^{x_{2,m}+\Delta x_2/2} \int_{x_{1,n}-\Delta x_1/2}^{x_{1,n}+\Delta x_1/2} \frac{\partial^2}{\partial x_j \partial x_k}\left(\frac{1}{l_0}\right) dx_1^{'} dx_2^{'}$. (3.26)

Assuming $x_3 > 0$, and integrating (3.26) in a way similar to the rectangular prism method described in Chapter 2, we obtain the kernel functions K^{jk}

$$K^{11} = \frac{-(x_1^{'} - x_1)(x_2^{'} - x_2)}{a_1^2 l_0}\Bigg|_{x_1^{'}=x_{1,n}-\Delta x_1/2}^{x_{1,n}+\Delta x_1/2} \Bigg|_{x_2^{'}=x_{2,m}-\Delta x_2/2}^{x_{2,m}+\Delta x_2/2},$$

$$K^{12} = \frac{1}{l_0}\Bigg|_{x_1^{'}=x_{1,n}-\Delta x_1/2}^{x_{1,n}+\Delta x_1/2} \Bigg|_{x_2^{'}=x_{2,m}-\Delta x_2/2}^{x_{2,m}+\Delta x_2/2},$$

$$K^{13} = \frac{x_3(x_2^{'} - x_2)}{a_1^2 l_0}\Bigg|_{x_1^{'}=x_{1,n}-\Delta x_1/2}^{x_{1,n}+\Delta x_1/2} \Bigg|_{x_2^{'}=x_{2,m}-\Delta x_2/2}^{x_{2,m}+\Delta x_2/2},$$

$$K^{22} = \frac{-(x_1^{'} - x_1)(x_2^{'} - x_2)}{a_2^2 l_0}\Bigg|_{x_1^{'}=x_{1,n}-\Delta x_1/2}^{x_{1,n}+\Delta x_1/2} \Bigg|_{x_2^{'}=x_{2,m}-\Delta x_2/2}^{x_{2,m}+\Delta x_2/2},$$

$$K^{23} = \frac{x_3(x_1^{'} - x_1)}{a_2^2 l_0}\Bigg|_{x_1^{'}=x_{1,n}-\Delta x_1/2}^{x_{1,n}+\Delta x_1/2} \Bigg|_{x_2^{'}=x_{2,m}-\Delta x_2/2}^{x_{2,m}+\Delta x_2/2},$$

$$K^{33} = \left(\frac{(x_1^{'} - x_1)(x_2^{'} - x_2)}{a_1^2 l_0} + \frac{(x_1^{'} - x_1)(x_2^{'} - x_2)}{a_2^2 l_0}\right)\Bigg|_{x_1^{'}=x_{1,n}-\Delta x_1/2}^{x_{1,n}+\Delta x_1/2} \Bigg|_{x_2^{'}=x_{2,m}-\Delta x_2/2}^{x_{2,m}+\Delta x_2/2}, \quad (3.27)$$

where $a_1 = \sqrt{\left(x_1^{'} - x_1\right)^2 + x_3^2}$ and $a_2 = \sqrt{\left(x_2^{'} - x_2\right)^2 + x_3^2}$. From (3.25), we see that the gradient can be obtained from the summation of the gravity anomalies weighed by the second-order derivative of the inverse distance. (3.27) gives analytical weight functions (kernel functions) for each gradient. For the gradient derived from (3.22), Laplace's equation is an internal check for the numerical evaluation of the diagonal elements of the gradient tensor.

If we compute the gradient at the altitude, x_3, there are no singularities in (3.22). When $x_3 = 0$, there are strong singularities in (3.22) at $x_1 = x_1^{'}$, $x_2 = x_2^{'}$, which corresponds to the situation of $\psi = 0$ and $r = R$ in (3.13). We split off the effect of this inner most zone, E_i, which is assumed to be a circle of radius ψ_0 around the computation point. In this area, l_0 becomes the horizontal distance, $s = \sqrt{\left(x_1 - x_1^{'}\right)^2 + \left(x_2 - x_2^{'}\right)^2}$. Obviously we have $s_0 = R\psi_0$. Thus the disturbing gradient is split into two parts:

$$\delta\Gamma_{jk} = \left(\delta\Gamma_{jk}\right)_i + \left(\delta\Gamma_{jk}\right)_e, \quad (3.28)$$

with $\left(\delta\Gamma_{jk}\right)_i = \frac{1}{2\pi}\iint_{E_i} \Delta g\left(\theta^{'}, \lambda^{'}\right) \frac{\partial^2}{\partial x_j \partial x_k}\left(\frac{1}{s}\right) dx_1^{'} dx_2^{'}$,

and $\left(\delta\Gamma_{jk}\right)_e = \frac{1}{2\pi}\iint_{E_e} \Delta g\left(\theta^{'}, \lambda^{'}\right) \frac{\partial^2}{\partial x_j \partial x_k}\left(\frac{1}{s}\right) dx_1^{'} dx_2^{'}$,

where E_e is the inner zone and outer zone on the unit sphere. Since $\frac{1}{s}$ is independent of x_3, we can not derive $\delta\Gamma_{13}$ and $\delta\Gamma_{23}$ from (3.28), and their development is discussed in the following part. The integral of other gradient components can be evaluated over the outer zone can be computed from (3.22). Using polar coordinates, s, α, the element of area becomes $dx_1' dx_2' = sdsd\alpha$ .The rectangular coordinates, x_1, x_2 become $x_1 = s\cos\alpha$, $x_2 = s\sin\alpha$. According to (3.23) and (3.24), we have

$$\left(\delta\Gamma_{11}\right)_i = \frac{1}{2\pi}\int_0^{2\pi}\int_0^{s_0}\frac{\Delta g}{s^2}\left(3\cos^2\alpha - 1\right)dsd\alpha,$$

$$\left(\delta\Gamma_{12}\right)_i = \frac{1}{2\pi}\int_0^{2\pi}\int_0^{s_0}\frac{\Delta g}{s^2}\left(3\sin\alpha\cos\alpha\right)dsd\alpha,$$

$$\left(\delta\Gamma_{22}\right)_i = \frac{1}{2\pi}\int_0^{2\pi}\int_0^{s_0}\frac{\Delta g}{s^2}\left(3\sin^2\alpha - 1\right)dsd\alpha,$$

$$\left(\delta\Gamma_{33}\right)_i = -\frac{1}{2\pi}\int_0^{2\pi}\int_0^{s_0}\frac{\Delta g}{s^2}dsd\alpha. \tag{3.29}$$

We expand Δg into a Taylor expansion series at the computation point P:

$$\Delta g = \Delta g_P + x_1 g_1 + x_2 g_2 + \frac{1}{2}\left(x_1^2 g_{11} + 2x_1 x_2 g_{12} + x_2^2 g_{22}\right) + \cdots, \tag{3.30}$$

where $g_1 = \frac{\partial\Delta g}{\partial x_1}$, $g_2 = \frac{\partial\Delta g}{\partial x_2}$, $g_{11} = \frac{\partial^2\Delta g}{\partial x_1^2}$, $g_{12} = \frac{\partial^2\Delta g}{\partial x_1\partial x_2}$ and $g_{22} = \frac{\partial^2\Delta g}{\partial x_2^2}$. This can be further written as:

$$\Delta g = \Delta g_P + s\left(g_1\cos\alpha + g_2\sin\alpha\right) + \frac{s^2}{2}\left(g_{11}\cos^2\alpha + 2g_{12}\sin\alpha\cos\alpha + g_{22}\sin^2\alpha\right) + \cdots, \tag{3.31}.$$

Inserting (3.32) into (3.30), performing the integration, and retaining only the lowest nonvanishing terms (assuming high-order terms are not as significant as the lowest nonvanishing terms), we obtain

$$\left(\delta\Gamma_{11}\right)_i = \frac{5g_{11} - g_{22}}{16}\cdot s_0,$$

$$\left(\delta\Gamma_{12}\right)_i = \frac{3}{8}g_{12}\cdot s_0,$$

$$\left(\delta\Gamma_{22}\right)_i = \frac{5g_{22} - g_{11}}{16}\cdot s_0,$$

$$\left(\delta\Gamma_{33}\right)_i = -\frac{g_{11} + g_{22}}{4}\cdot s_0, \tag{3.32}$$

In planar approximation, we have $\Delta g \approx -\frac{\partial T}{\partial r}$. Letting $\frac{\partial T}{\partial x_3} \approx \frac{\partial T}{\partial r}$, we have

$$\delta\Gamma_{13} \approx -\frac{\partial\Delta g}{\partial x_1} = -g_1,$$

$$\delta\Gamma_{23} \approx -\frac{\partial\Delta g}{\partial x_2} = -g_2. \tag{3.33}$$

Clearly (3.33) can be employed to compute the entire gradient disturbance components, $\delta\Gamma_{13}$ and $\delta\Gamma_{23}$, when the computation point is on the geoid. On the other hand, (3.32) cab be used to compute the gradient disturbance of the other components due to the inner zone part. The horizontal derivatives of gravity anomaly can be obtained approximately from the grid data, e.g. given $\Delta g_{n,m}$, $n=1,\ldots,N$, $m=1,\ldots,M$, the horizontal derivatives are approximately

$$g_{1_{n,m}}=\frac{\Delta g_{n+1,m}-\Delta g_{n-1,m}}{2\Delta x_1}\quad,\quad g_{2_{n,m}}=\frac{\Delta g_{n,m+1}-\Delta g_{n,m-1}}{2\Delta x_2}\quad,\quad g_{11_{n,m}}=\frac{g_{1_{n+1,m}}-g_{1_{n-1,m}}}{2\Delta x_1}\quad,$$

$g_{12_{n,m}}=\frac{g_{1_{n,m+1}}-g_{1_{n,m-1}}}{2\Delta x_2}$ and $g_{22_{n,m}}=\frac{g_{2_{n,m+1}}-g_{2_{n-1,m-1}}}{2\Delta x_2}$.

We can also use second-order spline interpolation or Fourier transforms to get the horizontal derivatives of the gravity anomaly.

3.4 Spherical spline model

3.4.1 Introduction to spherical spline

Spherical splines are based on the radial basis functions, which are defined on a sphere and depend on the spherical distance from a given point. Thus they can be expressed as infinite series of Legendre polynomials. They have been developed and applied for interpolation and smoothing of discrete data given on the sphere (Freeden, 1981, 1990, 1998; Wahba, 1982, 1984). Spherical splines have proved to be useful in solving the boundary value problems of the potential theory from discrete data (Freeden, 1987). Spherical splines overcome the disadvantages of the spherical harmonic model where each coefficient in this model depends on all the data over the entire sphere, and they provide an alternative model to allow local data to be changed without changing the model globally (Jekeli, 2005).

Spherical splines are established in the frame of a Hilbert space with reproducing kernels (Schreiner, 1997; Jekeli, 2005). Let $\Omega=\left\{\xi\in\mathbb{R}^3\,\middle|\,|\xi|=1\right\}$ be the unit sphere in $\mathbb{R}^3$. Let $\Im^2(\Omega)$ be the space of square-integrable functions on Ω. Let $\left\{Y_{n,1},\ldots,Y_{n,2n+1}\right\}$ be an $\Im^2(\Omega)$ -orthonormal system of spherical harmonics of degree n. Continuous functions, f,g, defined on the sphere, Ω, have spherical harmonic expansions formulated respectively as:

$$f(\xi)=\sum_{l=0}^{\infty}\sum_{m=-l}^{l}F_{lm}Y_{lm}(\xi),\tag{3.34}$$

$$g(\xi)=\sum_{l=0}^{\infty}\sum_{m=-l}^{l}G_{lm}Y_{lm}(\xi),\tag{3.35}$$

and their harmonic coefficients satisfy:

$$\sum_{l=0}^{\infty}A_l^2\sum_{m=-l}^{l}F_{lm}^2<\infty,\tag{3.36}$$

for a given set of numbers A_l. An inner product for these functions is constructed as

$$\left(f,g\right)_{\mathrm{H}\left(\{A_l\},\Omega\right)}=\sum_{l=0}^{\infty}A_l^2\sum_{m=-l}^{l}F_{lm}G_{lm}\ . \tag{3.37}$$

A reproducing kernel for this space is given by the uniformly convergent series:

$$K_A\left(\xi,\eta\right)=\sum_{l=0}^{\infty}\frac{2l+1}{A_l^2}P_l\left(\xi\cdot\eta\right), \tag{3.38}$$

where P_l are Legendre polynomials. The summability of the series (3.38) depends on the set number, A, which must satisfies

$$\sum_{l=0}^{\infty}(2l+1)\frac{1}{A_l^2}<\infty, \tag{3.39}$$

such that the series of the reproducing kernel can be summed. Any function, $s\left(\xi\right)$, in the Hilbert space, $H\left(\left\{A_l\right\},\Omega\right)$, having the form

$$s\left(\xi\right)=\sum_{i=1}^{N}c_iK_A(\xi,\eta_i), \tag{3.40}$$

is defined to be a spherical spline. c_i are coefficients and the points, η_i, are defined on the unit sphere.

In order to implement these spherical splines, Schreiner (1997) provided truly locally supported kernel functions from a piecewise polynomial function. Consider the function defined on the interval, $-1\le t\le 1$:

$$B_h^{(k)}(t)=\left\{\begin{matrix}0,-1\le t\le h\\ \left(\frac{t-h}{1-h}\right)^k,h<t\le 1\end{matrix}\right\}=\sum_{l=0}^{\infty}(2l+1)\beta_lP_l(t), \tag{3.41}$$

where $k\ge 1$; and then define the kernel function as the convolution of $B_h^{(k)}$ with itself:

$$K_A\left(\xi,\eta_i\right)=B_h^{(k)}(\xi\cdot\eta_i)*B_h^{(k)}(\xi\cdot\eta_i)=\sum_{l=0}^{\infty}(2l+1)\beta_l^2P_l\left(\xi\cdot\eta_i\right), \tag{3.42}$$

Comparing (3.42) to (3.38), we have $\beta_l=\frac{1}{A_l}$. Schreiner (1997) derived a recursion formula for A_l, which is for $k\ge 0$ and $l\ge 1$

$$\begin{aligned}\frac{1}{A_0}&=2\pi\frac{1-h}{k+1}\\ \frac{1}{A_1}&=\frac{k+1+h}{k+2}\frac{1}{A_0}\\ \frac{1}{A_{l+1}}&=\frac{k+1-l}{l+k+2}\frac{1}{A_{l-1}}+\frac{2l+1}{l+k+2}\frac{1}{A_l}\end{aligned} \tag{3.43}$$

where h is a parameter that defines the local support for K_A:

$$h=\sqrt{\frac{\cos\psi+1}{2}}, \tag{3.44}$$

where ψ is the spherical radius of the support region.

3.4.2 Interpolation of gravity and gradients

The basic idea is to determine gradients from gravity anomaly data using a spline function representation of the gravity anomaly data. The coefficients of the spline function are determined as follows. Suppose P, Q_i are two points on the spheres with radii of r_P, r_{Q_i} respectively. Consider the kernel function,

$$K_A(P,Q_i) = \sum_{l=0}^{\infty} \frac{2l+1}{A_l^2} \left(\frac{R^2}{r_P r_{Q_i}} \right)^{l+1} P_l\left(\cos\psi_{PQ_i}\right), \tag{3.45}$$

the disturbing potential can be expressed by using these kernel functions as splines for a set of points Q_i, $i = 1,\ldots,N$, located on the sphere with the radius of R,

$$T(P) = \sum_{i=1}^{N} c_i K_A\left(P,Q_i\right). \tag{3.46}$$

Using $\Delta g = -\frac{\partial T}{\partial r} - \frac{2}{R}T$, the gravity anomaly can be obtained according to (3.46),

$$\Delta g\left(Q_j\right) = \sum_{i=1}^{N} c_i K_A^{\Delta g}\left(Q_j,Q_i\right). \tag{3.47}$$

where we have the kernel function for the gravity anomaly on the sphere of radius, R:

$$K_A^{\Delta g}(Q_j,Q_i) = \sum_{l=2}^{\infty} \frac{l-1}{R}\frac{2l+1}{A_l^2} P_l\left(\cos\psi_{Q_jQ_i}\right),\ i = 1,\ldots,N \tag{3.48}$$

Practically for given observed gravity anomaly data, one uses (3.48) to solve the coefficients, c_i.

Letting $e_i, i = 1,\ldots,N$, be the error of the observation data on points, Q_i, we design the model

$$\begin{pmatrix} \Delta g(Q_1) \\ \vdots \\ \Delta g(Q_N) \end{pmatrix} = \begin{pmatrix} K_A^{\Delta g}(Q_1,Q_1) & \cdots & K_A^{\Delta g}(Q_1,Q_N) \\ \vdots & \ddots & \vdots \\ K_A^{\Delta g}(Q_N,Q_1) & \cdots & K_A^{\Delta g}(Q_N,Q_N) \end{pmatrix} \begin{pmatrix} c_1 \\ \vdots \\ c_N \end{pmatrix}. \tag{3.49}$$

The elements in the matrix, $K_A^{\Delta g}$, depend on the spherical distance between points Q_i and Q_j. If one defines a range, ψ_1, e.g. 5 arcmin, in (3.44) such that the spline kernel function defined by A_l is zero outside of this range. One example is given in Figure 3.12 where the spline kernel function is determined by the parameters: $\psi_1 = 5'$ and $k = 2$, and its value is scaled by the value of kernel function at $\psi = 0$. When $\psi > 5'$, the value of the kernel function is zero. If Q_i, $i = 1,\ldots,N$ are ordered eastward in a row and northward in a column, for those point pairs, $\left(Q_{i1},Q_{i2}\right)$, $1 \le i1 \le N, 1 \le i2 \le N$, when their distances are more than 5 arcmin, the kernel, $K_A^{\Delta g}\left(Q_{i1},Q_{i2}\right)$ is zero. This definition results in a sparse

matrix, $K_A^{\Delta g}$, which can facilitate the computation of the matrix inverse. The coefficients, c_i are obtained as follows:

$$\begin{pmatrix} c_1 \\ \vdots \\ c_N \end{pmatrix} = \begin{pmatrix} K_A^{\Delta g}(Q_1,Q_1) & \cdots & K_A^{\Delta g}(Q_1,Q_N) \\ \vdots & \ddots & \vdots \\ K_A^{\Delta g}(Q_N,Q_1) & \cdots & K_A^{\Delta g}(Q_N,Q_N) \end{pmatrix}^{-1} \begin{pmatrix} \Delta g(Q_1) \\ \vdots \\ \Delta g(Q_N) \end{pmatrix}. \tag{3.50}$$

We obtain the spherical spline representation for the disturbing potential from the determined coefficients, c_i. Finally the gradient disturbances can be computed by taking the second derivatives of the disturbing potential.

$$\delta\Gamma_{jk}(P) = \sum_{i=1}^{N} c_i \frac{\partial^2 K_A(P,Q_i)}{\partial x_j \partial x_k}, \tag{3.51}$$

where $\frac{\partial^2 K_A(P,Q_i)}{\partial x_j \partial x_k}$ are the second derivatives of the kernel function and will be discussed in the following section. The spherical splines, applied to the gravity anomaly data on the sphere allow the upward continuation of the gradient disturbances.

3.4.3 Derivatives of Kernel Function

The kernel function between point $P(r,\theta,\lambda)$ and $Q(R,\theta',\lambda')$ can be expressed as follows:

$$K_A(r,\theta,\lambda;R,\theta',\lambda') = \sum_{l=0}^{\infty} \frac{2l+1}{A_l^2}\left(\frac{R}{r}\right)^{l+1} P_l(\cos\psi). \tag{3.52}$$

Then we can derive the second derivatives of the kernel function according to (3.6). The derivatives of K_A with respect to the spherical coordinates are given by

$$\frac{\partial K_A}{\partial r} = \sum_{l=0}^{\infty} \frac{-l-1}{R}\frac{2l+1}{A_l^2}\left(\frac{R}{r}\right)^{l+2} P_l(\cos\psi),$$

$$\frac{\partial K_A}{\partial \theta} = \sum_{l=0}^{\infty} \frac{2l+1}{A_l^2}\left(\frac{R}{r}\right)^{l+1} \frac{\partial P_l(\cos\psi)}{\partial \theta},$$

$$\frac{\partial^2 K_A}{\partial \theta^2} = \sum_{l=0}^{\infty} \frac{2l+1}{A_l^2}\left(\frac{R}{r}\right)^{l+1} \frac{\partial^2 P_l(\cos\psi)}{\partial \theta^2},$$

$$\frac{\partial K_A}{\partial \lambda} = \sum_{l=0}^{\infty} \frac{2l+1}{A_l^2}\left(\frac{R}{r}\right)^{l+1} \frac{\partial P_l(\cos\psi)}{\partial \lambda},$$

$$\frac{\partial^2 K_A}{\partial \lambda^2} = \sum_{l=0}^{\infty} \frac{2l+1}{A_l^2}\left(\frac{R}{r}\right)^{l+1} \frac{\partial^2 P_l(\cos\psi)}{\partial \lambda^2},$$

$$\frac{\partial^2 K_A}{\partial\theta\partial r}=\sum_{l=0}^{\infty}\frac{-l-1}{R}\frac{2l+1}{A_l^2}\left(\frac{R}{r}\right)^{l+2}\frac{\partial P_l(\cos\psi)}{\partial\theta},$$

$$\frac{\partial^2 K_A}{\partial\lambda\partial r}=\sum_{l=0}^{\infty}\frac{-l-1}{R}\frac{2l+1}{A_l^2}\left(\frac{R}{r}\right)^{l+2}\frac{\partial P_l(\cos\psi)}{\partial\lambda},$$

$$\frac{\partial^2 K_A}{\partial r^2}=\sum_{l=0}^{\infty}\frac{(l+1)(l+2)}{R^2}\frac{2l+1}{A_l^2}\left(\frac{R}{r}\right)^{l+3}P_l(\cos\psi), \tag{3.53}$$

where the derivative of the Legendre polynomial are

$$\frac{\partial P_l(\cos\psi)}{\partial\theta}=\frac{dP_l(\cos\psi)}{d\cos\psi}(-\sin\theta\cos\theta'+\cos\theta\sin\theta'\cos(\lambda-\lambda')), \tag{3.54}$$

$$\frac{\partial^2 P_l(\cos\psi)}{\partial\theta^2}=\frac{d^2P_l(\cos\psi)}{d(\cos\psi)^2}(-\sin\theta\cos\theta'+\cos\theta\sin\theta'\cos(\lambda-\lambda'))^2-\frac{dP_l(\cos\psi)}{d\cos\psi}\cos\psi, \tag{3.55}$$

$$\frac{\partial P_l(\cos\psi)}{\partial\lambda}=\frac{dP_l(\cos\psi)}{d\cos\psi}(-\sin\theta\sin\theta'\sin(\lambda-\lambda')), \tag{3.56}$$

$$\frac{\partial^2 P_l(\cos\psi)}{\partial\lambda^2}=\frac{d^2P_l(\cos\psi)}{d(\cos\psi)^2}(\sin\theta\sin\theta'\sin(\lambda-\lambda'))^2-\frac{dP_l(\cos\psi)}{d\cos\psi}\sin\theta\sin\theta'\cos(\lambda-\lambda'), \tag{3.57}$$

$$\frac{\partial^2 P_l(\cos\psi)}{\partial\theta\partial\lambda}=\frac{d^2P_l(\cos\psi)}{d(\cos\psi)^2}(-\sin\theta\cos\theta'+\cos\theta\sin\theta'\cos(\lambda-\lambda'))(-\sin\theta\sin\theta'\sin(\lambda-\lambda')$$
$$-\frac{dP_l(\cos\psi)}{d\cos\psi}(\cos\theta\sin\theta'\sin(\lambda-\lambda')) \tag{3.58}$$

A recursion formula for the Legendre polynomials (Heiskanen and Moritz, 1967, eq.(1-59)) can be used to compute the derivatives. We have

$$P_l(\cos\psi)=-\frac{l-1}{l}P_{l-2}(\cos\psi)+\frac{2l-1}{l}\cos\psi P_{l-1}(\cos\psi). \tag{3.59}$$

Now we take derivative on both sides with respect to $\cos\psi$ and get

$$\frac{dP_l(\cos\psi)}{d(\cos\psi)}=-\frac{l-1}{l}\frac{dP_{l-2}(\cos\psi)}{d(\cos\psi)}+\frac{2l-1}{l}\cos\psi\frac{dP_{l-1}(\cos\psi)}{d(\cos\psi)}+\frac{2l-1}{l}P_{l-1}(\cos\psi), \tag{3.60}$$

$$\frac{d^2P_l(\cos\psi)}{d(\cos\psi)^2}=-\frac{l-1}{l}\frac{d^2P_{l-2}(\cos\psi)}{d(\cos\psi)^2}+\frac{2l-1}{l}\cos\psi\frac{d^2P_{l-1}(\cos\psi)}{d(\cos\psi)^2}+\frac{4l-2}{l}\frac{dP_{l-1}(\cos\psi)}{d(\cos\psi)} \tag{3.61}$$

The first and second-order derivatives of the Legendre polynomials with respect to $\cos\psi$ can be evaluated recursively using (3.59)-(3.61). That is, we use (3.59) to compute Legendre polynomial values over the degrees and the first-order derivatives over the degree are recursively solved in (3.60) from the initial two values for the first–order derivative and Legendre polynomial values. In a similar way, the second-order derivatives can be recursively solved in (3.61).

3.5 Least–squares collocation

Assuming the disturbing potential, T, is a stochastic process on the sphere of radius R_b, its covariance function (Tscherning, 1976) in any two points in space or outside this sphere can be expressed as

$$Cov(T_P, T_Q) = \sum_{l=2}^{\infty} \sigma_l \left(\frac{R_b^2}{r_P r_Q} \right)^{l+1} P_l(\cos\psi), \tag{3.62}$$

where σ_l are degree variances of the disturbing potential, R_b is the radius of the Bjerhammar sphere, $P_l(\cos\psi)$ are the Legendre polynomials, r_P and r_Q are the distances of P and Q from the origin, and ψ is the spherical distance between P and Q. From (3.62), we can obtain the auto-covariance of the gravity anomaly using the usual propagation of covariances. Let the covariance function be expressed as

$$Cov(\Delta g_P, \Delta g_Q) = \sum_{l=l_{\min}}^{l_{\max}} c_l \left(\frac{R_b^2}{r_P r_Q} \right)^{l+2} P_l(\cos\psi), \tag{3.63}$$

with $c_l = (l-1)^2 \sigma_l / R_b^2$. $l_{\min}$ and $l_{\max}$ are practical limits in the harmonic degrees, which are determined by the resolution of discrete data used in the estimation. The cross-covariance between the disturbing potential and gravity anomaly is given as follows:

$$Cov(T_P, \Delta g_Q) = r_P \sum_{l=l_{\min}}^{l_{\max}} \frac{c_l}{l-1} \left(\frac{R_b^2}{r_P r_Q} \right)^{l+2} P_l(\cos\psi). \tag{3.64}$$

The covariance function between the gradient disturbances and the gravity anomaly is then

$$Cov(\delta\Gamma_{jk_P}, \Delta g_Q) = \frac{\partial^2}{\partial x_j \partial x_k} Cov(T_P, \Delta g_Q), \tag{3.65}$$

Now using (3.6), and (3.57) - (3.61), we obtain

$$Cov(\delta\Gamma_{11_P}, \Delta g_Q) = \frac{1}{r_P} \sum_{l=l_{\min}}^{l_{\max}} \frac{c_l}{l-1} \left(\frac{R_b^2}{r_P r_Q} \right)^{n+2} \begin{bmatrix} -(l+1)P_l(\cos\psi) - P_{l1}(\cos\psi)\cot\psi \\ +P_{l2}(\cos\psi)\sin^2\alpha \end{bmatrix},$$

$$Cov(\delta\Gamma_{12_P}, \Delta g_Q) = \frac{1}{r_P} \sum_{l=l_{\min}}^{l_{\max}} \frac{c_l}{l-1} \left(\frac{R_b^2}{r_P r_Q} \right)^{l+2} P_{l2}(\cos\psi)\cos\alpha\sin\alpha,$$

$$Cov(\delta\Gamma_{13_P}, \Delta g_Q) = -\frac{1}{r_P} \sum_{l=l_{\min}}^{l_{\max}} \frac{l+2}{l-1} c_l \left(\frac{R_b^2}{r_P r_Q} \right)^{l+2} P_{l1}(\cos\psi)\sin\alpha,$$

$$Cov(\delta\Gamma_{22_P}, \Delta g_Q) = \frac{1}{r_P} \sum_{l=l_{\min}}^{l_{\max}} \frac{c_l}{l-1} \left(\frac{R_b^2}{r_P r_Q} \right)^{l+2} \begin{bmatrix} P_{l2}(\cos\psi)\cos^2\alpha - P_{l1}(\cos\psi)\cot\psi \\ -(l+1)P_l(\cos\psi) \end{bmatrix},$$

$$Cov(\delta\Gamma_{23_P}, \Delta g_Q) = -\frac{1}{r_P}\sum_{l=l_{\min}}^{l_{\max}} \frac{(l+2)c_l}{l-1}\left(\frac{R_b^2}{r_P r_Q}\right)^{l+2} P_{l1}(\cos\psi)\cos\alpha\,,$$

$$Cov(\delta\Gamma_{33_P}, \Delta g_Q) = \frac{1}{r_P}\sum_{l=l_{\min}}^{l_{\max}} \frac{(l+1)(l+2)}{l-1}c_l\left(\frac{R_b^2}{r_P r_Q}\right)^{l+2} P_l(\cos\psi)\,. \tag{3.66}$$

One could use one of several existing models for the degree variances (Jekeli, 2003), or derive empirical values from the actual gravity data with the help of the Fourier transform of the auto-covariance function. Here, we use an analytical model (Tscherning et al., 1992) for the degree variance,

$$c_l = \frac{A_0(l-1)}{(l-2)(l+4)}\left(\frac{R_b^2}{R^2}\right)^{l+2}, \tag{3.67}$$

where A_0 is a scale factor, and R is the mean earth radius. Suppose P_i, $i = 1,\ldots,M1$ are points where the gradient disturbances are to be determined. The gravity anomaly data are given on the points, Q_i, $i = 1,\ldots,N$. Finally, the gradient disturbances are estimated using least-squares collocation according to

$$\underset{M1\times 1}{\delta\Gamma_{jk}} = \underset{M1\times N}{Cov(\delta\Gamma_{jk}, \Delta g)}\left(\underset{N\times N}{Cov(\Delta g, \Delta g)} + \underset{N\times N}{D}\right)^{-1}\underset{N\times 1}{\Delta g}\,. \tag{3.68}$$

In (3.68), $M1, N$ are dimensions of matrices, and $Cov(\delta\Gamma_{jk,}\Delta g)$ and $Cov(\Delta g, \Delta g)$ can be evaluated with the modeled degree variance, and D is the diagonal matrix of variances of the observation noise.

Instead of using a spherical covariance model like (3.63), a planar covariance model can be used to estimate the gradient disturbances. Forsberg (1987) suggested some planar logarithmic covariance functions and gave their relationship to spherical degree-variance models. The reciprocal distance model (Moritz, 1978; Jekeli, 2003) can also be used as long as it incorporates the upward continuation. The selection between spherical and planar covariance model ultimately depends on local applications as well as their implementations. The planar model usually has simpler formulas, but the spherical model can also be evaluated rapidly using a tabular method and is able to account better for the low-frequency part of the signal (Forsberg, 1987).

3.6 Analyzing gradient model using simulated fields

3.6.1 Simulated field

We developed Stokes' integral, spherical splines, and least-squares collocation to determine gradient disturbances from gravity anomaly data. Here we test these methods using simulated gravity data, which was generated using a power spectral density (PSD) model of the gravity disturbance. This model was designed using moderately varying gravity anomaly data in the Montana/Wyoming area of U.S. Figure 3.2 shows the PSD of the gravity disturbance in the specified (below) spectral band. The blue solid line is the PSD model used to generate the simulated field and the red dot line is the PSD corresponding to the degree variance model used in the least-squares collocation

(described in (3.81)). The spectral band in Figure 3.2 corresponds to, $l_{\min} = 180$ and $l_{\max} = 10800$, the minimum and maximum frequencies that can be recovered from 1'×1' gravity anomaly data in a $1^\circ \times 1^\circ$ area. Considering that the area is small, we use the planar approximation instead of the spherical approximation to derive the synthetic data.

Let Δx_1 and Δx_2 be the grid intervals, 1.5 km and 1.8 km in east and north directions respectively for 1 arcmin gravity data. J_1 and J_2 (e.g. $J_1 = J_2 = 60$) are the grid numbers in each direction, (k_1, k_2), $k_1 = 0, \ldots, J_1 - 1, k_2 = 0, \ldots, J_2 - 1$ are the spatial coordinates and f_{k_1,k_2} are the frequencies corresponding to the spatial coordinates, given by

$$f_{k_1,k_2} = \sqrt{f_{1_{k_1}}^2 + f_{2_{k_2}}^2},$$

$$f_{1_{k_1}} = \frac{k_1}{J_1 \Delta x_1}, f_{2_{k_1}} = \frac{k_2}{J_2 \Delta x_2}, \text{ for } k_1 = 0, \ldots, \frac{J_1}{2} - 1, k_2 = 0, \ldots, \frac{J_2}{2} - 1,$$

$$f_{1_{k_1}} = \frac{k_1 - J_1}{J_1 \Delta x_1}, f_{2_{k_1}} = \frac{k_2 - J_2}{J_2 \Delta x_2}, \text{ for } k_1 = \frac{J_1}{2}, \ldots, J_1 - 1, k_2 = \frac{J_2}{2}, \ldots, J_2 - 1. \quad (3.69)$$

We define A_{k_1,k_2} as the magnitude of the (k_1, k_2) spatial component of the disturbing potential. A_{k_1,k_2} is constructed from the square root of the PSD value, $\Phi\left(f_{k_1,k_2}\right)$, and a randomization per frequency using uniformly distributed variables, v_{k_1,k_2}:

$$A_{k_1,k_2} = v_{k_1,k_2} \frac{\sqrt{J_1 \Delta x_1 J_2 \Delta x_2}}{2\pi f_{k_1,k_2}} \sqrt{\Phi_{\delta g}\left(f_{k_1,k_2}\right)}, f_{k_1,k_2} \neq 0. \quad (3.70)$$

v_{k_1,k_2} is a uniformly distributed random variable:

$$v_{k_1,k_2} \sim U\left[-\sqrt{3}, \sqrt{3}\right],$$

so that the standard deviation of v is a unity. We define the spectrum of the disturbing potential at the altitude, x_3, as:

$$\Im(T)_{k_1,k_2} = A_{k_1,k_2} e^{i\varphi_{k_1,k_2}} e^{-2\pi x_3}, \quad (3.71)$$

where the phase, φ_{k_1,k_2}, is also a uniformly distributed random variable:

$$\varphi_{k_1,k_2} \sim U[0, 2\pi].$$

The spectrum of the gravity disturbance at $x_3 = 0$ is

$$\Im(\delta g)_{k_1,k_2} = -2\pi f_{k_1,k_2} A_{k_1,k_2} e^{i\varphi_{k_1,k_2}}. \quad (3.72)$$

The spectra of the gradient disturbances are synthesized in a way similar to (2.43):

$$\Im(\delta\Gamma_{jk}) = \mu_{jk} \Im(T). \quad (3.73)$$

Thus, the synthetic gravity disturbance, disturbing potential and the gradient disturbances are obtained by an inverse discrete Fourier transform of their Fourier spectra according to (2.54). Using $\Delta g = \delta g - \frac{2}{R} T$, we also derived the synthetic gravity anomaly simultaneously. In this area, the absolute value of the disturbing potential is less than

$10\,m^2/s^2$, so the difference between the gravity anomaly and the gravity disturbance is less than 0.15 mGal. Figure 3.3 shows the synthetic gravity anomaly in an $1^\circ \times 1^\circ$ area with resolution of 1 arc min; totally, there are $60 \times 60 = 3600$ data points. The rms of Δg and $\delta\Gamma_{33}$ (on the geoid) are 7.9 mGal and 21.8 E, respectively. The central black line in Figure 3.3 is the test profile. The upward continuation of the modeled gradient disturbance along this profile was performed at different altitudes of 100 m through 3000 m. The spacing of the computation points along the test profile is 1 arc min. The synthetic gradient disturbances were considered as true in the following comparisons of the modeled gradient disturbances.

3.6.2 Modeled Gradient disturbances

The gradient disturbances were derived on the basis of all 3600 gravity anomaly data shown in Figure 3.3, $\Delta g_{n,m}$, $n,m = 1,\ldots 60$. To compare the spherical approximation to the planar approximation, we use (3.13) and (3.22) respectively to compute the gradient disturbances. The integrals in (3.13) and (3.22) are evaluated by summing point values on the grid points (as opposed to the method of (3.25), where the kernel is integrated analytically over a grid compartment). For example, the gradient disturbance, $\delta\Gamma_{11}$ at the points, $\left(x_{1,h,i}, x_{2,h,i}, x_3\right)$, $1 \le h \le 60, 1 \le i \le 60,$ are computed as follows:

$$\left(\delta\Gamma_{11}\right)_{h,i} = \frac{R}{4\pi}\sum_{n=1}^{60}\sum_{m=1}^{60}\Delta g_{n,m}\left(C_{1,r}S_r + C_{1,\psi^2}S_{\psi^2} + C_{1,\psi}S_{\psi}\right)_{n,m;h,i}\Delta\sigma, \tag{3.74}$$

$$\left(\delta\Gamma_{11}\right)_{h,i} = \frac{\Delta x_1 \Delta x_2}{2\pi}\sum_{n=1}^{60}\sum_{m=1}^{60}\Delta g_{n,m}\left(\frac{3\left(x_{1,j,k} - x_{1,n,m}\right)^2 - l_{n,m;h,i}^2}{l_{n,m;h,i}^5}\right), \tag{3.75}$$

where $\Delta\sigma = \sin\theta\Delta\theta\Delta\lambda$, θ is the co-latitude, $53^\circ.5 \le \theta \le 54^\circ.5$. $\Delta\theta$ and $\Delta\lambda$ are the sampling intervals along latitude and longitude, respectively, under the spherical approximation. Δx_1 and Δx_2 are the grid interval in east and north directions under the planar approximation.

For the sake of convenience, we denote $\Delta\delta\Gamma_{jk}^{ap}$ as the difference between the modeled gradient disturbances under the spherical approximation and those under the planar approximation. Table 3.1 gives the rms of $\Delta\delta\Gamma_{jk}^{ap}$ (considering the edge effect, we neglect 10 estimates at each side of profile) at different altitudes. At 100 m, $\Delta\delta\Gamma_{12}^{ap}$, $\Delta\delta\Gamma_{13}^{ap}$, and $\Delta\delta\Gamma_{23}^{ap}$ have the largest rms values, 0.0088 E, 0.0201 E and 0.0296 E respectively. With an increase in altitude, these rms values decrease due to the attenuation of upward continuation. At 100 m, the rms values of $\Delta\delta\Gamma_{11}^{ap}$, $\Delta\delta\Gamma_{22}^{ap}$, and $\Delta\delta\Gamma_{33}^{ap}$ are 0.053 E, 0.0067 E and 0.0004 E, respectively. These rms values increase with an increase in altitude and reach the highest at 1000m. After 1000m, they begin to decrease with an increase in altitude. Generally, for the gradient disturbance computation based on $1^\circ \times 1^\circ$ gravity anomaly data with 1 arcmin resolution, the rms values of the differences between spherical and planar approximation are less than 0.03 E for all gradient components. In

order to expand this comparison with respect to the extent of integration, we also generated a $2^{\circ}\times 2^{\circ}$ synthetic gravity anomaly data shown in Figure 3.4 with the resolution of 1 arc min. The values of $l_{\min}$ and $l_{\max}$ used in the synthesis are 180 and 10800. The method is same as for the $1^{\circ}\times 1^{\circ}$ synthetic gravity anomaly and only the grid numbers are extended to 120. In Figure 3.4, the rms of the gravity anomaly is 17.2 mGal and the minimum and maximum are 39.1 and -58.9 mGal, respectively. Table 3.2 lists the rms of the differences (considering the edge effect, we neglect 20 estimates at each side of profile) between the spherical and the planar approximation. The rms of $\Delta\delta\Gamma_{jj}^{ap}$ (in-line gradient disturbances) increases with altitude increasing from 100 m through 1500 m and becomes stable after 1500m. The rms of $\Delta\delta\Gamma_{jk}^{ap}$ (off-diagonal gradient disturbances) generally decreases with an increase in altitude, except for $\Delta\delta\Gamma_{23}^{ap}$. The rms values of the differences are less than 0.08 E for all gradient disturbances computed from the gravity anomaly data in the $2^{\circ}\times 2^{\circ}$ area. They are below the best accuracy of an airborne gradiometer (e.g. 1 E), so the planar approximation is adequate to determine gradients using Stokes' integral.

Now (3.25) is also applied to model the gradients by integrating the kernel over the grid interval instead of using just the grid point value. Based on two sets of gravity anomaly data shown in Figures 3.3 and 3.4, we compute the gradient disturbances at the test profiles at different altitudes from 100 m through 3000 m. We compared these results to true gradient disturbances and denote their differences as $\Delta\delta\Gamma_{jk}^{st}$. We also compared the results computed by (3.75) (Other components are evaluated in a similar way that the integrand is evaluated on the grid point) to true gradient disturbances and denote their differences as $\Delta\delta\Gamma_{jk}^{st1}$. These results are presented in Figures 3.5-3.8. Table 3.3 and 3.4 list the parts of rms values. Figure 3.5 shows the rms of $\Delta\delta\Gamma_{11}^{st1}$ first decreases with altitude increasing from 100 m to 300 m, and then increases when the altitude increases from 300 m to 700m, and finally decreases after 700 m. The rms for all other $\Delta\delta\Gamma_{jk}^{st1}$ is the biggest at 100 m. After 100m, the rms of $\Delta\delta\Gamma_{12}^{st1}$, $\Delta\delta\Gamma_{13}^{st1}$ and $\Delta\delta\Gamma_{23}^{st1}$ decreases with an increase in altitude. Figure 3.6 shows that $\Delta\delta\Gamma_{jj}^{st}$ (the inline gradients) have smaller rms values than $\Delta\delta\Gamma_{jk}^{st}$ (the off-diagonal gradients) at the lower altitudes. At 100 m, the rms values of $\Delta\delta\Gamma_{12}^{st}$, $\Delta\delta\Gamma_{13}^{st}$ and $\Delta\delta\Gamma_{23}^{st}$ are 3.58 E, 10.63 E and 11.60 E, respectively, but the rms values of $\Delta\delta\Gamma_{11}^{st}$, $\Delta\delta\Gamma_{22}^{st}$ and $\Delta\delta\Gamma_{33}^{st}$ are 1.03 E, 1.01 E and 1.57 E. The rms values of the differences decrease with an increase in altitude. For example, at 1000 m, the rms values of $\Delta\delta\Gamma_{12}^{st}$, $\Delta\delta\Gamma_{13}^{st}$ and $\Delta\delta\Gamma_{23}^{st}$ are 0.54 E, 0.92 E and 1.27 E, respectively, and the rms values of $\Delta\delta\Gamma_{11}^{st}$, $\Delta\delta\Gamma_{22}^{st}$ and $\Delta\delta\Gamma_{33}^{st}$ are 0.27 E, 0.19 E and 0.31 E. Figure 3.7 presents results similar to Figure 3.5 and Figure 3.8 presents the similar results to Figure 3.6 but for larger (2°×2°) data extent. From Table 3.3 and Table 3.4 we can find that the rms of $\Delta\delta\Gamma_{jk}^{st}$ is less than that of $\Delta\delta\Gamma_{jk}^{st1}$ at the same altitude. It demonstrated that the modeled gradient disturbances evaluated from (3.25) are more accurate than those evaluated from (3.75) when compared to the true gradient disturbances. The Stokes'

integral yields much worse results at the lower altitude (e.g. 100 m, which is much less than the average grid interval, 1.5 km of the gravity anomaly data). This problem is caused by (3.27) in evaluating the integral of the kernel. According to (3.27), when $x_3 \to 0$, we have $K^{13}, K^{23} \to 0$. So the estimation of $\delta\Gamma_{13}^{st}$ and $\delta\Gamma_{23}^{st}$ tends to be smaller than true gradients at the lower altitude due to the singularity and the resolution of data. Thus the computation of off-diagonal gradient disturbances at the lower altitude needs to be implemented by other techniques, such as the least-squares collocation (in a later example, LSC is more accurate than Stokes's integral at the altitude of 600 m).

According to the two sets of results, Stokes' integral can be used to compute the gradient disturbances at altitudes which are larger than the resolution of the gravity anomaly data. To test this property of Stokes' integral in computing the gradient disturbances, we generate a synthetic $6" \times 6"$ gravity anomaly data shown in Figure 3.9 using the same PSD as the previous 2 sets of data and compute the gradient disturbances with these gravity data. The statistics of gravity anomalies is: min: -32.8 mGal; max: 38.8 mGal, rms: 14.1 mGal. All gradient disturbances are computed on the points along the profile across the center of the area with the interval of 180m at different altitudes and compared to the synthetic data generated by (3.73) using FFT. The rms values of the differences (considering the edge effect, we neglect 100 estimates at each side of the profile) between modeled gradient disturbances and "true" quantities are plotted in Figure 3.10. At 100 m, the rms values are the largest for all gradient disturbance components. The rms of $\Delta\delta\Gamma_{13}^{st}$ and $\Delta\delta\Gamma_{23}^{st}$ decrease very quickly when the altitude increases from 100 m to 700 m and gradually increase with an increase in altitude. The rms of $\Delta\delta\Gamma_{12}^{st}$ decreases when the altitude increases from 100 m to 300 m, and keeps constant with an increase in altitude. The rms of $\Delta\delta\Gamma_{11}^{st}$ and $\Delta\delta\Gamma_{22}^{st}$ tend to be constant with the increase of the altitude. The rms of $\Delta\delta\Gamma_{33}^{st}$ decreases with the altitude increasing from 100 m to 600 m and keeps stable after 600 m. $\Delta\delta\Gamma_{jk}^{st}$ along the profile at 200 m is presented in Figure 3.11, where $\Delta\delta\Gamma_{13}^{st}$ and $\Delta\delta\Gamma_{23}^{st}$ are around zero, but $\Delta\delta\Gamma_{12}^{st}$ has a linear trend along the profile. The statistics of $\Delta\delta\Gamma_{jk}^{st}$ is given in Table 3.5, where their standard deviations are between 0.3 E and 0.6 E. The mean values are around zero for the off-diagonal gradient disturbances and they are 1.0 E, -0.9 E and -0.1 E for in-line gradient disturbances. Thus, the gradient modeling based on gravity anomaly data with $6" \times 6"$ resolution accurate to better than 1 E above an altitude of 200 m based on this simulation.

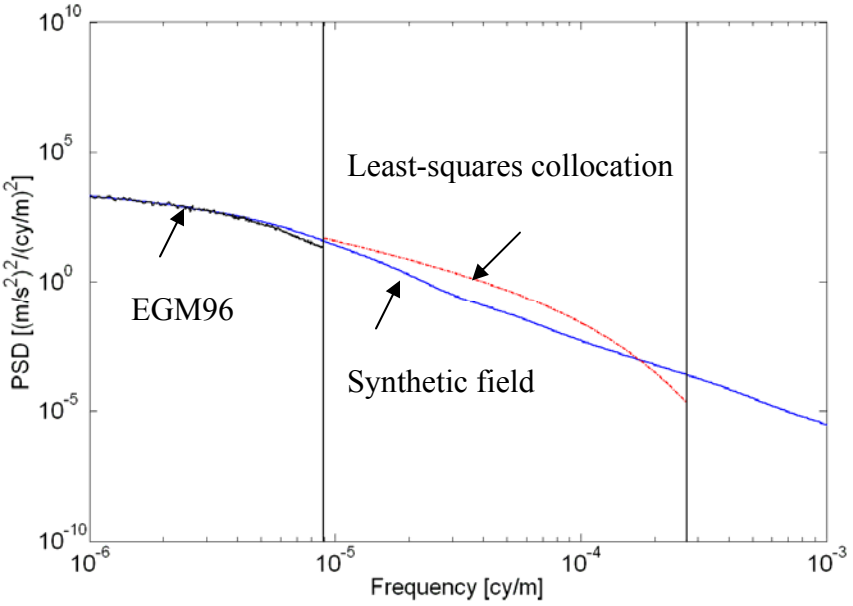

Figure 3.2: Power spectral densities of the gravity disturbance used to generate a synthetic field and for least-squares collocation (transformed from the degree variance model).

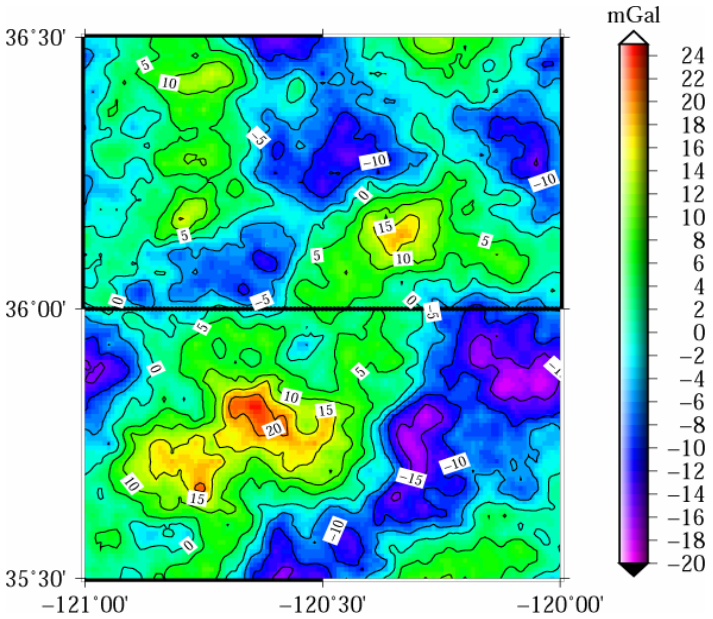

Figure 3.3: $1^\circ \times 1^\circ$ gravity anomaly field generated by randomization of the psd shown in Figure 3.2 (the black line is the central profile used for tests).

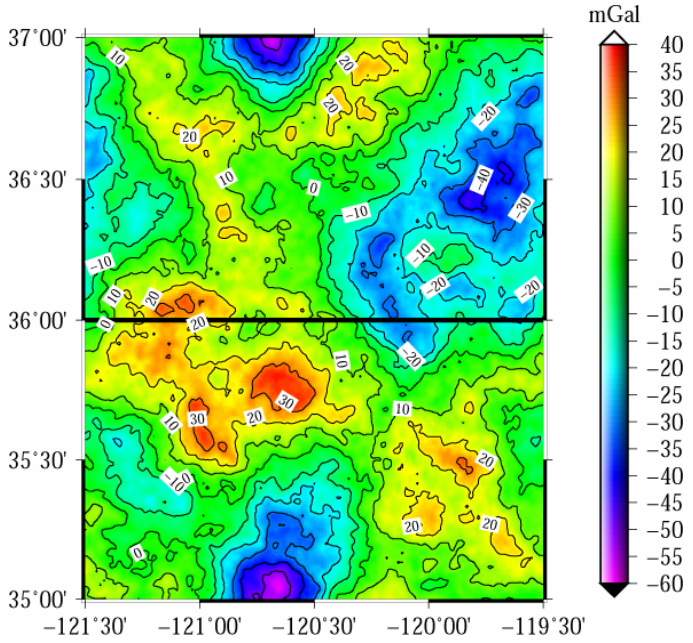

Figure 3.4: $2^{\circ} \times 2^{\circ}$ gravity anomaly field gravity anomaly field generated by randomization of the psd shown in Figure 3.8 (the black line is central profile used for tests).

Table 3.1: RMS of $\Delta\delta\Gamma_{jk}^{ap}$ (gravity anomaly extent: $1^{\circ} \times 1^{\circ}$, unit: E).

Altitude (m)	$\Delta\delta\Gamma_{11}^{ap}$	$\Delta\delta\Gamma_{12}^{ap}$	$\Delta\delta\Gamma_{13}^{ap}$	$\Delta\delta\Gamma_{22}^{ap}$	$\Delta\delta\Gamma_{23}^{ap}$	$\Delta\delta\Gamma_{33}^{ap}$
100	0.0053	0.0088	0.0201	0.0067	0.0296	0.0040
500	0.0089	0.0077	0.0189	0.0077	0.0278	0.0128
1000	0.0099	0.0065	0.0170	0.0087	0.0244	0.0162
1500	0.0089	0.0055	0.0153	0.0083	0.0213	0.0154
2000	0.0079	0.0047	0.0140	0.0076	0.0188	0.014
2500	0.0070	0.0041	0.0128	0.0069	0.0167	0.0127
3000	0.0063	0.0036	0.0117	0.0064	0.0148	0.0116

Table 3.2: RMS of $\Delta\delta\Gamma_{jk}^{ap}$ (gravity anomaly extent: $2^{\circ}\times 2^{\circ}$, unit: E).

Altitude (m)	$\Delta\delta\Gamma_{11}^{ap}$	$\Delta\delta\Gamma_{12}^{ap}$	$\Delta\delta\Gamma_{13}^{ap}$	$\Delta\delta\Gamma_{22}^{ap}$	$\Delta\delta\Gamma_{23}^{ap}$	$\Delta\delta\Gamma_{33}^{ap}$
100	0.016	0.0258	0.0591	0.0173	0.0548	0.0141
500	0.0386	0.025	0.0574	0.0265	0.0576	0.0569
1000	0.0474	0.0238	0.0542	0.0356	0.0584	0.0771
1500	0.0468	0.0227	0.0513	0.0379	0.0571	0.0791
2000	0.0453	0.0217	0.0487	0.0377	0.0551	0.0775
2500	0.0438	0.0208	0.0464	0.037	0.053	0.0752
3000	0.0422	0.0199	0.0443	0.0362	0.051	0.0729

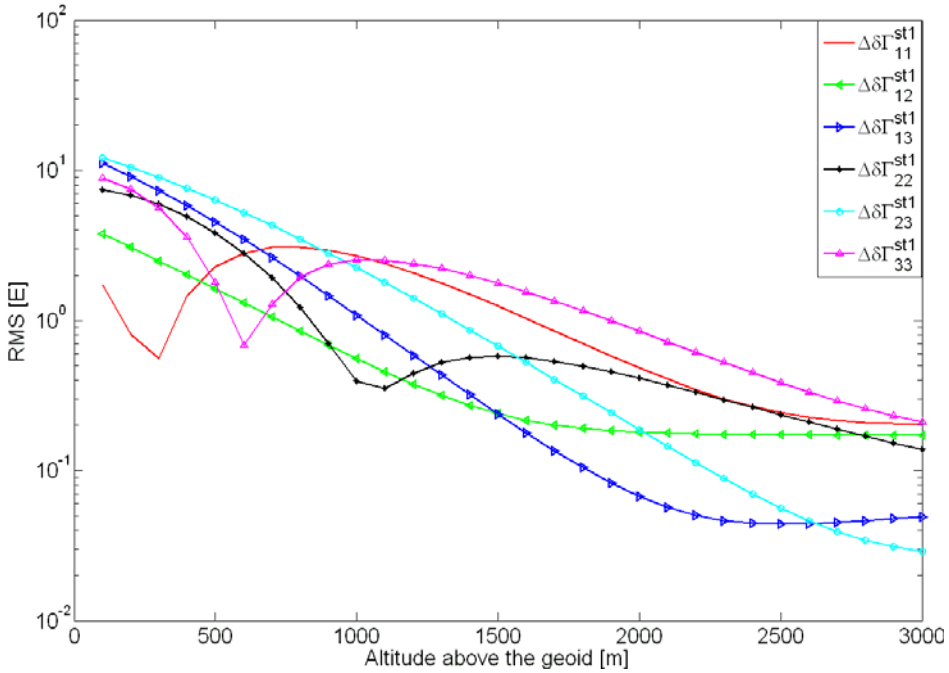

Figure 3.5: RMS of $\Delta\delta\Gamma_{jk}^{st1}$ (gravity anomaly extent: $1^{\circ}\times 1^{\circ}$; resolution: 1').

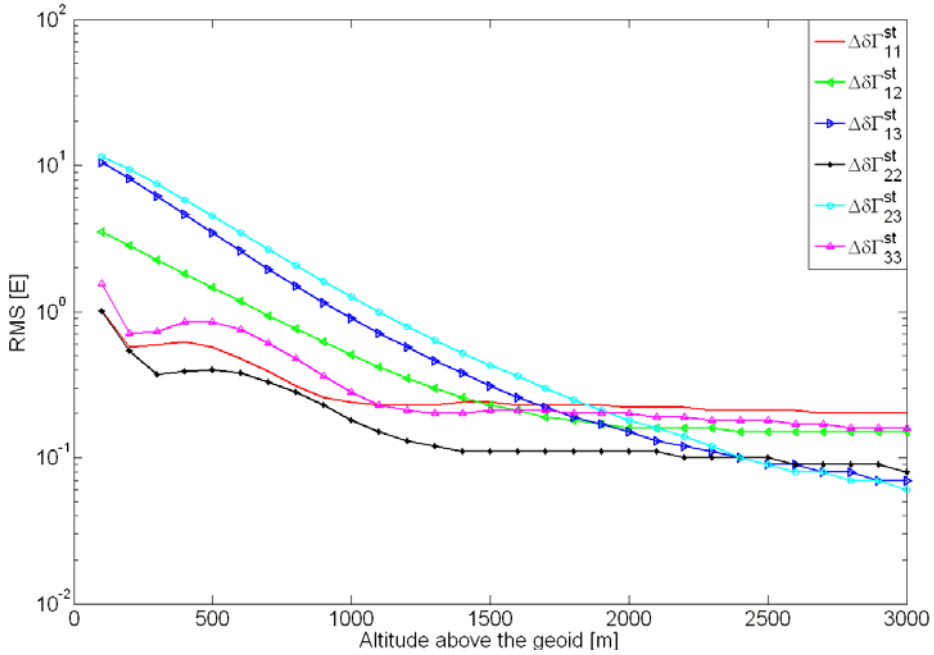

Figure 3.6: RMS of $\Delta\delta\Gamma^{st}_{jk}$ (gravity anomaly extent: $1^\circ \times 1^\circ$; resolution: 1').

Table 3.3: RMS of $\Delta\delta\Gamma^{st1}_{jk}$ and $\Delta\delta\Gamma^{st}_{jk}$ (gravity anomaly extent: $1^\circ \times 1^\circ$, unit: E).

Altitude (m)	$\Delta\delta\Gamma^{st1}_{11}$	$\Delta\delta\Gamma^{st1}_{12}$	$\Delta\delta\Gamma^{st1}_{13}$	$\Delta\delta\Gamma^{st1}_{22}$	$\Delta\delta\Gamma^{st1}_{23}$	$\Delta\delta\Gamma^{st1}_{33}$
100	1.7231	3.7753	11.081	7.4214	12.153	8.8493
500	2.2675	1.6298	4.516	3.8189	6.317	1.7835
1000	2.6942	0.5579	1.0844	0.3921	2.245	2.5271
1500	1.2427	0.2396	0.2375	0.5772	0.6728	1.7674
2000	0.4836	0.1805	0.0674	0.4125	0.1875	0.8463
2500	0.2431	0.1733	0.0441	0.2358	0.0563	0.3863
3000	0.2032	0.1717	0.0494	0.1389	0.0291	0.2107
Altitude(m)	$\Delta\delta\Gamma^{st}_{11}$	$\Delta\delta\Gamma^{st}_{12}$	$\Delta\delta\Gamma^{st}_{13}$	$\Delta\delta\Gamma^{st}_{22}$	$\Delta\delta\Gamma^{st}_{23}$	$\Delta\delta\Gamma^{st}_{33}$
100	1.0285	3.5757	10.633	1.0136	11.597	1.5694
500	0.5879	1.5007	3.5319	0.4044	4.5522	0.8665
1000	0.2654	0.5423	0.9154	0.1851	1.2716	0.3086
1500	0.2555	0.263	0.3237	0.1119	0.4344	0.2246
2000	0.2417	0.1973	0.1566	0.1083	0.1821	0.2132
2500	0.2278	0.1823	0.1007	0.0965	0.0941	0.1916
3000	0.219	0.1769	0.0808	0.0855	0.0623	0.1761

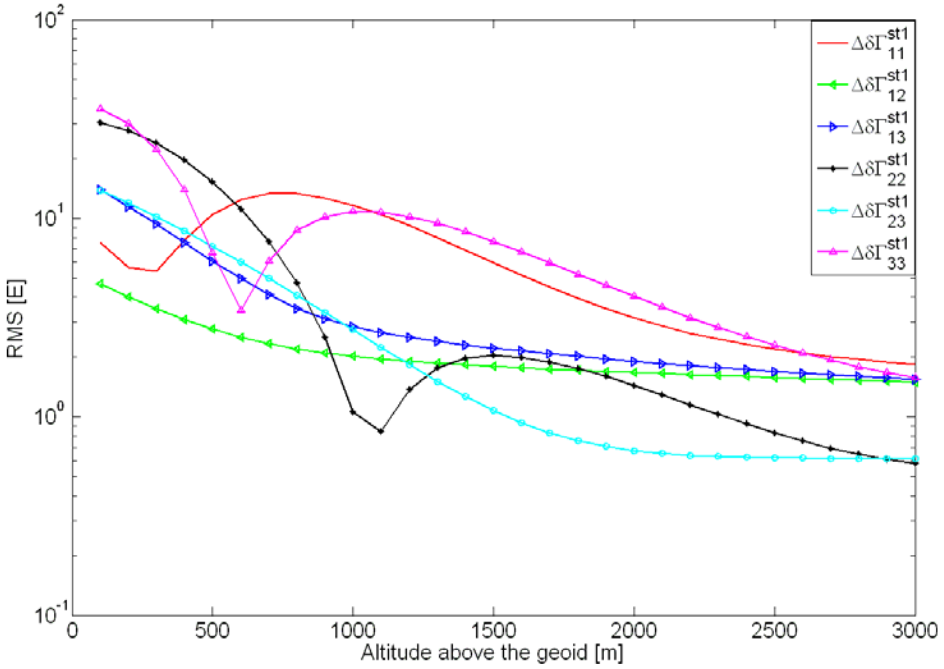

Figure 3.7: RMS of $\Delta\delta\Gamma^{st1}_{jk}$ (gravity anomaly extent: $2^\circ \times 2^\circ$, resolution: 1').

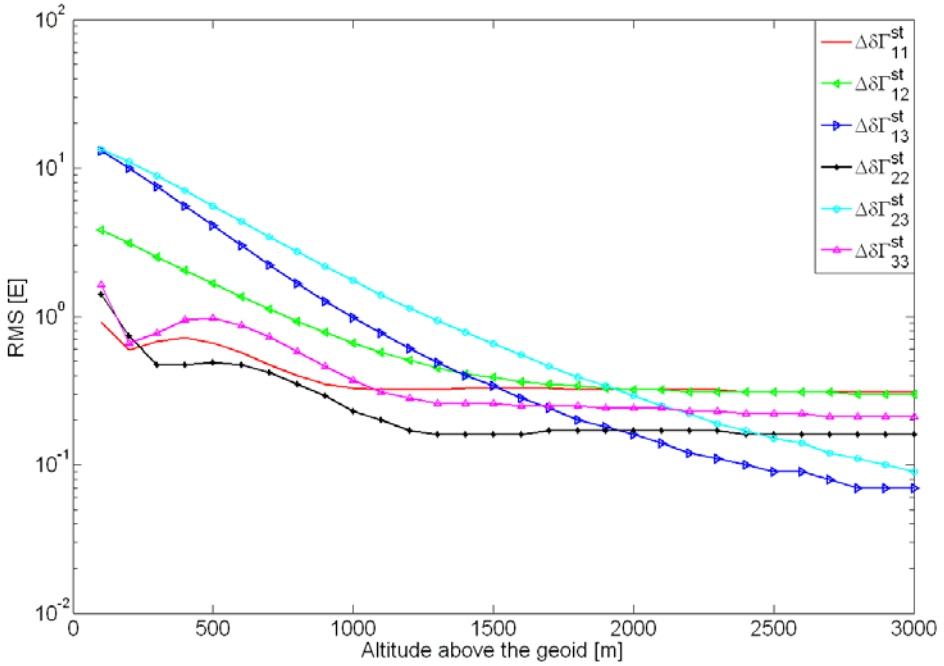

Figure 3.8: RMS of $\Delta\delta\Gamma^{st}_{jk}$ (gravity anomaly extent: $2^\circ \times 2^\circ$, resolution: 1').

Table 3.4: RMS of $\Delta\delta\Gamma_{jk}^{st1}$ and $\Delta\delta\Gamma_{jk}^{st}$ (gravity anomaly extent: $2^\circ \times 2^\circ$, unit: E).

Altitude	$\Delta\delta\Gamma_{11}^{st1}$	$\Delta\delta\Gamma_{12}^{st1}$	$\Delta\delta\Gamma_{13}^{st1}$	$\Delta\delta\Gamma_{22}^{st1}$	$\Delta\delta\Gamma_{23}^{st1}$	$\Delta\delta\Gamma_{33}^{st1}$
100	7.5638	4.6667	13.892	30.234	13.863	35.624
500	10.491	2.7668	6.1058	15.208	7.2483	6.7371
1000	11.642	2.0161	2.8389	1.0588	2.7376	10.796
1500	5.965	1.7967	2.2225	2.0342	1.0716	7.6444
2000	3.1494	1.6741	1.9061	1.4401	0.6752	4.0394
2500	2.1929	1.5772	1.6927	0.8294	0.6205	2.2904
3000	1.834	1.4945	1.5423	0.5837	0.6173	1.5761
Altitude	$\Delta\delta\Gamma_{11}^{st}$	$\Delta\delta\Gamma_{12}^{st}$	$\Delta\delta\Gamma_{13}^{st}$	$\Delta\delta\Gamma_{22}^{st}$	$\Delta\delta\Gamma_{23}^{st}$	$\Delta\delta\Gamma_{33}^{st}$
100	5.699	4.4349	13.284	1.7455	13.323	5.0248
500	4.3131	2.665	5.0409	0.7295	5.5728	3.8656
1000	2.9228	2.0145	2.8134	0.6378	1.849	2.3727
1500	2.3536	1.8025	2.2183	0.6503	0.8963	1.7843
2000	2.0587	1.6766	1.8923	0.6377	0.6864	1.5205
2500	1.8629	1.5785	1.6849	0.6102	0.6473	1.3541
3000	1.716	1.4955	1.5402	0.5844	0.6411	1.2297

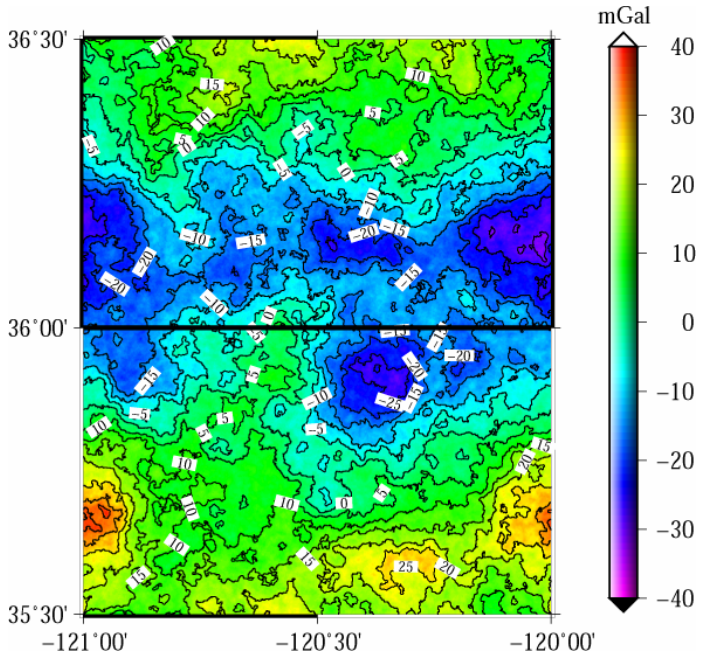

Figure 3.9: $1^\circ \times 1^\circ$ gravity anomaly field with 6" resolution generated by randomization of the psd shown in Figure 3.2 (the black line is central profile used for tests).

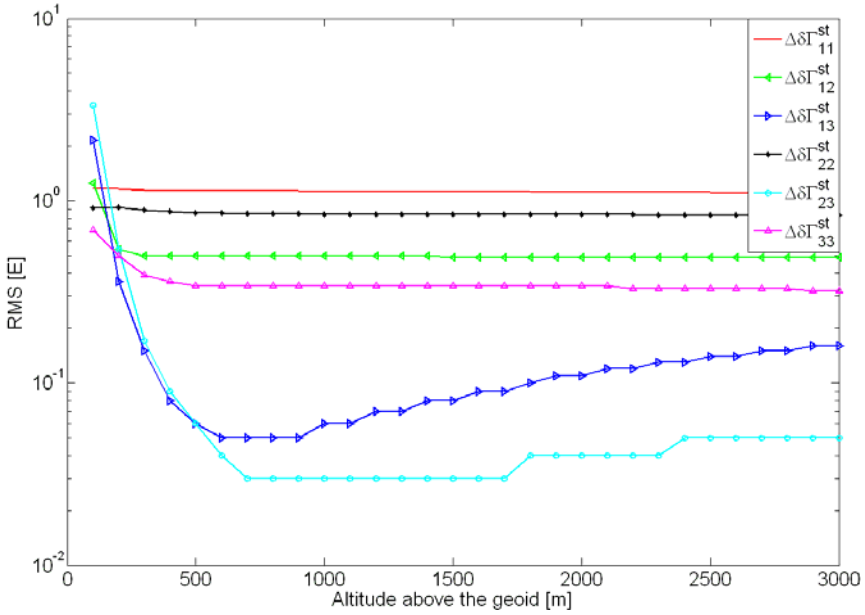

Figure 3.10: RMS of $\Delta\delta\Gamma^{st}_{jk}$ (gravity anomaly extent: $1^\circ \times 1^\circ$; resolution: 6").

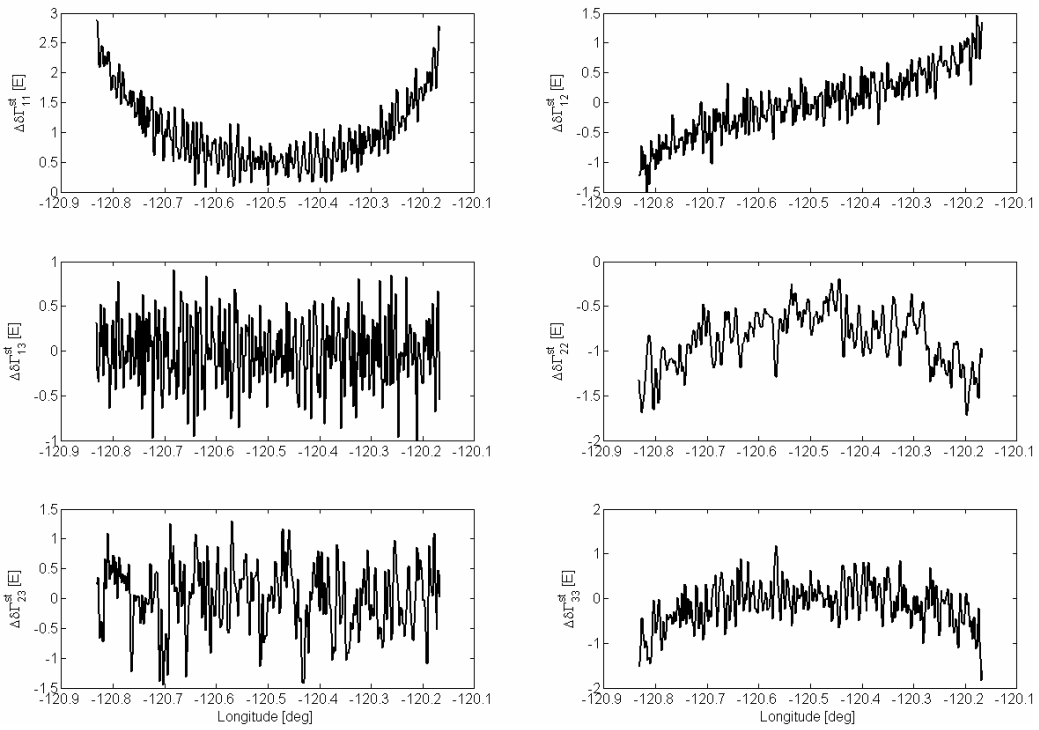

Figure 3.11: $\Delta\delta\Gamma^{st}_{jk}$ derived from gravity anomaly with 6" resolution at 200 m.

Table 3.5: Statistics of $\Delta\delta\Gamma_{jk}^{st}$ at 200 m (unit: E).

Statistics	$\Delta\delta\Gamma_{11}^{st}$	$\Delta\delta\Gamma_{12}^{st}$	$\Delta\delta\Gamma_{13}^{st}$	$\Delta\delta\Gamma_{22}^{st}$	$\Delta\delta\Gamma_{23}^{st}$	$\Delta\delta\Gamma_{33}^{st}$
Mean	1.0	0.0	0.0	-0.9	0.0	-0.1
Std	0.6	0.5	0.4	0.3	0.5	0.5
Min	0.1	-1.5	-1	-1.7	-1.4	-1.8
Max	2.9	1.5	0.9	-0.2	1.3	1.2

After investigating the Stokes' integral method, we also considered spherical splines and least-squares collocation (LSC) on the basis of all 3600 gravity anomaly data shown in Figure 3.2 to compute the gradient disturbances on points along the test profile in the center of Figure 3.2. For the spherical splines, we first determined the numbers, A_l, for $l = 0,\ldots,10800$, with the selection of parameters ($k = 2$, $\psi = 5'$) according to (3.43) and (3.44), where the degree, 10800, corresponds to the resolution of 1 arc minute. From (3.41) and (3.42), the kernel function of the disturbing potential is a convolution of two identical second order polynomial functions, which ensures the kernel is supported on the local area with the radius of $\psi = 5'$. Thus, we compute the kernel function for the gravity anomaly in terms of spherical distance using (3.48) to produce a list of values at an interval of 1 arcsec. Comparing (3.48) to (3.63), we can find the kernel function is a special case of the covariance function, where the "degree variance" is determined by the parameters, A_l and k. For the purpose of comparison between the spline kernel function and gravity anomaly covariance function, the spline kernel function value is normalized with respect to the value at $\psi = 0$. Figure 3.12 verifies the local support property of the spline kernel function that it converges to zero when the spherical distance is greater than 5 arcmin. From 3600 gravity anomaly data, the values of the spline kernel function for respective point pairs in the matrix of (3.49) were evaluated by the interpolations from the kernel-value table. Denote this matrix as K. 3600 coefficients were solved according to (3.50). Despite the local support of 5 arcmin (radius), the matrix to be inverted has several very small eigenvalues. Therefore we use singular-value decomposition (SVD) to determine an approximation of the inverse (Xu, 1998). The matrix, K is decomposed as

$$K = U\Lambda_n V, \tag{3.76}$$

where $\Lambda_n = \begin{pmatrix} \lambda_1 & & 0 \\ & \ddots & \\ 0 & & \lambda_n \end{pmatrix}$, λ_i, $i = 1,\ldots,n$ are eigenvalues, U and V are two unitary(the multiplication between it and its conjugate matrix is identity matrix) matrices. Generally, the inverse of K matrix is given by

$$K^{-1} = V^T\Lambda_n^{-1}U^T, \tag{3.77}$$

Figure 3.13 shows that some eigenvalues are much smaller. If small eigenvalues are used in (3.77) for the matrix inverse, the result will be numerically unstable and inaccurate. The relatively small eigenvalues are neglected in SVD to obtain the inverse.

Usually we choose a threshold, $\lambda_t = 10^{-6}$, so all eigenvalues below 10^{-6} were discarded. Thus the inverse of K matrix is

$$K^{+} = V^{T}\Lambda^{+}U^{T}, \tag{3.78}$$

where $\Lambda^{+} = \begin{pmatrix} \Lambda_t^{-1} & 0 \\ 0 & 0 \end{pmatrix}$. With the resulting spline coefficients, c_i, we computed the gradient disturbances at points along the test profile according to ((3.51). The results are presented in Figure 3.14 and 3.15 and in Table 3.6 and 3.7.

For least-squares collocation (LSC), first the empirical gravity anomaly covariance values associated with the spherical distance, ψ, were computed on the basis of 3600 gravity anomaly data:

$$cov_{\Delta g}(\psi_i) = \frac{1}{N_i}\sum_{j,k}^{N_i} \Delta g(\theta_j, \lambda_j)\Delta g(\theta_k, \lambda_k). \tag{3.79}$$

where $\psi_i = i\Delta\psi$, $i = 0,\ldots,120$, $\Delta\psi = 0'.5$, and N_i is the number of pairs of points whose distance is in the interval, $[\psi_i - \Delta\psi, \psi_i + \Delta\psi]$. The products are calculated for N_i pairs of points. Second, the degree variance model, (3.67), was used to generate the modeled covariance values according to (3.63). The parameters, $l_{\min}$, $l_{\max}$, A_0 and R_b are to be estimated by the empirical values. COVFIT program in GRAVSOFT computer software (Tscherning, et al., 1992) was used to compute parameters: $l_{\min} = 361$, $l_{\max} = 10800$, $A_0 = 320 mGal^2$, $R_b = R - 2389m$, and $R = 6371km$. Furthermore, this degree variance model can be transformed to a corresponding PSD of gravity anomaly (Jekeli, 2003):

$$\Phi_{\Delta g}(f) = \frac{2\pi R^2 c_l}{l}, \text{ where } f = \frac{l}{2\pi R}. \tag{3.80}$$

Figure 3.2 shows that the PSD derived from the degree variance model is an approximation of the PSD used to generate the synthetic gravity anomaly data.

The gradients are determined according to (3.68). We assume the observed anomalies are the synthetic data, and thus are error free, so we used a value of 0 $mGal^2$ as the variance for the observation noise. Here the gradient disturbances on points along the test profile are computed using the $1^{\circ}\times 1^{\circ}$ gravity anomaly data shown in Figure 3.2.

The results are shown in Figures 3.14 and 3.15, where modeled gradient disturbances derived from Stokes' integral, spherical splines and LSC are compared to true gradient disturbances at 600 m and 1200 m altitude. Tables 3.6 and 3.7 give their statistics of the differences (we neglected 10 records at each side of the profile in order to avoid the edge effects). Denote these differences as $\Delta\delta\Gamma_{jk}^{st}$, $\Delta\delta\Gamma_{jk}^{sp}$ and $\Delta\delta\Gamma_{jk}^{LSC}$. At 600 m, the standard deviations of the differences of $\Delta\delta\Gamma_{11}^{st}$, $\Delta\delta\Gamma_{22}^{st}$ and $\Delta\delta\Gamma_{33}^{st}$ are between 0.4 E and 0.7 E, but those of are $\Delta\delta\Gamma_{12}^{st}$, $\Delta\delta\Gamma_{13}^{st}$ and $\Delta\delta\Gamma_{23}^{st}$ are between 1.2 E and 3.5 E; the standard deviation of $\Delta\delta\Gamma_{11}^{sp}$, $\Delta\delta\Gamma_{22}^{sp}$ and $\Delta\delta\Gamma_{33}^{sp}$ are between 1.5 E and 2.3 E, but standard deviation of $\Delta\delta\Gamma_{12}^{sp}$, $\Delta\delta\Gamma_{13}^{sp}$ and $\Delta\delta\Gamma_{23}^{sp}$ are between 2.4 E and 4.7 E; all $\Delta\delta\Gamma_{jk}^{LSC}$ have consistent standard deviation values (less than 1 E). Stokes' integral yields more accurate gradient disturbances than the spline method (in terms of the mean and standard deviation of

differences) and LSC yields more accurate gradient disturbances than Stokes' integral, except for $\delta\Gamma_{11}$.

At 1200 m altitude, the standard deviations of $\Delta\delta\Gamma_{11}^{st}$, $\Delta\delta\Gamma_{22}^{st}$ and $\Delta\delta\Gamma_{33}^{st}$ are less than 0.2 E, and the standard deviations of $\Delta\delta\Gamma_{12}^{st}$, $\Delta\delta\Gamma_{13}^{st}$ and $\Delta\delta\Gamma_{23}^{st}$ are less than 0.8 E; the standard deviations of $\Delta\delta\Gamma_{11}^{sp}$, $\Delta\delta\Gamma_{22}^{sp}$ and $\Delta\delta\Gamma_{33}^{sp}$ are less than 3.2 E, and those of $\Delta\delta\Gamma_{12}^{sp}$, $\Delta\delta\Gamma_{13}^{sp}$ and $\Delta\delta\Gamma_{23}^{sp}$ are as large as 2.9 E; the standard deviations of $\Delta\delta\Gamma_{jk}^{LSC}$ are between 0.1 E and 0.5 E. For both the Stokes' integral and spline methods, the in-line gradient disturbances generally have smaller standard deviations than the off-diagonal components. The standard deviation of $\Delta\delta\Gamma_{jk}^{st}$ is less than 4 E and that of $\Delta\delta\Gamma_{jk}^{LSC}$ is less than 3 E. LSC and Stokes' integral methods yield similar accuracy, although the LSC method appears more accurate at the lower altitude. The Stokes' integral method yields worse results at 600 m altitude than at 1200 m because the resolution of input data is 1 arcmin (about 2 km), which is three times 600 m.

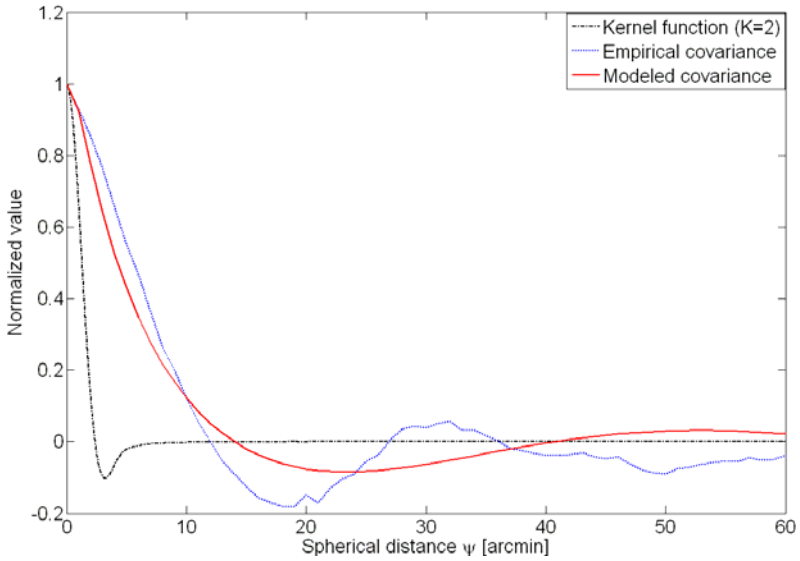

Figure 3.12: Spline kernel function vs. Covariance function for the gravity anomaly.

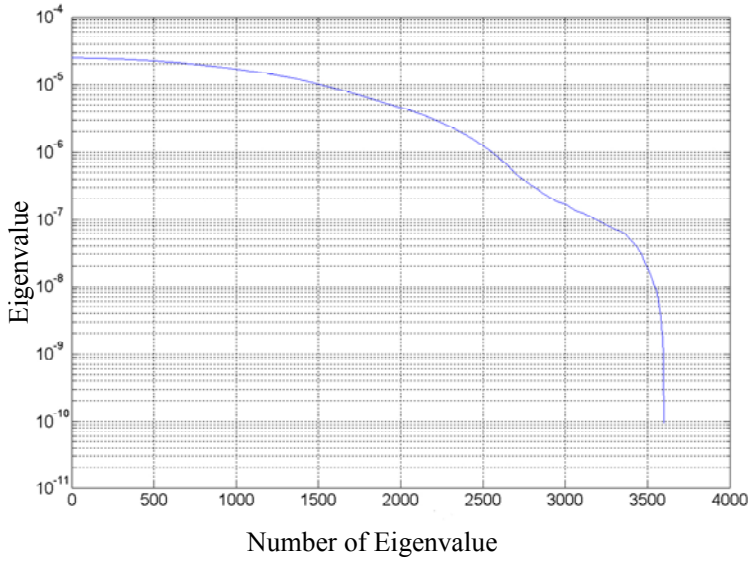

Figure 3.13: Eigenvalue of kernel matrix.

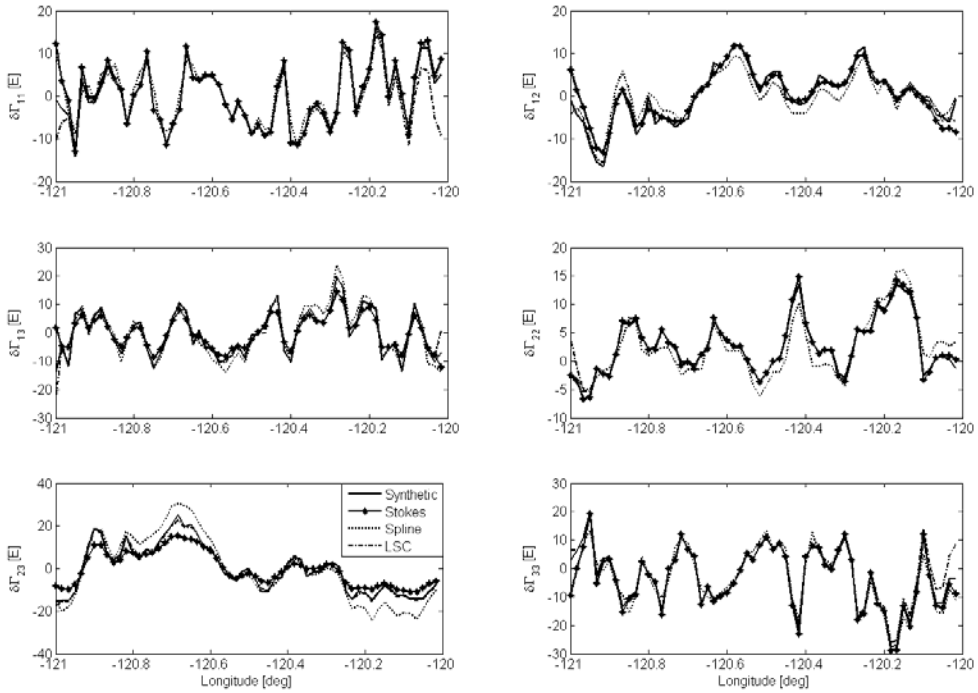

Figure 3.14: Modeled and true (synthetic) gradient disturbances at 600 m altitude.

Table 3.6: Statistics of $\Delta\delta\Gamma_{jk}^{st}$, $\Delta\delta\Gamma_{jk}^{sp}$ and $\Delta\delta\Gamma_{jk}^{LSC}$ at 600m (unit: E).

Statistics	$\Delta\delta\Gamma_{11}^{st}$	$\Delta\delta\Gamma_{12}^{st}$	$\Delta\delta\Gamma_{13}^{st}$	$\Delta\delta\Gamma_{22}^{st}$	$\Delta\delta\Gamma_{23}^{st}$	$\Delta\delta\Gamma_{33}^{st}$
Mean	0.2	0.1	-0.2	0.0	-0.6	-0.2
Std	0.4	1.2	2.6	0.4	3.5	0.7
Min	-0.7	-3.0	-6.0	-0.6	-9.6	-2.3
Max	1.3	2.5	3.9	1.3	5.3	1.1
	$\Delta\delta\Gamma_{11}^{sp}$	$\Delta\delta\Gamma_{12}^{sp}$	$\Delta\delta\Gamma_{13}^{sp}$	$\Delta\delta\Gamma_{22}^{sp}$	$\Delta\delta\Gamma_{23}^{sp}$	$\Delta\delta\Gamma_{33}^{sp}$
Mean	0.8	-0.9	0.3	-1.2	1.2	0.4
Std	1.7	2.4	2.6	1.5	4.7	2.3
Min	-2.0	-3.9	-4.7	-3.9	-9.8	-5.4
Max	5.0	5.7	5.5	2.2	9.8	4.7
	$\Delta\delta\Gamma_{11}^{LSC}$	$\Delta\delta\Gamma_{12}^{LSC}$	$\Delta\delta\Gamma_{13}^{LSC}$	$\Delta\delta\Gamma_{22}^{LSC}$	$\Delta\delta\Gamma_{23}^{LSC}$	$\Delta\delta\Gamma_{33}^{LSC}$
Mean	-0.4	0.0	0.0	0.0	0.0	0.4
Std	0.5	0.5	0.7	0.1	0.9	0.4
Min	-1.8	-1.1	-1.2	-0.2	-2.1	-0.3
Max	0.4	1.2	1.1	0.2	2.3	1.6

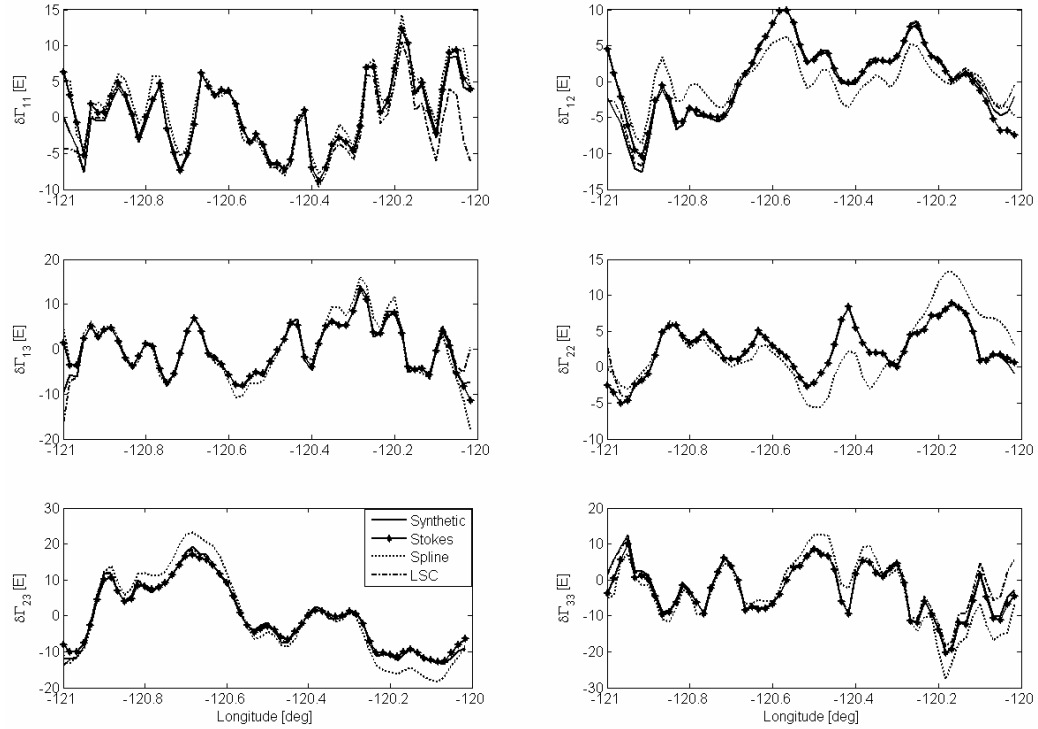

Figure 3.15: Modeled and true (synthetic) gradient disturbances at 1200m altitude.

Table 3.7: Statistics of $\Delta\delta\Gamma^{st}_{jk}$, $\Delta\delta\Gamma^{sp}_{jk}$ and $\Delta\delta\Gamma^{LSC}_{jk}$ at 1200m altitude (unit: E).

Statistics	$\Delta\delta\Gamma^{st}_{11}$	$\Delta\delta\Gamma^{st}_{12}$	$\Delta\delta\Gamma^{st}_{13}$	$\Delta\delta\Gamma^{st}_{22}$	$\Delta\delta\Gamma^{st}_{23}$	$\Delta\delta\Gamma^{st}_{33}$
Mean	0.1	0.1	0.0	-0.1	-0.1	-0.1
Std	0.1	0.3	0.5	0.1	0.8	0.2
Min	-0.1	-0.6	-1.4	-0.3	-2.1	-0.7
Max	0.6	1.0	0.9	0.1	1.4	0.3
	$\Delta\delta\Gamma^{sp}_{11}$	$\Delta\delta\Gamma^{sp}_{12}$	$\Delta\delta\Gamma^{sp}_{13}$	$\Delta\delta\Gamma^{sp}_{22}$	$\Delta\delta\Gamma^{sp}_{23}$	$\Delta\delta\Gamma^{sp}_{33}$
Mean	0.8	-1.1	0.2	-1.3	0.6	0.5
Std	1.2	2.5	1.7	2.4	2.9	3.2
Min	-1.5	-4.0	-2.7	-6.0	-4.8	-7.2
Max	3.4	4.6	4.1	5.1	5.4	7.1
	$\Delta\delta\Gamma^{LSC}_{11}$	$\Delta\delta\Gamma^{LSC}_{12}$	$\Delta\delta\Gamma^{LSC}_{13}$	$\Delta\delta\Gamma^{LSC}_{22}$	$\Delta\delta\Gamma^{LSC}_{23}$	$\Delta\delta\Gamma^{LSC}_{33}$
Mean	-0.4	0.0	0.0	0.0	0.0	0.4
Std	0.5	0.1	0.1	0.1	0.3	0.4
Min	-1.8	-0.3	-0.2	-0.1	-0.6	-0.3
Max	0.3	0.4	0.2	0.2	0.7	1.6

3.7 Conclusion

We developed three different methods to model gradient disturbances at aircraft altitude from gravity anomaly data on the geoid. The methods include Stokes' integral, a radial-basis spline representation, and least-squares collocation; and, they all are based on the solution for the boundary-value problem and incorporate upward continuation of the gradient disturbances.

Stokes' integral method determines gradient disturbances by differentiating the disturbing potential computed from Stokes' integral. In local areas, the planar approximation of Stokes' function can be used to make the integral computation convenient and simple. Stokes' integral has a limitation in computing off-diagonal gradients at lower altitude or at ground level, because of singularities in the kernel function. These problems need to be solved by the inner zone technique, where the horizontal derivatives of the gravity anomalies data need to be calculated from the grid point values. The accuracy of Stokes' integral depends on the resolution of gravity data and the altitude of computation. A simulation based on 6"×6" gravity anomaly data in a $1^\circ \times 1^\circ$ area shows that 1 E accuracy can be reached when the computation altitude is at or above 200 m. For lower resolution gravity anomaly data, e.g. 1'×1' , 1 E accuracy can be reached when the computation altitude is above 1200 m.

The radial-basis spline method models gradient disturbances by solving the coefficients of a spline representation of the gravity anomaly data. Least-squares collocation models gradient disturbances from the gravity anomaly data on the basis of a covariance model determined from empirical values. Both the splines method and LSC

are similar in how they model the gradient disturbances from gravity data. The kernel function in the spline method is analogous to the covariance function, but determined only with respect to the region of local support. The covariance function in LSC is determined from the empirical values which are evaluated using all data. Also LSC can also account for data error in the determination of gradient disturbances. The parameters of the spline function are practically chosen on the basis of the resolution of gravity data and required order of the splines, where the resolution of gravity data gives the selection of the range, ψ and the order of the splines gives k. Different selections on the parameters in the spline model will yields different results. An optimal selection is necessary for this model. Several trials on different parameters show that the parameters ($k = 2, \psi = 5'$) yield the best results (with smallest standard deviation) with respect to the true (synthetic) gradient disturbances. For LSC, once we choose a covariance model, the parameters in this covariance model are estimated from empirical values which are computed from the gravity anomaly data. Thus it provides better results than radial-basis spline method.

These methods for modeling the gradient disturbances at altitude are tested using a synthetic gravity anomaly/gradient disturbance field. From the results of these tests, the planar approximation can replace the spherical approximation without significant error (rms: less than 0.1 E). Comparing the three methods, we find that, Stokes' integral method performs better than the radial-basis spline method. LSC estimates are comparable to the Stokes' integral results, but slightly more accurate when tested at the lower altitude. The accuracy of gradient disturbances determined from Stokes' integral depends on the resolution of input data and the altitude of upward continuation. Both radial-basis splines and least-squares collocation methods can use scattered data and grid point data, and they provide a complementary model for Stokes' integral in which scattered data need to be first interpolated on the grid points in order to achieve more accurate results using (3.25).

CHAPTER 4

GRADIENT MODEL BASED ON GRAVITY AND DEM

4.1 Introduction

The importance of gravity gradient modeling becomes more significant as instrumentation, particularly in airborne applications, becomes more accurate. A good gradient model derived from existing data sources aids in the pre-processing of airborne gradient data, as well as in detecting and interpreting residual density anomalies sought out by an airborne gradiometric survey. Gravity gradients can be modeled theoretically either from surface gravity and topographic data, or a combination of both. Some early studies in obtaining gradients from gravity data include those of Agarwal and Lal (1972) and Gunn (1975). More recent methods relied on Fourier Transform relationships among various derivatives of geopotential field (Mickus and Hinojosa, 2001). Most modeling of the gravity gradient, however, is based on topographic data since the gradients reflect primarily the near structures of the Earth's mass. A recent review of various associated methods was given by (Jekeli and Zhu, 2005), which is also elaborated here in Chapter 2. DEM data usually have much higher resolution than gravity data and thus DEM-derived gradient models inherit the resolution more nearly appropriate to this type of gravitational quantity. Nevertheless, depending on their resolution, gravity data grids also provide information on gradients at the corresponding wavelengths. In fact, they more accurately reflect lateral density variation that may be missing in the topographically-derived model that is usually based on a constant density assumption.

Chapter 2 and Chapter 3 give the approaches to model the gradients respectively from DEM data and gravity data. In this chapter, we develop a unified approach to model gradients at aircraft altitude from a combination of surface gravity and terrain elevation data, and consider the power spectral densities of gradients. The objectives of the analysis are to verify the significant attenuation of the gradient signal with altitude, to study the dependence of the model at aircraft altitude on typical density variability in the topographic masses, and to develop a validation and calibration approach for airborne gradiometry. A comparison and analysis between the modeled gradients and actual FTG (Full Tensor Gradient) data is also given in this chapter.

4.2 Principle of the gradient model

4.2.1 Gradients from residual gravity anomalies

Gradient modeling from gravity anomalies is based on the solution to the boundary-value problem in the potential theory, such as Stokes' integral, radial-basis splines or least-squares collocation. From these solutions, we obtain the gradient disturbances by differentiation with appropriate transformations between the spherical and local Cartesian coordinate systems.

Given free-air gravity anomaly data, we need to process these appropriately for a consistent combination with DEM data. As we know, Stokes' formula is the solution of an exterior boundary value problem which implies that there is no mass outside the geoid (where the gravity anomalies are supposed to provide). This is a fundamental assumption in the problem of determining the potential, and we need to reduce the gravity anomaly data from the Earth's surface in a suitable way. Since the boundary is the geoid, we remove all masses above the geoid in our model, neglecting the atmospheric effect (it is negligibly small for gradients (about 10^{-5} E)). It will produce an indirect effect due the mass change of the Earth. The gravity effect due to the DEM is separated into two parts, the Bouguer plate, and the terrain correction. Without restoring the masses, the indirect effect would be too large, and thus we use the second Helmert condensation principle to restore the masses as a condensed layer onto the geoid. Once the masses are restored in this manner, the total reduction for the gravity is mainly the terrain correction since the Bouguer plate effect cancels under a planar approximation (Wang and Rapp, 1990) and the reduced free-air anomaly becomes the Faye anomaly. In the problem of determining the precise geoid, we would still need to consider the indirect effect after applying the remove/restore Helmert condensation process. However, this aspect is slightly different in our case since we wish to compute gradients, not to determine the geoid.

Together with the second Helmert condensation, we also refer the anomalies to EGM96 in order to reduce the long-wavelength errors coming from the truncation of the integral. Thus we apply Stokes' formula to residual gravity anomalies and from this to compute residual gradient disturbances. Using (3.3), we have

$$\delta\Gamma_{jk}\big|_{residual} = \frac{R}{4\pi}\iint_{\sigma}\left(\Delta g - \Delta g_{\text{terrain}} - \Delta g_{\text{EGM96}}\right)\frac{\partial^2 S(r,\psi)}{\partial x_j \partial x_k}\,d\sigma\,, \tag{4.1}$$

where EGM96-derived gravity anomaly can be evaluated from the coefficients of EGM96 model (Lemoine, et al., 1998),

$$\Delta g_{EGM96}(\theta,\lambda) = \frac{GM}{R^2}\sum_{n=2}^{360}\sum_{m=0}^{n}(n-1)\left(C_{nm}\cos m\lambda + S_{nm}\sin m\lambda\right)\overline{P}_{nm}(\cos\theta)\,, \tag{4.2}$$

where GM is Newton's gravitational constant times Earth's total mass, C_{nm} and S_{nm} are the harmonic coefficients of EGM96 (the even-degree zonal value of C_{nm} represents the difference between the EGM96 coefficient and the reference values computed for the WGS84 ellipsoid) , and $\overline{P}_{nm}$ are the normalized Legendre functions. The terrain effect on gravity due to the remove/restore Helmert condensation process is

$$\Delta g_{terrain} = -c_p \,, \tag{4.3}$$

The terrain correction, c_p, at point $P\left(x_1, x_2, x_3 = h_P\right)$ is given (Wang and Rapp, 1990) in planar approximation by

$$c_p = G\rho \int_{x_1'} \int_{x_2'} \int_{h_p}^{h} \left(\frac{x_3' - h_P}{l^3} \right) dx_3' dx_2' dx_1' \,, \tag{4.4}$$

where l is the distance between the point P and the integration point, $P'\left(x_1', x_2', x_3'\right)$. Integrating (4.4) with respect to x_3', we can get the terrain correction (Wang and Rapp, 1990)

$$\begin{aligned} c_p &= G\rho \int_{x_1'} \int_{x_2'} \left(\frac{1}{s} - \frac{1}{s} \left(1 + \left(\frac{h_P - h}{s} \right)^2 \right)^{-1/2} \right) dx_2' dx_1' \\ &\approx \frac{1}{2} G\rho \int_{x_1'} \int_{x_2'} \frac{\left(h - h_P\right)^2}{s^3} dx_2' dx_1' \end{aligned} \,, \tag{4.5}$$

where s is the distance in the plane between P and P', which is given by

$$s = \sqrt{\left(x_1' - x_1\right)^2 + \left(x_2' - x_2\right)^2} \,. \tag{4.6}$$

Instead of using (4.1), the residual gradient disturbances also can be derived from radial-basis splines and least-squares collocation applied to the residual gravity anomalies, as was described in Chapter 3.

4.2.2 Gravity gradient from DEM and Gravity anomalies

The modeled gradients should reflect the signal sensed above the natural Earth's surface instead of a changed, mass redistributed Earth. In other words, gradients implied by reduced residual gravity anomalies in Stokes' formula reflect the gradients due to a changed gravity field. These are corrected by an effect analogous to the indirect effect of the Helmert condensation method, but applied to the gradients. In essence, we compute this effect by reversing the remove-restore process applied to the surface free-air gravity anomalies. Since the gravity anomaly is reduced by removing the terrain effect and restoring the layer effect, we need to remove the condensed layer effect and restore the terrain effect. We also can use Newton's density integration to compute the surface layer effect on the gradients. Therefore, we have

$$\delta\Gamma_{jk}\Big|_{\text{terrain}} = \Gamma_{jk}\Big|_{\text{DEM}} - \Gamma_{jk}\Big|_{\text{layer}} \,. \tag{4.7}$$

$\delta\Gamma_{jk}\Big|_{terrain}$ is the difference of gradient effects due to DEM and Helmert condensed layer on the geoid (this will be explained later). The gradients due to DEM can be derived using numerical integration, right rectangular prisms and polyhedra or FFT methods, as described in Chapter 2. Here we use the numerical integration method, given by the formula (2.34):

$$\Gamma_{jk}\Big|_{DEM} = G\rho\iint_A\int_0^h F_{jk}\,dx_3'\,dA = G\rho\iint_A T_{jk}\,dA\,. \tag{4.8}$$

Now the gravitational gradient due to a surface layer can be derived in a similar way. The density of the condensed layer given at any point by $\rho h(x_1', x_2')$, assuming $x_3 > 0$, so we get in planar approximation

$$\Gamma_{jk}\Big|_{layer} = G\rho\iint_A h(x_1', x_2')\frac{\partial^2}{\partial x_j \partial x_k}\left(\frac{1}{r_0}\right)dA\,. \tag{4.9}$$

with $r_0 = \sqrt{(x_1 - x_1^0)^2 + (x_2 - x_2^0)^2 + x_3^2}$. We may write this as

$$\Gamma_{jk}\Big|_{layer} = G\rho\iint_A h(x_1', x_2')F_{jk}'\,dA\,, \tag{4.10}$$

where F_{jk}' is slightly different from F_{jk} due to the degeneration of $x_3' = 0$,

$$F_{11}' = -\frac{1}{r_0^3} + \frac{3(x_1 - x_1')^2}{r_0^5}, F_{12}' = \frac{3(x_1 - x_1')(x_2 - x_2')}{r_0^5}, F_{13}' = \frac{3(x_1 - x_1')x_3}{r_0^5},$$

$$F_{22}' = -\frac{1}{r_0^3} + \frac{3(x_2 - x_2')^2}{r_0^5}, F_{23}' = \frac{3(x_2 - x_2')x_3}{r_0^5},$$

$$F_{33}' = -\frac{1}{r_0^3} + \frac{3x_3^2}{r_0^5}. \tag{4.11}$$

Clearly when $x_3 = 0$, (4.9) is invalid, since the derivative of the potential on the surface are not continuous. One can refer (1.17a) and (1.19a) in (Heiskanen & Moritz, 1967) to derive respective formulas. Here we list the first-order derivatives of the potential at the layer surface due to the layer:

$$\frac{\partial V_{layer}}{\partial x_1} = G\rho\iint_A h(x_1', x_2')\frac{\partial}{x_1}\left(\frac{1}{r_0}\right)dA$$

$$\frac{\partial V_{layer}}{\partial x_2} = G\rho\iint_A h(x_1', x_2')\frac{\partial}{x_2}\left(\frac{1}{r_0}\right)dA$$

$$\frac{\partial V_{layer}}{\partial x_3} = -2\pi G\rho h + G\rho\iint_A h(x_1', x_2')\frac{\partial}{x_3}\left(\frac{1}{r_0}\right)dA \tag{4.12}$$

The second-order derivatives are straightforwardly evaluated on the basis of (4.12).

Finally, we complete our model for the gradient disturbances (Zhu and Jekeli, 2007):

$$\delta\Gamma_{jk} = \delta\Gamma_{jk}\Big|_{\mathrm{EGM96}} + \frac{R}{4\pi}\iint_\sigma \left(\Delta g - \Delta g_{\mathrm{terrain}} - \Delta g_{\mathrm{EGM96}}\right)\frac{\partial^2 S(r,\psi)}{\partial x_j \partial x_k}\,d\sigma + \delta\Gamma_{jk}\Big|_{\mathrm{terrain}}. \tag{4.13}$$

The gradient disturbance (neglecting air effect) is composed of three parts: one is the residual gradient disturbance due to the residual gravity anomaly, the second is the EGM96-derived gradient disturbance, which is always smooth over the local area for its low resolution and can be regarded as a bias, and the third one is the terrain effect, which is the difference between the gradients due to the terrain mass and the condensed mass

layer. The EGM96-derived gradient disturbances are obtained from the global spherical harmonic model, EGM96 (Lemonie et al., 1998). Given in the spherical coordinates, (r,θ,λ), we have

$$\Gamma_{jk}(r,\theta,\lambda)\big|_{EGM96} = \frac{GM}{R}\sum_{n=2}^{360}\sum_{m=0}^{n}\frac{\partial^2 T_{nm}}{\partial x_j \partial x_k}, \tag{4.14}$$

with $T_{nm} = \left(\frac{R}{r}\right)^{n+1}\left(C_{nm}\cos m\lambda + S_{nm}\sin m\lambda\right)\overline{P}_{nm}(\cos\theta)$. Further derivations of (4.14) are given in Appendix B. As we know, gravity data contribute the longer wavelength signal of the gradient, the EGM96-derived gradient disturbances are the biases due to the low resolution of the model, and the terrain effects provide the high frequency components of the gradient.

In summary, we first remove the gravitational effect of the topographic masses above the geoid from the gravity anomalies and determine also the effect of the masses as a condensed surface layer on the geoid. These reduced gravity anomalies are further modified by removing the effect of a global model, such as EGM96 and can then be used in Stokes' formula. After applying Stokes' formula, we account for the indirect effect by reversing the whole remove-restore process by removing the gradient effect due to the layer on the geoid and restoring the gradient effect due to DEM. Finally we obtain the gradient disturbances from this procedure.

4.3 Airborne gradiometry survey in Parkfield, CA

4.3.1 Gradiometer data:

Airborne gravity gradient data were collected over the Parkfield experimental area near Parkfield, CA in September, 2004 by Bell Geospace (Bell Geospace, 2004; Talwani, 2004). The Town of Parkfield is situated on a relatively straight section of San Andreas faults in central California. The gradiometer instrument used in this survey is the Full Tensor Gradient (FTG) Instrument System developed by Bell Geospace, and is shown on the left of Figure 4.1. The gradiometer is installed in the aircraft, a Cessna Grand Caravan C-GSKT, shown on the right of Figure 4.1. Some additional equipment including control electronics, computers, monitors, printers, and air conditioning and other peripheral devices are onboard to support the FTG data acquisition. An airtight case was used to contain the FTG in order to provide it a temperature, pressure, and humidity controlled environment during data acquisition. Gradiometry data are acquired in an internal coordinate system which is referenced to the axes of three Gravity Gradient Instruments (GGIs) that are the primary measurement components of the FTG and output in-line and cross gradients. The final data are transformed from the internal coordinate system of the GGIs into a left handed coordinate system with x and y in the horizontal plane and z normal to that plane and pointing down. FTG data are acquired continuously, with the gyro output at 1024 Hz and the GGI output at 128 Hz, throughout the flight at ground speeds of approximately 62 m/s. The position of the FTG system was obtained by a Novatel Propak OEM4 airborne differential GPS System. It has an accuracy of ±5 meters and positions were real-time differentially corrected with an Omni-Star system. The

latitude and longitude coordinates collected by GPS and DGPS system are relative to the WGS-84 ellipsoid, and the final data are projected onto the Universal Transverse Mercator (UTM) Zone 10N using the WGS-84 ellipsoid. The GPS system is used in conjunction with a GPS-based PNAV-2001 navigation system to provide interactive information (both a heads-up pilots display (left/right of track) and a moving map representation of where the aircraft is in relation to the survey area) for the operator. The FTG data, plus the navigation data and the plane's acceleration data obtained from DGPS and GGI outputs, are recorded at the rate of about 400MB/hour. During the data acquisition, FTG onboard quality control was carried out by inspecting the in-line gradient sums and cross gradients, position and temperature of the gyros, GGI case temperatures and the north, east, and the vertical accelerations. The principal survey lines are in the northwest-southeast direction with 200 m spacing (see Figure 4.2). The tie lines are oriented in the northeast-southwest with 1000 m spacing. There are 49 principal lines and 10 tie lines in the survey, so there are 490 cross-over points, which can be used to analyze the internal accuracy of FTG data. This analysis is given in the following section.

Table 4.1 gives the statistics of the terrain elevation, aircraft altitude and the ground clearance. From Table 4.1, the maximum and minimum elevations of the terrain are 1064.3 m and 410 m respectively. The variation of the elevation is about 600 m in the survey area. The aircraft altitude was typically 400 m above the ground surface, but due to the change of terrain, the maximum clearance is much larger than 400 meters over the ground surface.

Figure 4.1 FTG gradiometer and Aircraft (Bell Geospace, 2004)

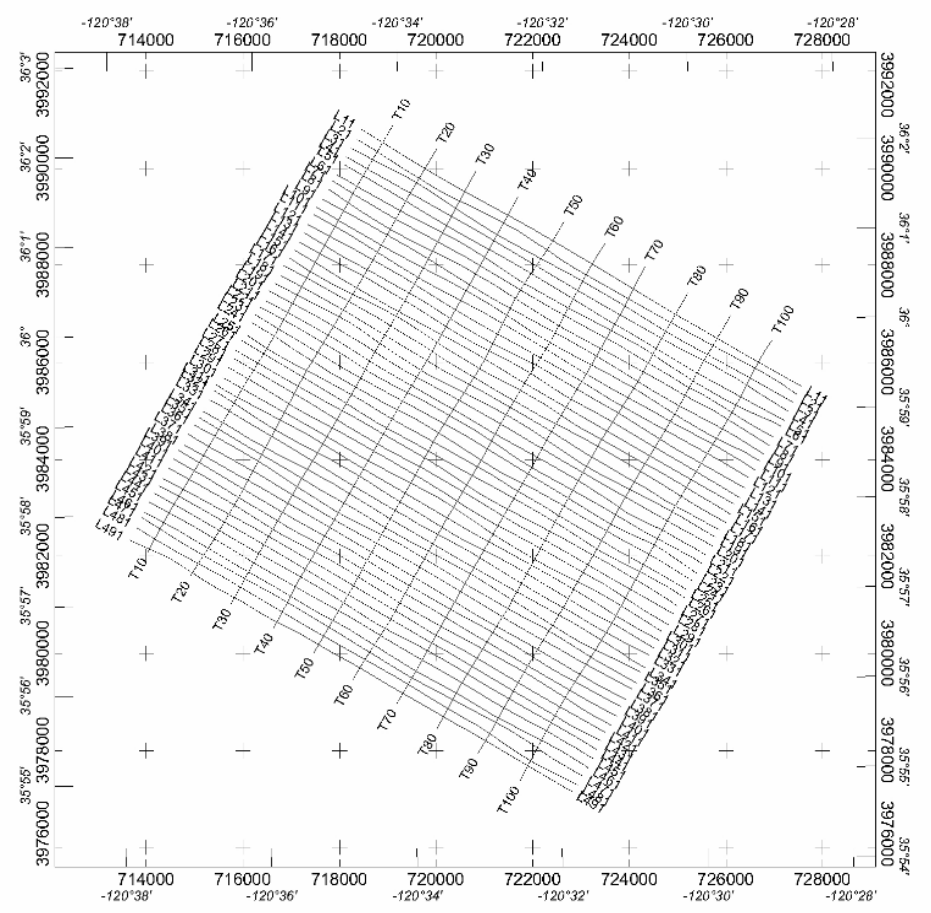

Figure 4.2: Gradient Data Survey Lines (Bell Geospace, 2004)

Table 4.1: Terrain and aircraft altitude statistics (unit: m). (Bell Geospace, 2004)

Statistics	Min	Max	Std Dev	Mean
Terrain above geoid	410	1064.3	108.0	705.7
GPS altitude above geoid	839.4	1350.5	109.9	1096.4
Ground clearance	183.4	674.5	93.5	390.7

4.3.2 Post processing of gravity gradient data

Figure 4.3 presents the procedures used by Bell Geospace to process the FTG data. First, FTG and GPS collect the raw data in the survey. SAR (Strip, average and reformat) procedure is applied on these raw data in order to strip out the necessary elements, average the values and reformat it into a 24-column binary file. In this procedure, the navigation and the attitude data obtained from DGPS and a PNAV-2001 navigation system are merged with the gradient data. These data are then processed by the High-Rate Post Mission Compensation (HRPMC). This process works on the most highly sampled data of the gyro and GGI outputs and compensates the data for most of the physical conditions during signal acquisition including the corrections for the self-gradients of the aircraft and the instrument. FTG-Specific Line correction is the next process used to calculate the tensor components from the GGI in-line and cross signals and to remove bulk low-frequency errors. This process assumes that there is no correlation between the error we want to remove and the signal that we want to keep. Since some small mis-ties at the intersection of survey lines still remain due to random noise content and no-specific linear errors, in the final line leveling procedure, a Butterworth filter between 0.5 and 1 kilometer in length is applied and the mis-ties are calculated at every intersection. The mis-ties in the filtered data are analyzed on a line by line basis and the adjustments calculated from the filtered data are also applied to the unfiltered data. This process is completed in several passes, each time re-calculating mis-ties, and applying a higher order fit to the data until mis-ties are very near zero. This procedure finally produces mis-ties adjusted, unfiltered data. The final step is a noise reduction based on the Laplacian relationship among the in-line tensor components. FTG provides the six components of the gravity gradient tensor. Subtracting the normal gradient tensor from the gravity gradient tensor collected by FTG, we obtain a free-air gradient tensor and these free-air gradients will be used to compare the gradients modeled from gravity anomaly and terrain data in the following section.

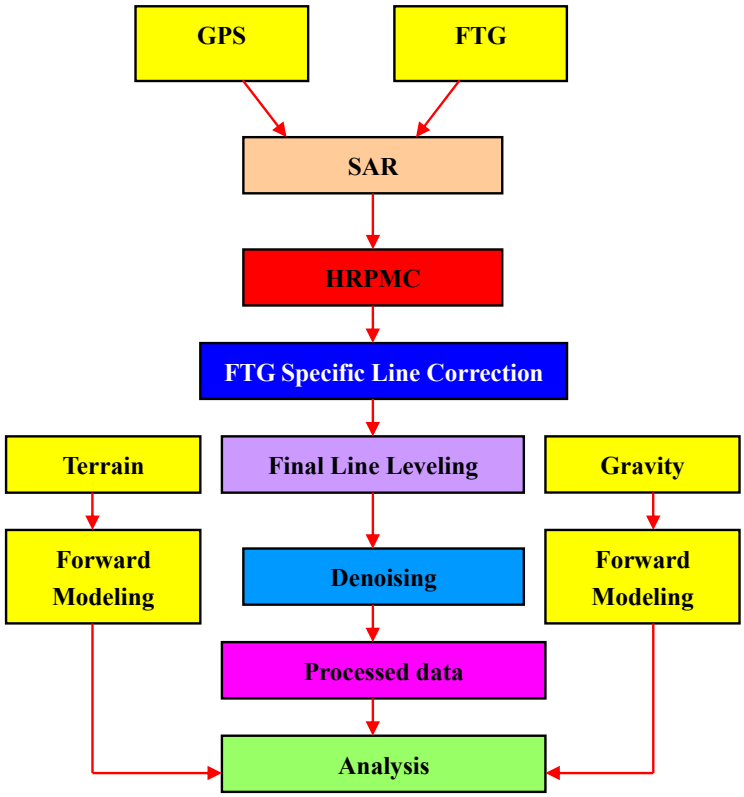

Figure 4.3: Flowchart of modeling gradient

4.3.3 Crossover point analysis

From the FTG data, we have 490 potential crossover points that can be used to determine the internal accuracy of the FTG data. For both principal and tie line profiles, there are no exact crossover points with the same horizontal coordinates and altitude. The sampling rate of the FTG data is 1 record per second, which corresponds to about 60 m sampling interval along the profile. First by comparing the horizontal coordinates from principal and tie line data, we found 490 point pairs whose horizontal separation are less than 36.05 m. These point pairs have similar horizontal coordinates, but not altitude. So we need to compensate the difference of the gradient signal due to the different surveying altitudes. Since most of gradient signal is likely due to the mass of the terrain, we use a DEM to compute the gradients for different altitudes, and then we use the difference between altitudes to compensate the gradients at each pair of crossover points. Suppose $P_1(x_1, y_1, z_1)$ and $P_2(x_2, y_2, z_2)$ are a pair of crossover points, where the gradient

measurements are $\delta\Gamma_{jk}(P_1)$ and $\delta\Gamma_{jk}(P_2)$. Taking account of the small difference in the horizontal coordinates between P_1 and P_2, we separately compute the gradients due to a DEM at P_1 and P_2, and denote them as $\delta\Gamma_{jk}(P_1)\big|_{DEM}$ and $\delta\Gamma_{jk}(P_2)\big|_{DEM}$. We use their difference,

$$\Delta\delta\Gamma_{jk}(P_1,P_2)=\delta\Gamma_{jk}(P_1)\big|_{DEM}-\delta\Gamma_{jk}(P_2)\big|_{DEM}, \tag{4.15}$$

as a compensation to correct $\delta\Gamma_{jk}(P_2)$ from P_2 to P_1. Finally we get the gradient disturbance error on the crossover point,

$$\Delta\delta\Gamma_{jk}(P_1)=\delta\Gamma_{jk}(P_1)-\delta\Gamma_{jk}(P_2)-\Delta\delta\Gamma_{jk}(P_1,P_2) \tag{4.16}$$

Applying this procedure at 490 crossover points, we obtain the results shown in Figure 4.4. Table 4.2 gives the statistics of Figure 4.4. It shows that the mean value is less than 0.2 E except for $\Delta\Gamma_{23}$ (-0.8 E) and the FTG data has a standard deviation of ±8 E which could be a measure of the precision of FTG data.

Table 4.2: Statistics of the crossover points (units: E)

Statistics	$\Delta\delta\Gamma_{11}$	$\Delta\delta\Gamma_{12}$	$\Delta\delta\Gamma_{13}$	$\Delta\delta\Gamma_{22}$	$\Delta\delta\Gamma_{23}$	$\Delta\delta\Gamma_{33}$
Mean	0.2	0.1	0.0	0.0	-0.8	-0.2
Std	8.1	6.1	6.9	6.1	6.3	6.8
Min	-27.9	-30.4	-26.1	-26.0	-22.6	-25.0
Max	36.8	20.1	21.2	19.2	24.7	18.0

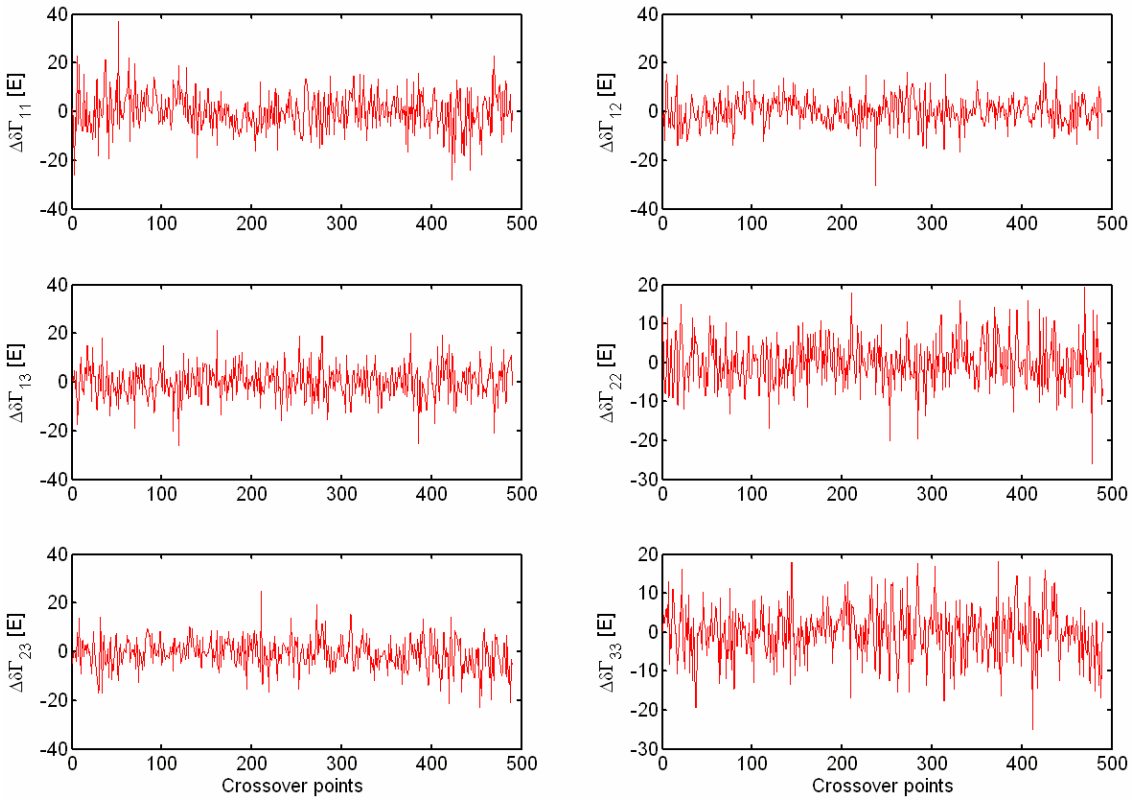

Figure 4.4: Crossover point error

4.4 Gravity gradient model

4.4.1 Gravity and DEM data in Parkfield

In order to compare the modeled gradients with the FTG data, we obtained gravity data and DEM data in the Parkfield, CA area. A total set of 3037 free-air gravity anomalies (Figure 4.5) was obtained from NGA. The anomalies are approximately evenly scattered in most of this area (latitude: 35.5° ~ 36.5° degree, longitude: -120° ~ -121°), except for the northern part. The resolution of these gravity data is approximately 1 arcmin, and the accuracy of the gravity anomalies is given as 3 mGal. For a further processing, the anomalies are interpolated onto a 1'×1' grid using kriging. From the free air anomaly data (the left part of Figure 4.6), we removed the EGM96 effect and made terrain corrections to get the residual gravity anomaly (the right part of Figure 4.6).

The terrain correction is computed according to (4.3) on the basis of 1"×1" DEM data (Figure 4.7) in this area. These data are a product of the Shuttle Radar Topography Mission (SRTM) conducted by NGA and NASA. USGS distributes the data under an agreement with NGA and NASA. The DEM data obtained from USGS are given at

intervals of 1 arcsec in latitude and longitude. It is horizontally and vertically referenced to the WGS84/EGM96 geoid. The physical statistics of these gravity anomaly and DEM data are given in Table 4.3. From this table, the terrain corrections are very smooth with the standard deviation of 2.9 mGal. The effects of EGM96 on the gravity anomaly are smooth in this area with the standard deviation of 19.7 mGal. The residual anomalies obtained by adding terrain corrections and removing the EGM96 effect, have a smaller standard deviation than the free-air or Faye anomaly data. The elevation of the topography varies between 0 and 1597.0 m in this area, and its mean and standard deviation are 441.2 m and 264.4 m respectively.

Table 4.3: The statistics of gravity anomaly and DEM in Parkfield (unit: mGal)

Statistics	Mean	Std. Dev	RMS	Min	Max
Free-air Anomaly (mGal)	-6.9	29.6	30.4	-62.8	95.5
Faye Anomaly (mGal)	-4.9	31.0	31.4	-62.5	104.6
Terrain correction (mGal)	2.0	2.9	3.5	0.1	31.8
EGM96 (mGal)	-1.5	17.6	17.7	-33.3	31.1
Residual Anomaly (mGal)	-3.4	29.0	29.2	-62.7	119.1
Terrain (m)	441.2	264.3	514.3	0	1597.0

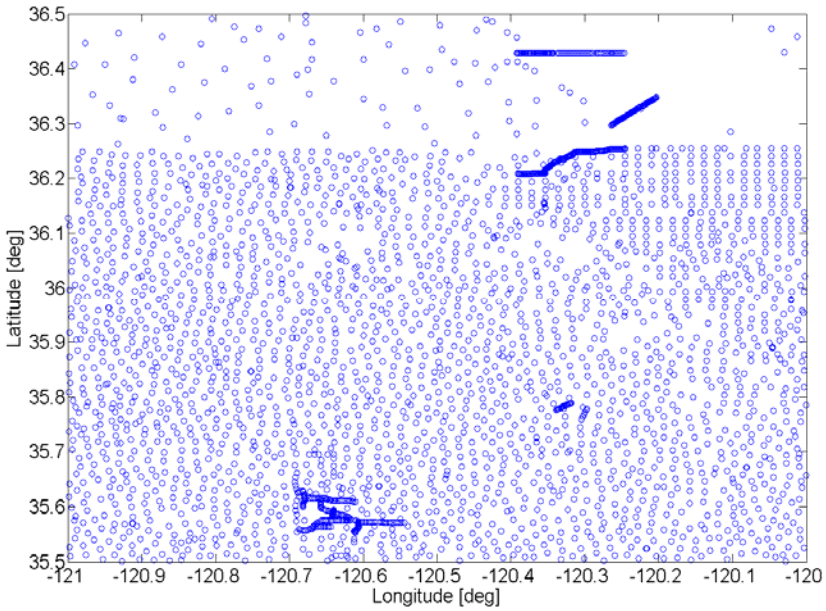

Figure 4.5: Gravity distribution in the Parkfield, CA, area

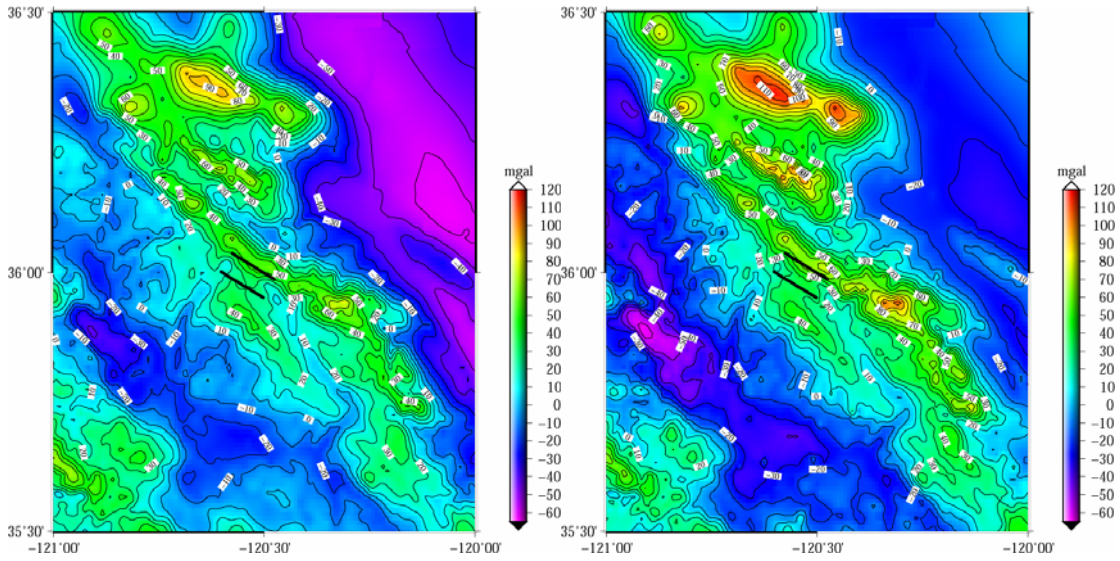

Figure 4.6: Gravity data in the Parkfield, CA, area (left: Free air gravity anomaly; right: residual gravity anomaly (free-air anomaly data corrected by EGM96, terrain corrections))

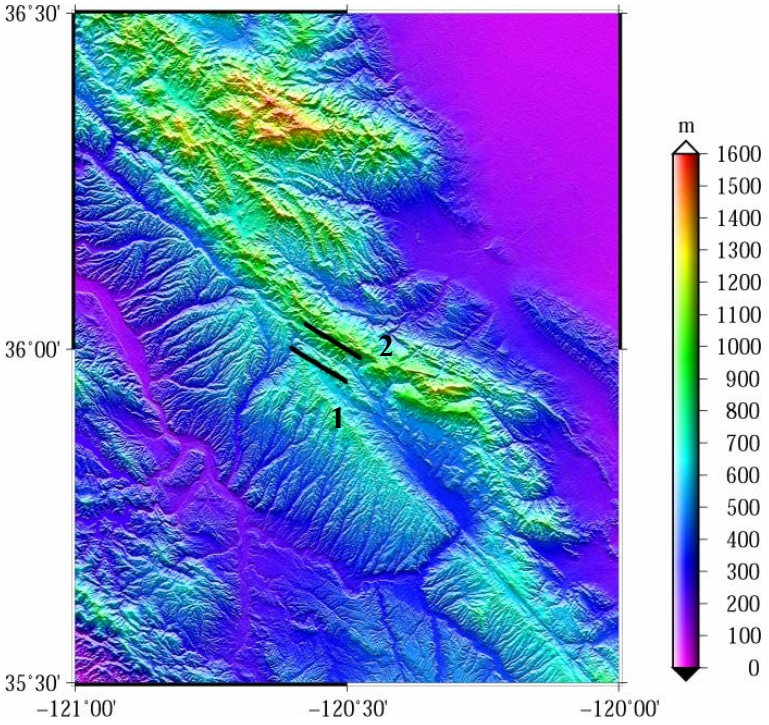

Figure 4.7: DEM of the Parkfield, CA, area (2 black lines: test profiles)

4.4.2 Gravity gradient modeling in the Parkfield area

To illustrate the gradient modeling techniques from DEM and gravity anomalies, we compute the gradient disturbances from EGM96, and from gravity anomalies and DEM data along the test profiles (2 black lines in Figure 4.7) over San Andrea fault. These two lines are actual FTG profiles, and each is about 10 km long, and 400 m above the terrain. Profile 1 has 150 records with a sampling interval of about 70 m. Profile 2 has 166 records with a sampling interval of about 64 m. Modeled gradient disturbances shown in Figure 4.10 were constructed by consistently combining boundary-value problem solutions (Stokes' integral and spherical harmonic expansions) with Newton's density integral for the layer and DEM effect according to (4.8) and (4.10). Gravitational gradients modeled from EGM96 are almost constant at these profiles, because the resolution of EGM96 is 50 km, and much larger than the length of these profiles.

High resolution (30 m) topography was used in forward modeling the terrain effect and the Helmert condensation layer under the assumption of constant crust density. Since the layer effect always contributes the longer wavelengths to the gradients than the DEM effect, the whole $1^\circ \times 1^\circ$ DEM is used to compute the layer effect and a local DEM (longitude: $-120^\circ 41'53'' \sim -120^\circ 25'30''$; latitude: $35^\circ 52'28'' \sim 36^\circ 04'38''$), about $24\text{km} \times 24\text{km}$, was chosen to compute the gradients due to the topographic mass. Bell Geospace also provides the terrain effects (gradients due to topographic mass) for FTG data. According to their report (Bell Geospace, 2004), the terrain effects are computed from SRTM data in the area (longitude: $-120^\circ 40' \sim -120^\circ 27'$; latitude: $35^\circ 54' \sim 36^\circ 03'$). Figure 4.8 shows that both our computed terrain effects and Bell Geospace's on Profile 2 are comparable. The rms of their differences is less 3 E for all gradient components. In the following step, we use our results to model terrain effects.

From Figure 4.9, the gradient signal derived from the residual gravity anomalies is much smoother than DEM-derived signal and reflects the density anomalies below the geoid. The layer effect is actually the low frequency part of the DEM-derived signal since it is the condensation of DEM effect. The DEM-derived gradients have higher variable magnitude than other components, and contribute most of the energy of the gradients.

From the 61×61 residual gravity anomalies in the test area, we used Stokes' integral, the radial-basis spline method and least-squares collocation, respectively, to derive $\delta\Gamma_{jk}^{st}\big|_{residual}$, $\delta\Gamma_{jk}^{sp}\big|_{residual}$ and $\delta\Gamma_{jk}^{LSC}\big|_{residual}$. Thus, we obtain three different modeled gradient disturbances (where the terrain and EGM96 effects are the same in each case), and define them as $\delta\Gamma_{jk}^{st}$, $\delta\Gamma_{jk}^{sp}$ and $\delta\Gamma_{jk}^{LSC}$.

In the case of Stokes' integral method the residual gravity anomaly data were used to compute the residual gradient disturbances according to (3.25) on the corresponding points of the FTG profile. The kernel values are evaluated on the grid points according to (3.27).

For the spherical spline method, first the parameters, $k = 2$, and $\psi = 5'$ were chosen to compute the series, A_l, according to (3.43). Second, the kernel values in terms of the spherical distance were computed at an interval of 1 arcsec according to (3.48). The kernel values for each pair of points in (3.49) were interpolated from these. Third, the $61 \times 61 = 3721$ coefficients were solved according to (3.50), where the matrix inverse was

obtained by the method of singular-value decomposition (Xu, 1998). Figure 4.10 presents the eigenvalues of the matrix. All eigenvalues below 4×10^{-7} are discarded. With the solution of coefficients, we used (3.54) to derive the gradient disturbances.

For least-squares collocation (LSC), we used the GRAVSOFT computer software (Tscherning et al., 1992) to compute the gradients with the covariance model parameters: $l_{\min}=181$, $A_0=1074 mGal^2$ and $R_b=R-200m$ which were estimated from the empirical covariance using the COVFIT program. Since the accuracy of the gravity anomalies is 3 mGal, we used a value of 9 $mGal^2$ as the variance of the observation noise.

Figures 4.11 and 4.12 show that the FTG data as well as the modeled gradient disturbances due to the residual gravity anomalies, terrain effects, and EGM96, along the two survey test profiles. The residual gravity anomalies were processed by the Stokes' integral, radial-basis spline and least-squares collocation methods. Tables 4.4 and 4.5 give the statistics for the differences between modeled gradient disturbances and the FTG data respectively. On Profile 1, the standard deviations of $\Delta\delta\Gamma_{12}^{st}$, $\Delta\delta\Gamma_{23}^{st}$ and $\Delta\delta\Gamma_{33}^{st}$ are between 8.1 E and 12.6 E, and the standard deviations of $\Delta\delta\Gamma_{11}^{st}$, $\Delta\delta\Gamma_{13}^{st}$ and $\Delta\delta\Gamma_{22}^{st}$ are between 17.5 E and 20.8 E. The standard deviation of $\Delta\delta\Gamma_{jk}^{st}$ agrees with $\Delta\delta\Gamma_{jk}^{LSC}$. The standard deviation of $\Delta\delta\Gamma_{12}^{sp}$ is 8.7 E, which agrees with $\Delta\delta\Gamma_{12}^{st}$ and $\Delta\delta\Gamma_{12}^{LSC}$, but the standard deviations of $\Delta\delta\Gamma_{23}^{sp}$ and $\Delta\delta\Gamma_{33}^{sp}$ are 25.3 E and 15.0 E, which are bigger than $\Delta\delta\Gamma_{23}^{st}$ and $\Delta\delta\Gamma_{33}^{st}$, $\Delta\delta\Gamma_{23}^{LSC}$ and $\Delta\delta\Gamma_{33}^{LSC}$, respectively. On Profile 2, the standard deviations of $\Delta\delta\Gamma_{jk}^{st}$ (off-diagonal components) are between 7.8 E and 10.0 E, which agree with $\Delta\delta\Gamma_{jk}^{sp}$, and $\Delta\delta\Gamma_{jk}^{LSC}$ as well; the standard deviations of $\Delta\delta\Gamma_{jj}^{st}$ (diagonal components) are between 12.5 E and 17.6 E, which agree with $\Delta\delta\Gamma_{jj}^{sp}$, and $\Delta\delta\Gamma_{jj}^{LSC}$ as well. The standard deviation of $\Delta\delta\Gamma_{11}^{st}$ is less than that of $\Delta\delta\Gamma_{11}^{sp}$ and $\Delta\delta\Gamma_{11}^{LSC}$. The standard deviation of $\Delta\delta\Gamma_{33}^{st}$ is 12.8 E, which is same as $\Delta\delta\Gamma_{33}^{LSC}$, and a little bigger than $\Delta\delta\Gamma_{33}^{sp}$. Generally, for Profile 1, $\Delta\delta\Gamma_{12}$ has a smaller standard deviation (about 8 E) for the three models.

In general, the standard deviations of the differences between the modeled gradients and the real FTG data are very large. The standard deviation for the off-diagonal gradient is about 9 E, better than the diagonal gradient. Stokes' integral and the least-squares collocation methods are at the same level of agreement with respect to the FTG data, and yield slightly better agreement than the radial-basis spline method. The off-diagonal gradients are less sensitive to the range of DEM used in modeling gradients than the diagonal gradients. Since the agreement in off-diagonal components between the FTG data and modeled gradient disturbances is better than in diagonal components, we concluded that the terrain effect used here is not a best match for this modeling case.

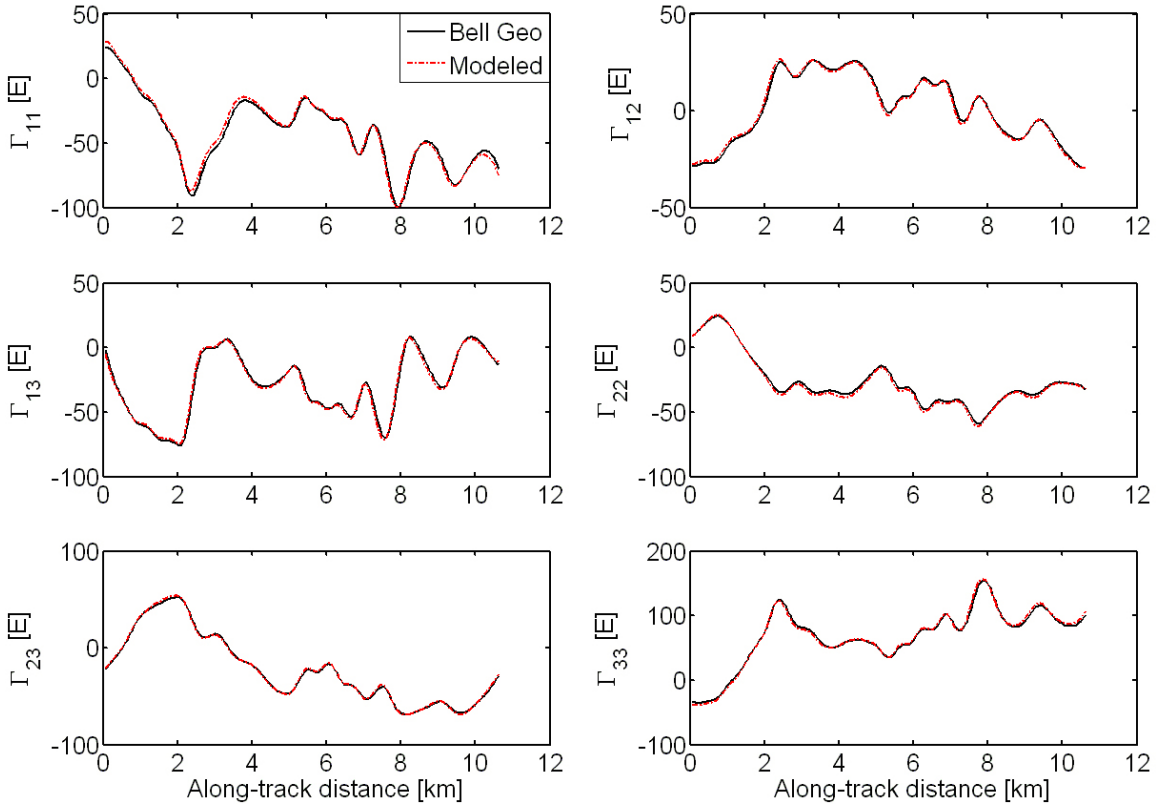

Figure 4.8 Terrain effect modeled using our chosen DEM vs. Bell Geospace's terrain effect on Profile 2

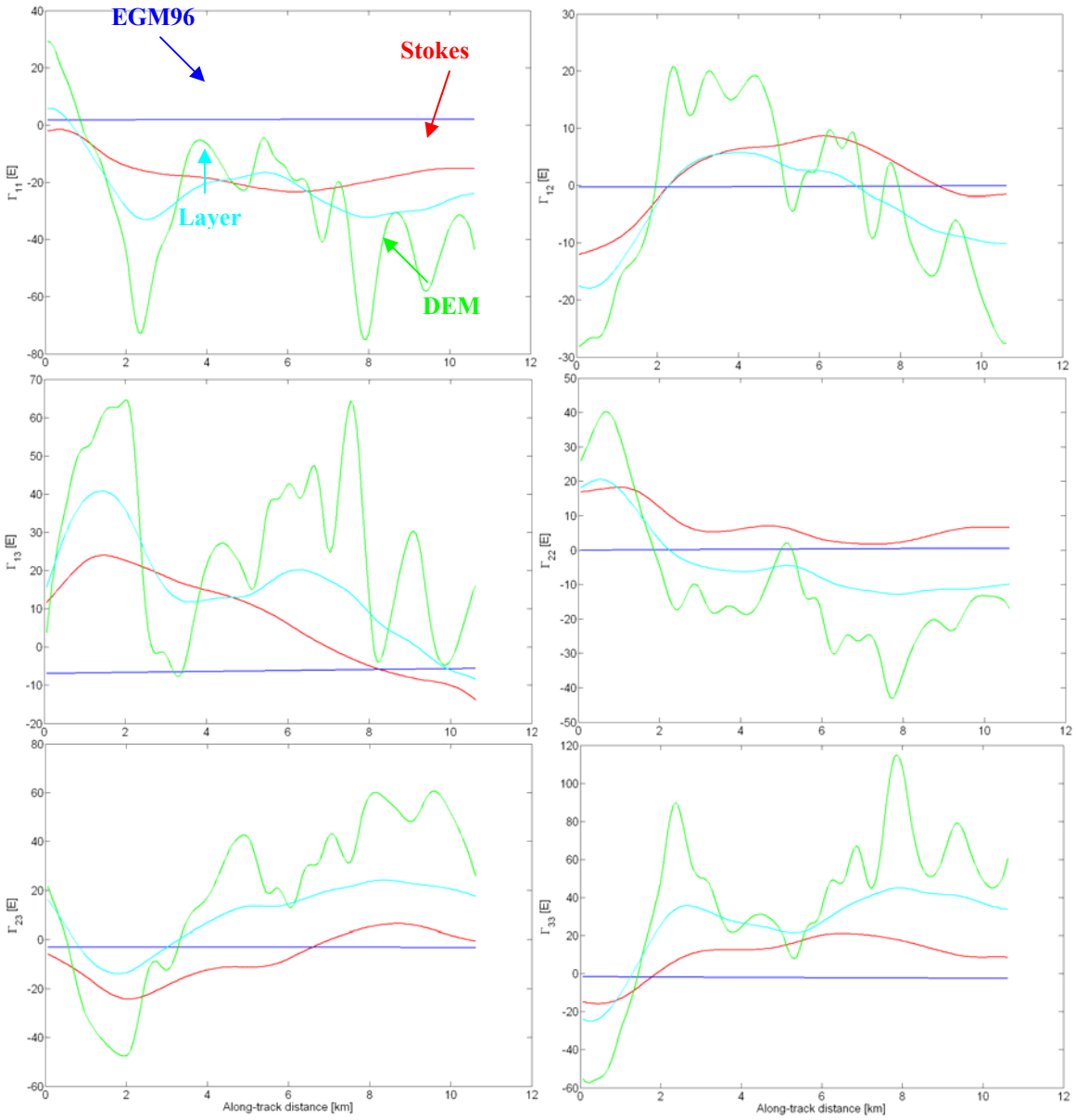

Figure 4.9: The gradient disturbances due to the residual gravity anomalies, DEM effect, layer effect and EGM96 (64m resolution along survey Profile 2)

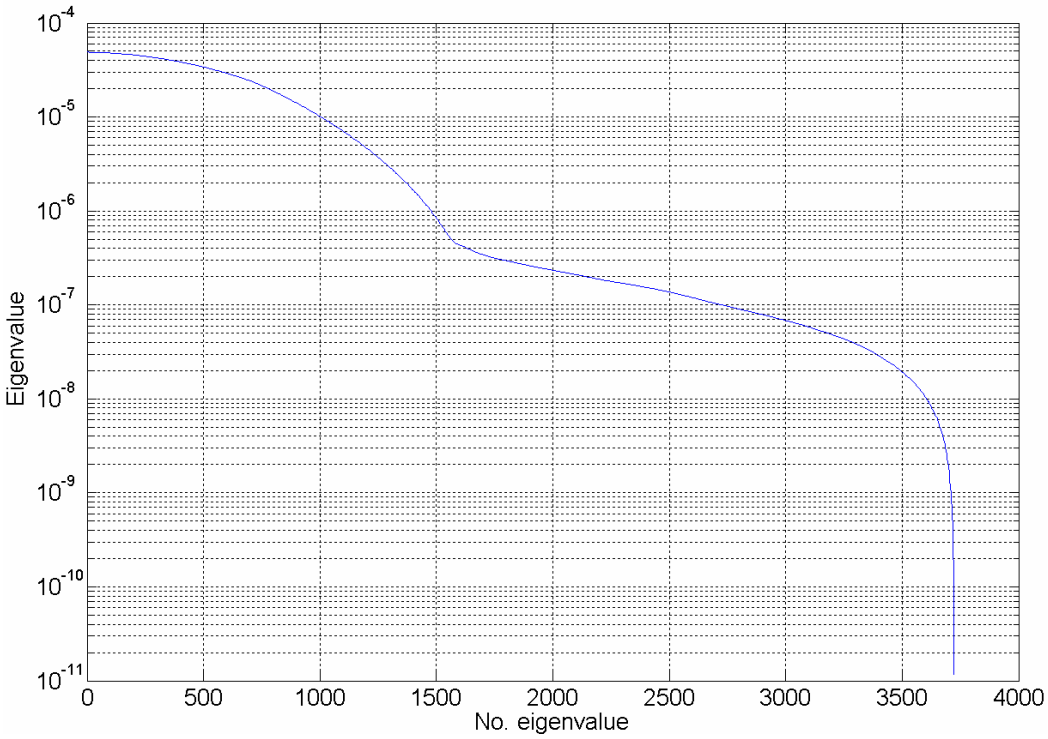

Figure 4.10 Eigenvalues of the kernel matrix in the radial-basis spline method

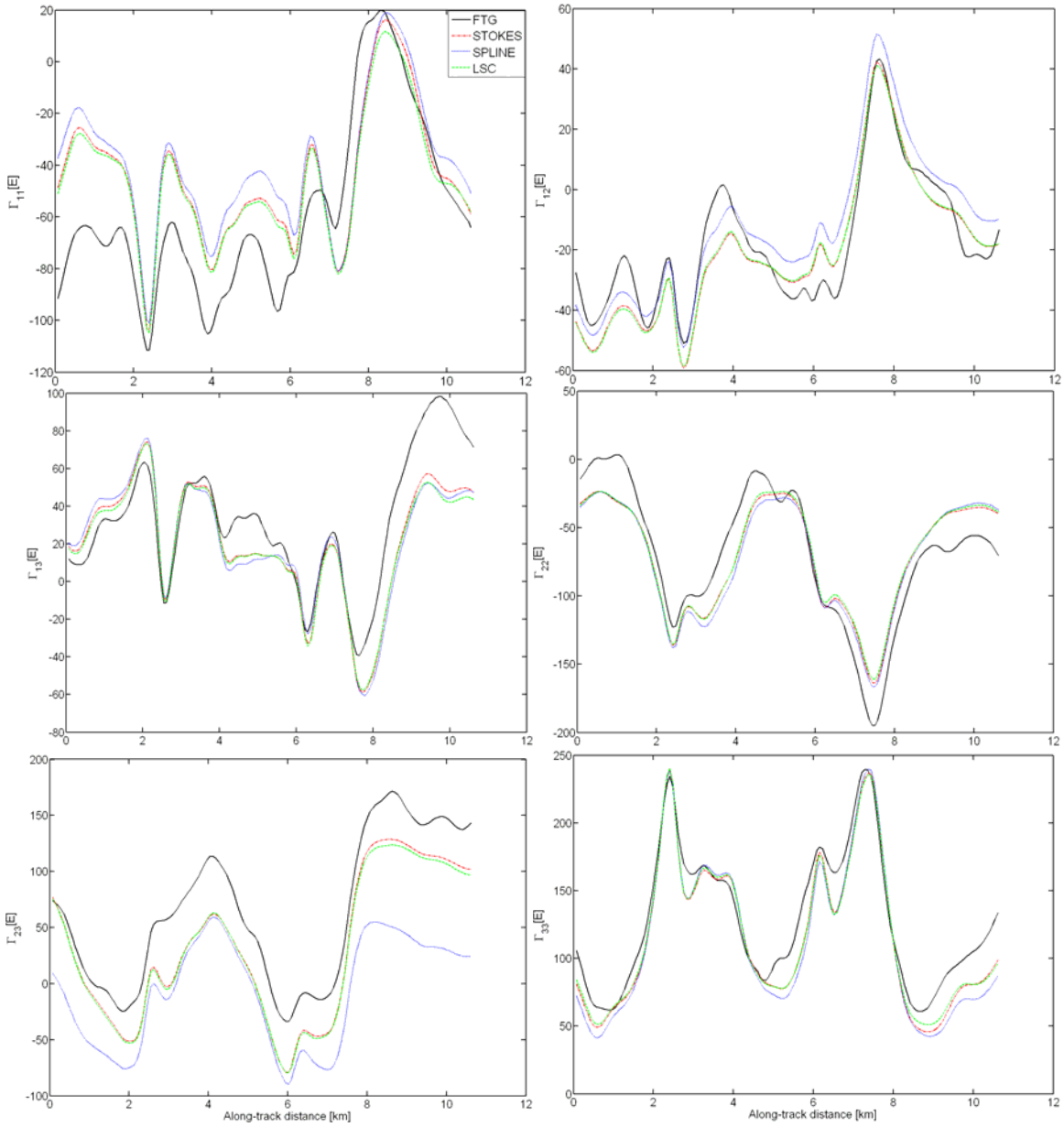

Figure 4.11: Plots of FTG data and gradients derived from Stokes' integral, spherical spline and least-squares collocation methods on survey Profile 1.

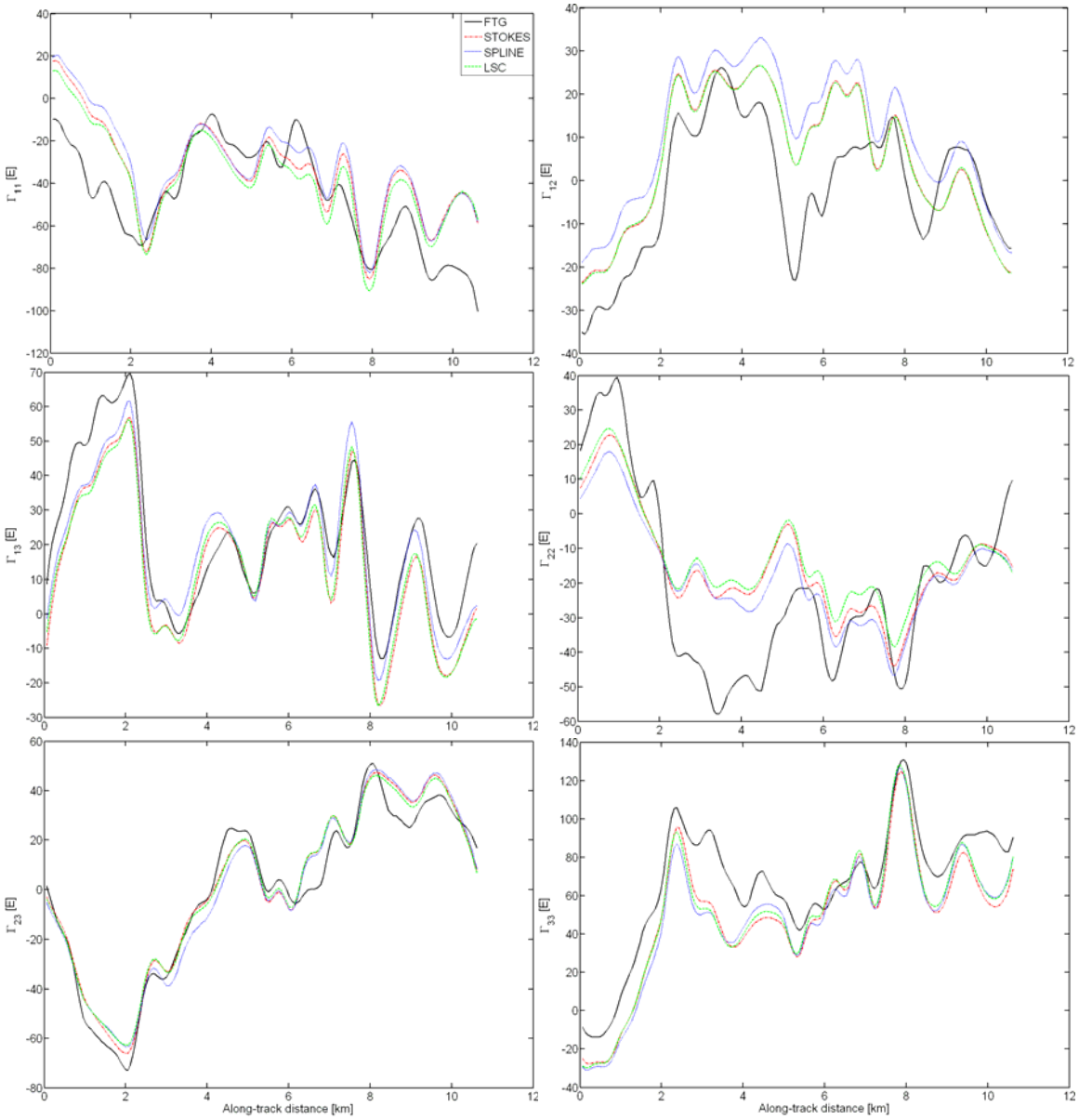

Figure 4.12: Plots of FTG data and gradients derived from Stokes' integral, spherical spline and least-squares collocation methods on survey Profile 2.

Table 4.4: Statistics of the differences between modeled gradient disturbances and FTG data on survey Profile 1 (unit: E)

Statistics	$\Delta\delta\Gamma_{11}^{st}$	$\Delta\delta\Gamma_{12}^{st}$	$\Delta\delta\Gamma_{13}^{st}$	$\Delta\delta\Gamma_{22}^{st}$	$\Delta\delta\Gamma_{23}^{st}$	$\Delta\delta\Gamma_{33}^{st}$
Mean	13.3	-2.5	-10.4	-1.0	-33.9	-12.3
Std	18.8	8.1	17.5	20.8	12.6	11.7
Min	-37.4	-20.7	-48.0	-35.0	-60.3	-35.0
Max	42.9	13.7	15.4	31.4	2.8	10.3
	$\Delta\delta\Gamma_{11}^{sp}$	$\Delta\delta\Gamma_{12}^{sp}$	$\Delta\delta\Gamma_{13}^{sp}$	$\Delta\delta\Gamma_{22}^{sp}$	$\Delta\delta\Gamma_{23}^{sp}$	$\Delta\delta\Gamma_{33}^{sp}$
Mean	18.4	4.8	-10.8	-2.8	-71.7	-15.5
Std	20.6	8.7	20.4	22.1	25.3	15.0
Min	-37.3	-12.2	-51.8	-40.4	-121.5	-46.3
Max	54.2	20.8	19.3	33.5	-38.7	11.5
	$\Delta\delta\Gamma_{11}^{LSC}$	$\Delta\delta\Gamma_{12}^{LSC}$	$\Delta\delta\Gamma_{13}^{LSC}$	$\Delta\delta\Gamma_{22}^{LSC}$	$\Delta\delta\Gamma_{23}^{LSC}$	$\Delta\delta\Gamma_{33}^{LSC}$
Mean	11.5	-2.6	-11.8	0.0	-35.9	-11.5
Std	19.3	8.1	18.2	21.4	12.5	11.6
Min	-39.5	-20.0	-53.7	-34.4	-62.5	-37.2
Max	40.6	14.4	14.5	34.3	1.5	10.3

Table 4.5: Statistics of the differences between modeled gradient disturbances and FTG data on survey Profile 2 (unit: E)

Statistics	$\Delta\delta\Gamma_{11}^{st}$	$\Delta\delta\Gamma_{12}^{st}$	$\Delta\delta\Gamma_{13}^{st}$	$\Delta\delta\Gamma_{22}^{st}$	$\Delta\delta\Gamma_{23}^{st}$	$\Delta\delta\Gamma_{33}^{st}$
Mean	11.3	6.6	-7.5	4.4	2.2	-15.7
Std	17.0	10.0	8.9	15.7	7.9	12.8
Min	-37.9	-16.6	-26.2	-29.9	-15.1	-47.5
Max	47.9	30.7	12.4	35.5	25.5	13.6
	$\Delta\delta\Gamma_{11}^{sp}$	$\Delta\delta\Gamma_{12}^{sp}$	$\Delta\delta\Gamma_{13}^{sp}$	$\Delta\delta\Gamma_{22}^{sp}$	$\Delta\delta\Gamma_{23}^{sp}$	$\Delta\delta\Gamma_{33}^{sp}$
Mean	14.5	12.2	-3.1	1.8	1.2	-16.4
Std	17.2	9.8	8.8	16.0	8.6	12.5
Min	-30.2	-9.9	-18.8	-34.8	-19.2	-50.1
Max	53.9	35.8	17.8	35.1	24.3	9.6
	$\Delta\delta\Gamma_{11}^{LSC}$	$\Delta\delta\Gamma_{12}^{LSC}$	$\Delta\delta\Gamma_{13}^{LSC}$	$\Delta\delta\Gamma_{22}^{LSC}$	$\Delta\delta\Gamma_{23}^{LSC}$	$\Delta\delta\Gamma_{33}^{LSC}$
Mean	7.9	6.5	-7.7	6.7	2.1	-14.7
Std	17.6	9.9	9.1	16.0	7.8	12.8
Min	-42.3	-16.4	-25.5	-31.6	-15.5	-48.4
Max	44.5	30.3	12.9	38.5	25.5	14.0

In order to assess just the boundary-value method of modeling the gradient disturbances, we compared them to the terrain-corrected gradients rather than the free-air gradient provided by Bell Geospace. As before, the free-air gravity anomalies in the Parkfield area were reduced to Faye anomalies (removing the terrain and adding an equivalent density layer on the geoid). Subsequently, only the effect of the DEM was removed from the modeled gradient disturbances because Bell Geospace's terrain corrected gradients also only removed the terrain effect. Figure 4.13 compares the modeled gradients using Stokes' integral with the FTG terrain-corrected gradients on Profile 2. Similar results were obtained for Profile 1. The modeled gradients are much smoother than the terrain-corrected FTG data.

Figure 4.14 gives the power spectral densities (PSDs) of both the terrain-corrected FTG data and the modeled gradients. The modeled gradients have a lower PSD curve than the FTG data, which has more variation in the frequency band of 1~2 cy/km. For the higher frequency beyond 2 cy/km, the modeled $\delta\Gamma_{33}$ agrees with the FTG data, but the other components still have some differences. Clearly, the differences between the FTG data and the modeled gradient disturbances are much larger than the differences among models obtained with the simulation described in Chapter 3. It should be noted, however, that the smoothness of the gravity anomaly-implied gradient disturbances is due to their much lower resolution (1 arcmin ≈ 2 km) compared to the FTG data (64 m). Since the terrain-corrected FTG data should also be smooth, this comparison between the FTG data and modeled gradients indicates the accuracy of the FTG data is between 10 E -20 E.

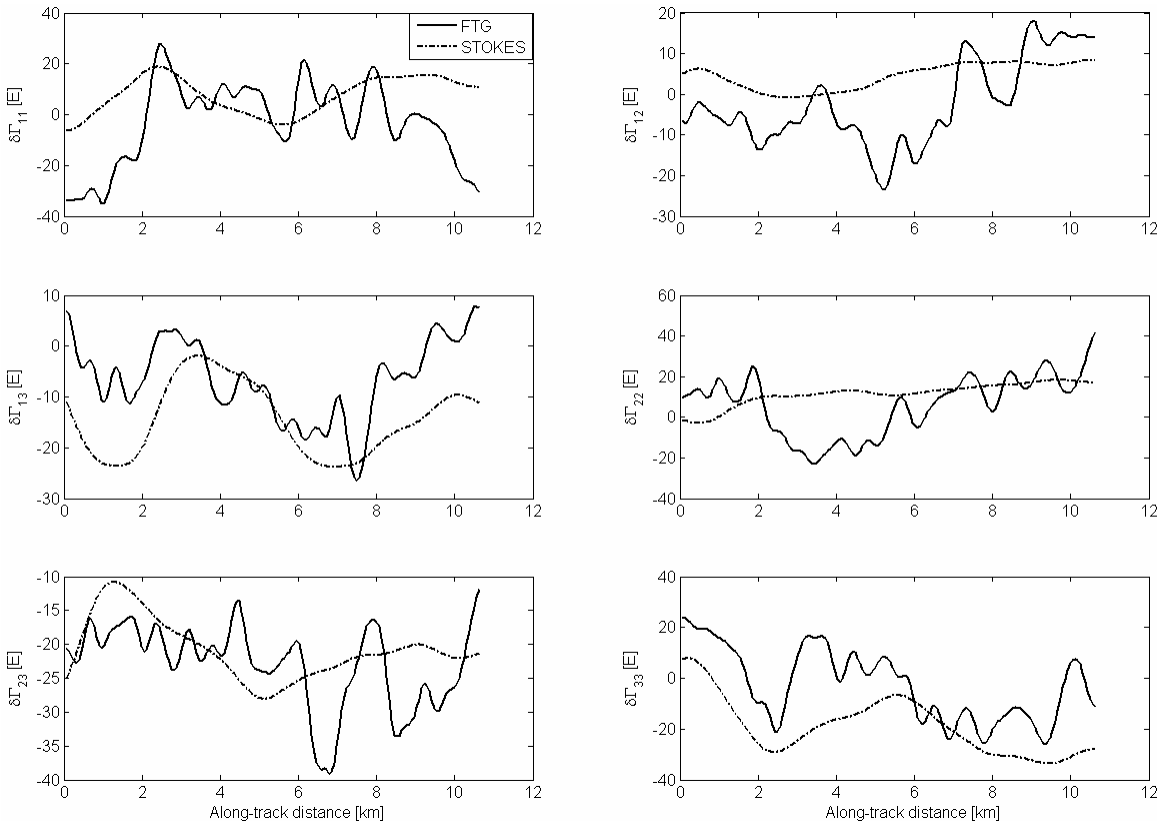

Figure 4.13: Terrain corrected FTG data and modeled gradient disturbances (without DEM effect) by Stokes' integral method on Profile 2.

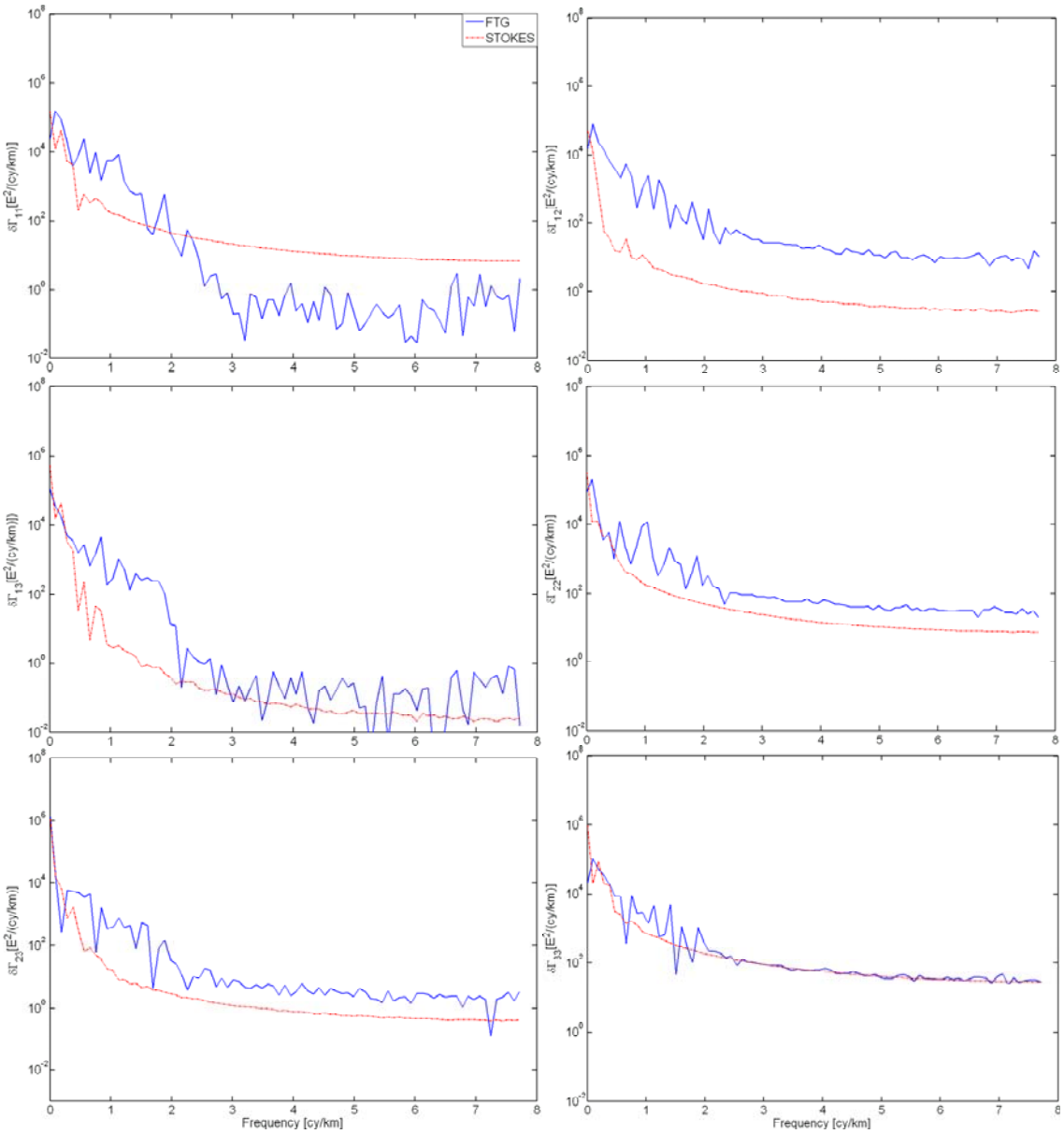

Figure 4.14: The PSD of terrain corrected FTG data and modeled gradient disturbances (without DEM effect) by Stokes' integral method on Profile 2.

4.5 Reference surface for gravity anomalies

In the modeling of gradients using a DEM, a mean topographic surface could be chosen instead of the geoid, as considered in Section 2.3.4. Similarly, we may use an alternative reference surface in the corresponding gravity reduction procedure.

We start with the free air anomaly (Heiskanen and Moritz, 1967),

$$\Delta g_f = g - \left(\frac{\partial \gamma}{\partial h}\right) h - \left(\frac{1}{2}\right)\left(\frac{\partial^2 \gamma}{\partial h^2}\right) h^2 - \gamma_0 + \delta g_A , \tag{4.17}$$

where g is gravity observed on the Earth's surface, γ_0 is the normal gravity on the ellipsoid, δg_A is the effect of atmosphere, and h is the normal height (usually the elevation of station above the mean sea surface is used and is assumed equal to the normal height). The second, third and fourth terms together yield the normal gravity on the telluroid. The telluroid is defined as that surface where the potential of normal gravity is equal to the actual gravity potential on the Earth's surface.

If we set the reference surface as the mean topographical surface (elevation is H) instead of the geoid, all quantities need to be reduced to that surface. Gravity can be downward continued to that surface according to

$$g_r = g - \left(\frac{\partial g}{\partial h}\right)(h - H) - \left(\frac{1}{2}\right)\left(\frac{\partial^2 g}{\partial h^2}\right)(h - H)^2 . \tag{4.18}$$

Assume there is a corresponding surface (co-telluroid) similar to the telluroid where the normal potential is equal to the actual potential on the reference surface. Then the difference between gravity on the reference surface and the normal gravity on the co-telluroid is given by

$$\Delta g_f^{'} = g_r - \left(\frac{\partial \gamma}{\partial h}\right) H - \left(\frac{1}{2}\right)\left(\frac{\partial^2 \gamma}{\partial h^2}\right) H^2 - \gamma_0 + \delta g_A . \tag{4.19}$$

Approximating $\frac{\partial g}{\partial h}$ with $\frac{\partial \gamma}{\partial h}$, $\frac{\partial^2 g}{\partial h^2}$ and $\frac{\partial^2 \gamma}{\partial h^2}$, we get

$$\Delta g_f^{'} = \Delta g_f + \left(\frac{\partial^2 \gamma}{\partial h^2}\right) H(h - H) , \tag{4.20}$$

$$\frac{\partial^2 \gamma}{\partial h^2} = 1.45 \times 10^{-12}\ m^{-1} s^{-2} , \tag{4.21}$$

and assuming $H = 1000$ m, and $h - H \approx 2000$ m, the difference between $\Delta g_f^{'}$ and Δg_f is about 0.3 mGal. This value can be neglected since it is smaller than the observation error (1mGal).

After choosing the mean elevation as reference surface, all reductions refer to this surface. Clearly, the gravity anomalies do not change under the second Helmert condensation scheme. They are still Faye anomalies (Free air anomalies + terrain correction). The only difference in the actual process is that the height of Bouguer plate is changed from h to h-H. The terrain correction is the same. The change in the final gradient is due to the change of density of the layer from ρh to $\rho(h - H)$. Also all

gradients due to the terrain are generated from a residual DEM model. Finally, the altitude of upward continuation is relative to the mean elevation surface.

Figure 4.15 presents FTG data and modeled gradient disturbances using the geoid and a mean elevation of 500 m as reference surface. It shows that there is better agreement with the geoid as reference. We denote modeled gradient disturbances using the geoid and 500 m mean elevation surface as reference as $\delta\Gamma_{jk}^{geoid}$ and $\delta\Gamma_{jk}^{500m}$ and denote the FTG data as $\delta\Gamma_{jk}^{FTG}$. Their power spectral densities (PSDs) on Profile 2 are shown in Figure 4.16 where $\delta\Gamma_{11}^{geoid}$, $\delta\Gamma_{13}^{geoid}$, and $\delta\Gamma_{33}^{geoid}$ agree with the PSD of the FTG data at the higher frequency(beyond 2 cy/km). $\delta\Gamma_{jk}^{geoid}$ only agrees with $\delta\Gamma_{jk}^{500m}$ at the intermediate frequency (1-2 cy/km) except for $\delta\Gamma_{22}$ and differs from $\delta\Gamma_{jk}^{500m}$ at the higher frequency. Generally, the layer effect on the gradients is increasing, and the topographic effect is decreasing with an increase in the altitude of reference surface. Due to the decrease in upward continuation altitude, gravity-derived gradients increase in magnitude. Figure 4.17 compares the contributions to the modeled gradient disturbances using the reference surface at 500 m mean elevation and the geoid. The gravity-derived component (Stokes' integral) has higher magnitude using 500m as reference surface than using the geoid because the relative distance between the computation point at the altitude and the reference surface decreases (and, as stated, the gravity anomalies have not changed). The difference is about 10~20 E. Similarly, the gradients due to the layer increase by about 20~30 E when it is on the 500 m reference surface rather than on the geoid. Though the layer density decreases about 1/3, the change of relative distance has greater impact on gradients than the density change. The change in DEM-derived gradients falls into two categories: the in-line gradients and the cross gradients. There is a little change in the cross gradients, but a large change for the in-line gradients of about 20 E. Figure 4.18 presents the power spectral densities of the modeled gradient components and the FTG data. We denote these components as $\delta\Gamma_{jk}\big|_{gravity}$, $\delta\Gamma_{jk}\big|_{layer}$ and $\delta\Gamma_{jk}\big|_{DEM}$. Generally, gravity-derived gradients and the layer effects have higher energy at high frequencies when the reference surface is at 500 m than at the geoid. The PSD of $\delta\Gamma_{jj}^{geoid}\big|_{DEM}$ (in-line gradients) agrees with $\delta\Gamma_{jj}^{500m}\big|_{DEM}$ at the frequency higher than 0.5 cy/km, but differs at the frequency lower than 0.5 cy/km. The PSD of $\delta\Gamma_{jk}^{geoid}\big|_{DEM}$ (cross gradients) agrees with $\delta\Gamma_{jk}^{500m}\big|_{DEM}$ at the frequency lower than 2 cy/km, and differs at the frequency higher than 2 cy/km, especially in $\delta\Gamma_{12}\big|_{DEM}$ and $\delta\Gamma_{23}\big|_{DEM}$.

The study on choosing a reference surface shows that a 500 m mean elevation surface yields worth results with respect to the FTG data than if the reference is the geoid. This is due to the amplifying layer effect on gradients and the decreasing topographic effects on gradients.

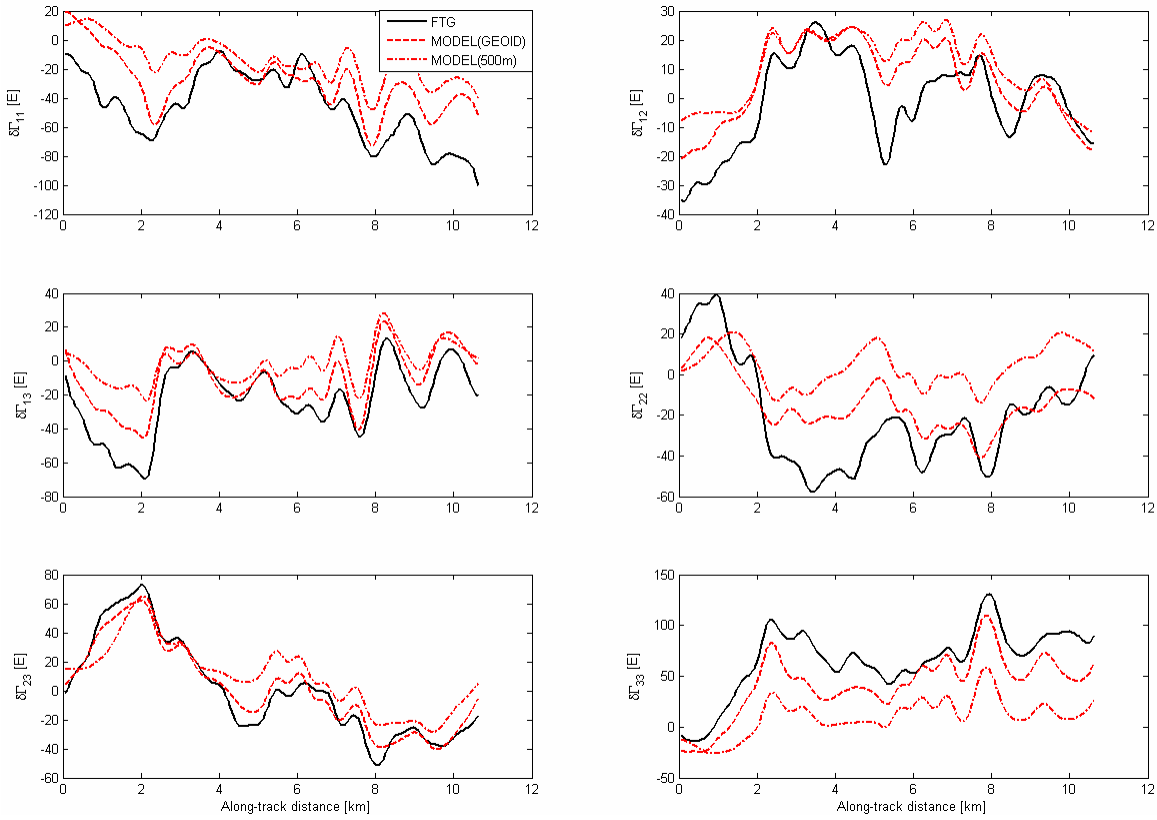

Figure 4.15: The modeled gradient disturbances using the geoid and 500 m mean elevation surface as reference surface and FTG data on Profile 2.

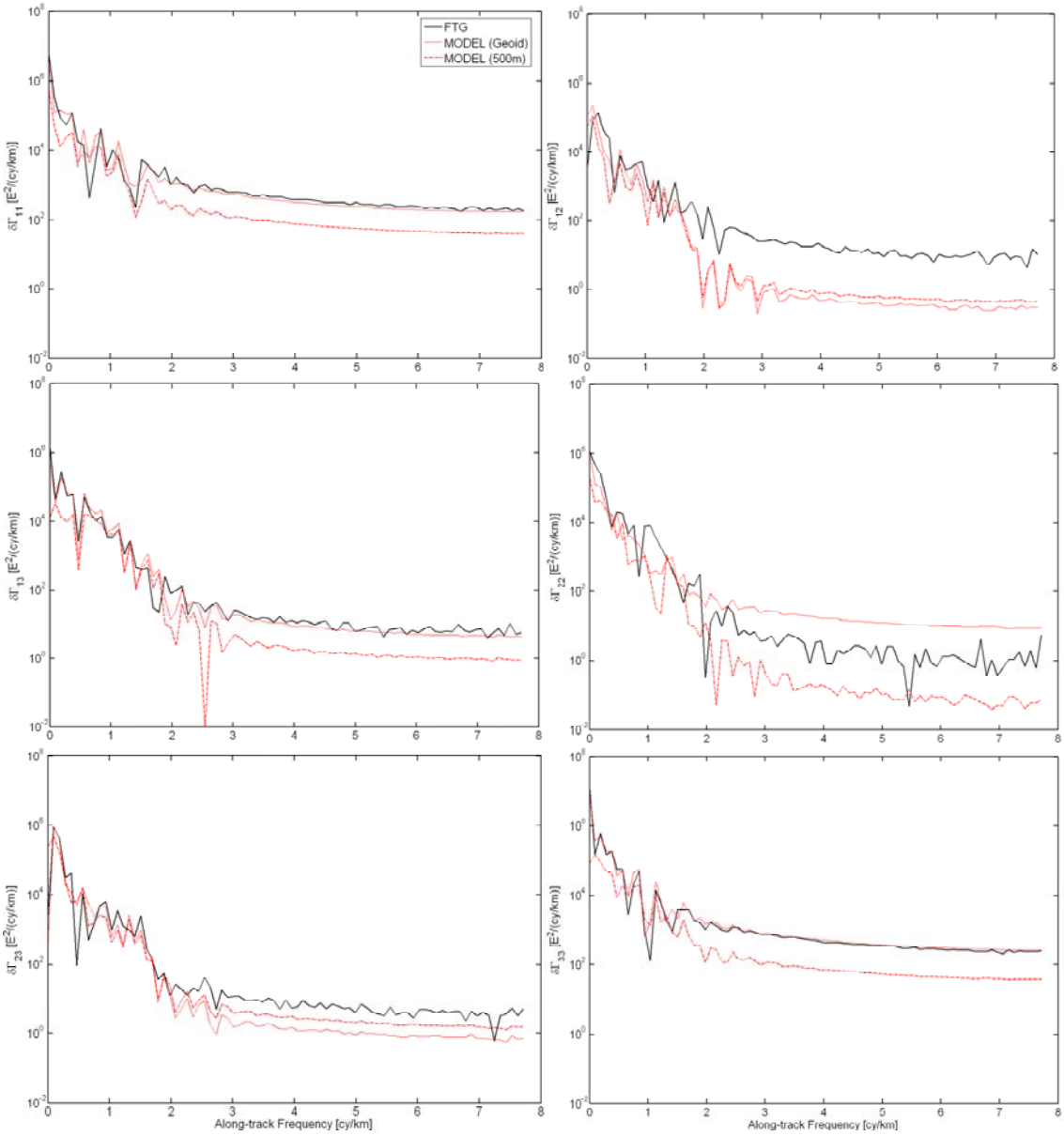

Figure 4.16: The PSD of modeled gradient disturbances using the geoid and 500 m elevation surface as reference and FTG data on Profile 2.

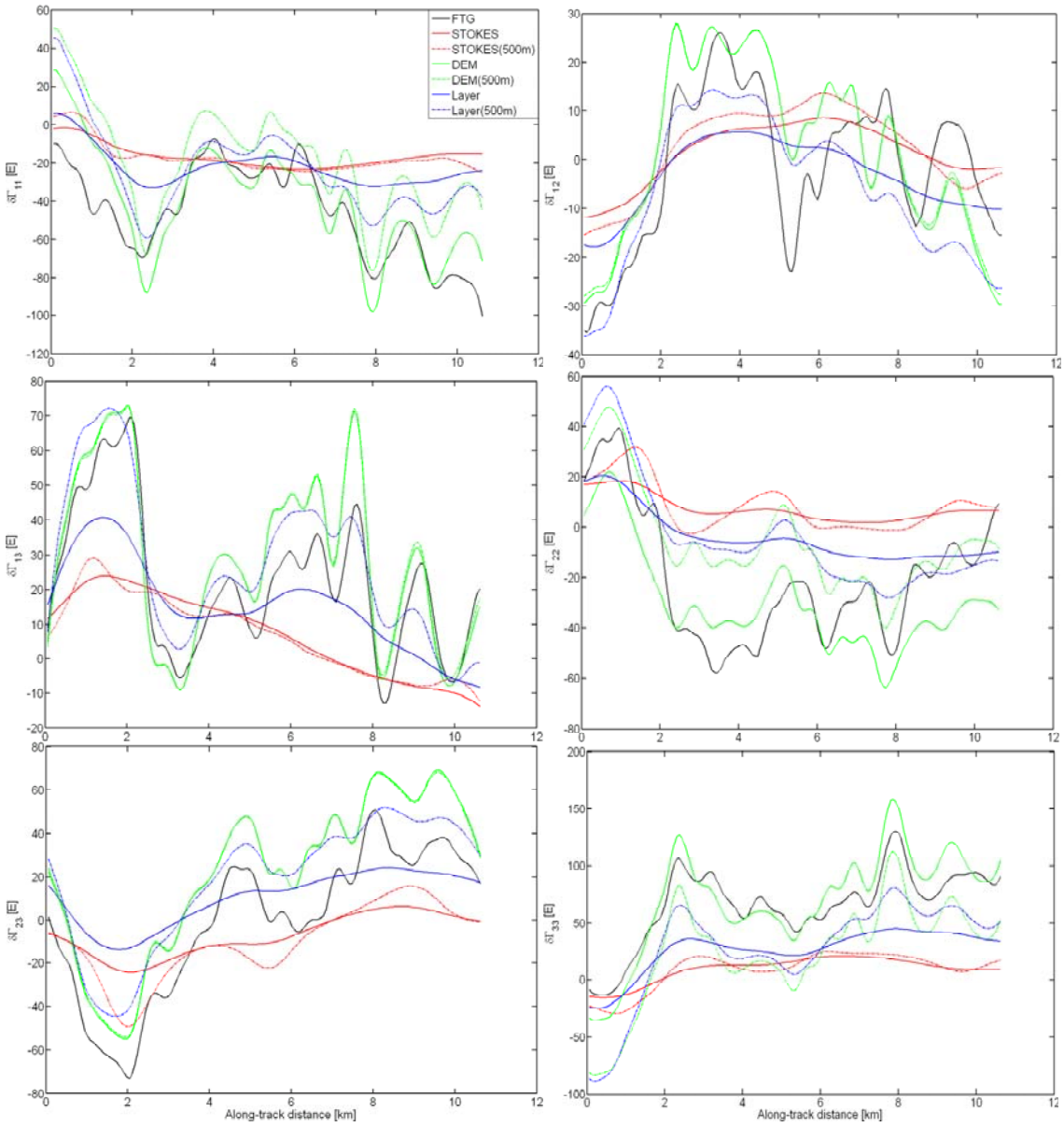

Figure 4.17: Components of gradient model using different reference surfaces.

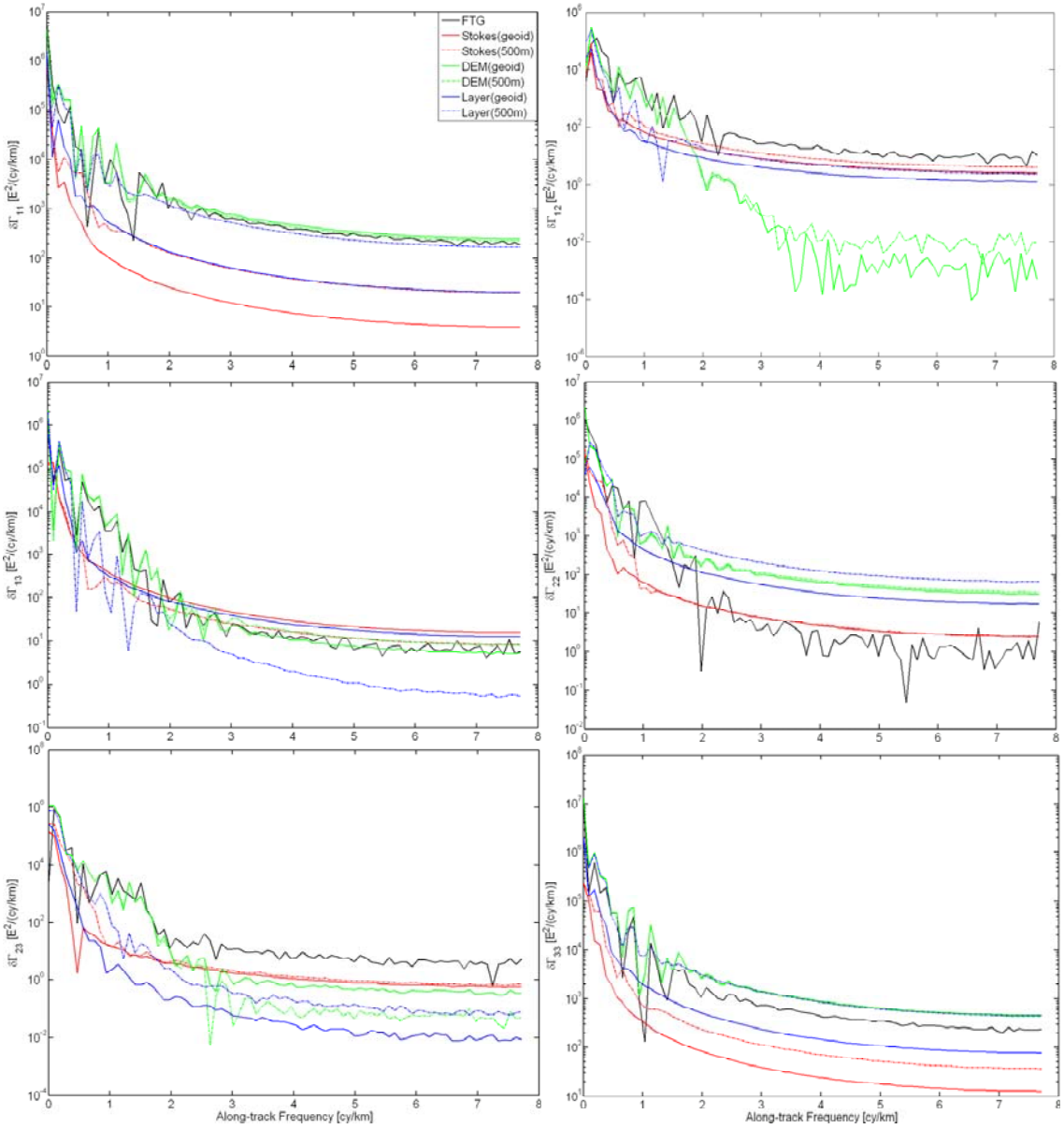

Figure 4.18: PSDs of components of gradient model using different reference surfaces.

4.6 Along track spectral analysis of gradient signal

4.6.1 Spectral analysis of DEM-derived gradient with density variation

Since most of gradient signal is generated by the DEM, we consider some future analysis on the basic assumption of constant density and how this affects the modeled

gradients at altitude. We used a DEM with both randomly varied density and with solved-for density contrasts to compute the implied gravity gradients on the profile 2.

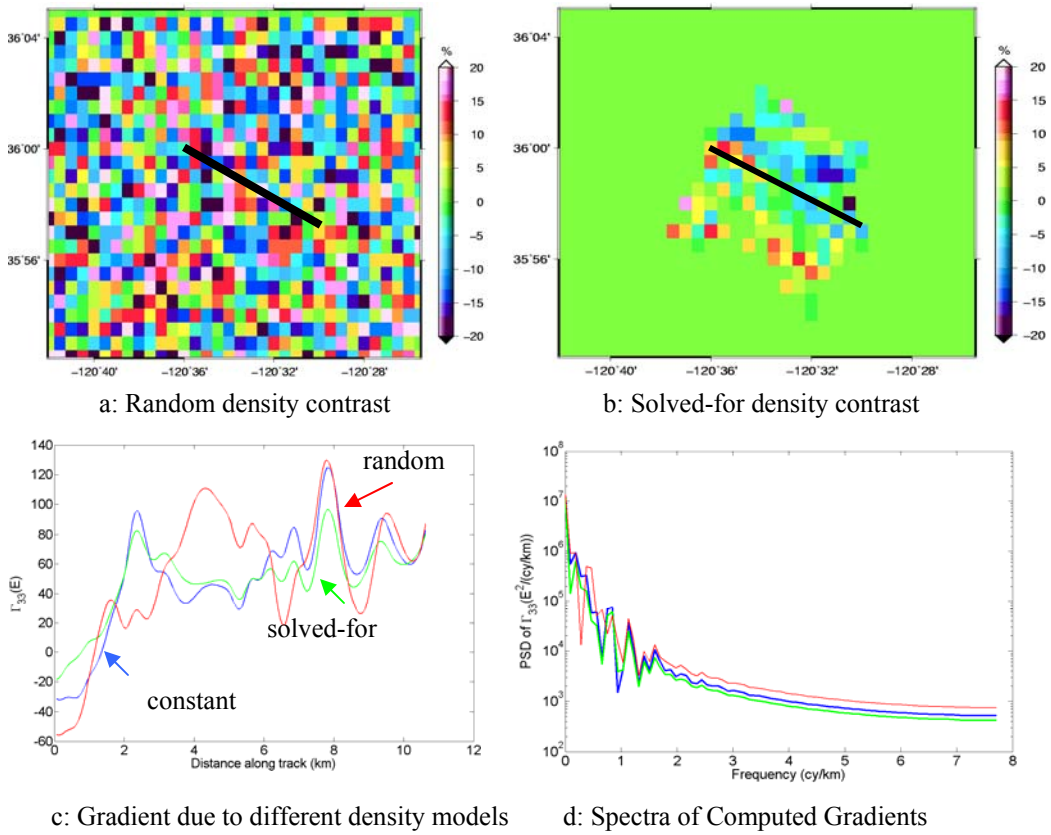

a: Random density contrast

b: Solved-for density contrast

c: Gradient due to different density models

d: Spectra of Computed Gradients

Figure 4.19: Variable vs. Constant Density DEM.

Figure 4.19 shows the varied density contrast distributions within topographic mass, the Γ_{33} gradient computed using these density distributions, and the PSD of this gradient due to different density distributions. Figure 4.19a is a random density contrast, and Figure 4.19b is the density contrast solved using Bell Geospace FTG data. Figure 4.19c gives us the different gradient signals due to the different density contrast distributions. From this, we find that the gradient due to topographic mass with the solved-for density contrast differs from the gradient due to topographic mass with constant density contrast by about 10E-30E, but the gradient due to topographic mass with random density contrast differs from the other two cases by about 20-70 E. Figure 4.19d shows that the energy of gradient due to the density contrast distributions in each case only focuses on the frequencies below 2 cy/km because the upward continuation attenuates the effects of variable density contrasts on the DEM-derived gradients.

4.6.2 Spectral analysis of gravity-derived gradients

Considering the medium resolution (2km) of the gravity anomaly data of the previous modeling test, we made another test in an area (Figure 4.20) in southern California where available gravity anomaly data have higher resolution (200m). A 32km test profile with 35m sampling interval was designed at altitude of 400m above the mean elevation along the profile. The gravity disturbances were computed using Stokes' integral method on the basis of residual gravity anomalies (removing EGM96 from Faye anomalies). Figure 4.21 and Figure 4.22 respectively give the modeled residual gradient disturbances and their power spectral densities (PSDs). It is shown that even from high resolution data, the PSDs of modeled gradients are concentrated below the frequencies of 2 cy/km because of the attenuation of upward continuation on the gradient disturbances. The magnitude of the PSD is between 10^{1} and $10^{7}\ E^2/(cy/km)$ while the PSD for DEM-derived gradients shown in Figure 4.19 is between 10^{2} and $10^{7}\ E^2/(cy/km)$. According to both test results, we may arrive at the conclusion that significant spectral content (PSD>$10^{2}\ E^2/(cy/km)$) of the modeled gradients at aircraft altitude (approx. 400 m above mean terrain) appears to be limited to about 2-3 cy/km (300-500 m resolution). This conclusion is essentially independent of the mass density function, and is upheld when using very high resolution in gravity data. These two results agree with results shown in Figure 4.16. It indicates the error in $\delta\Gamma_{22}^{FTG}$ exists largely because its PSD has bigger variations above the frequencies of 3 cy/km.

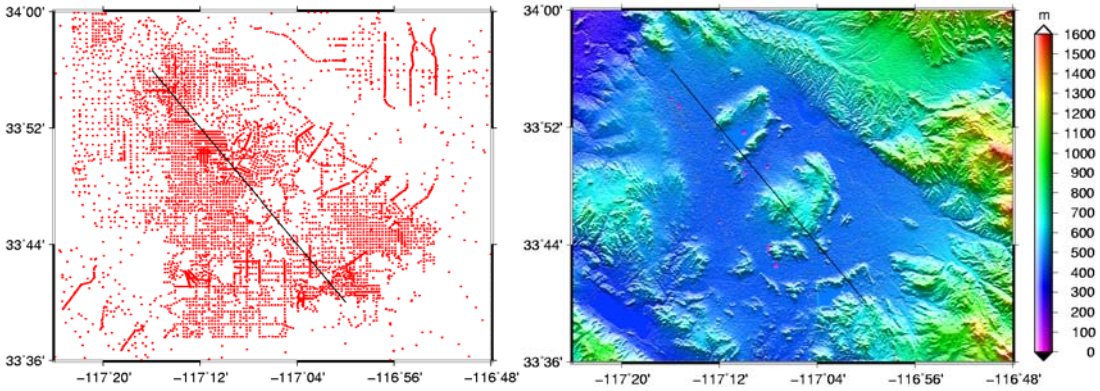

Figure 4.20: Gravity anomaly data and the DEM in a second area of southern California with test profile indicated by the black line.

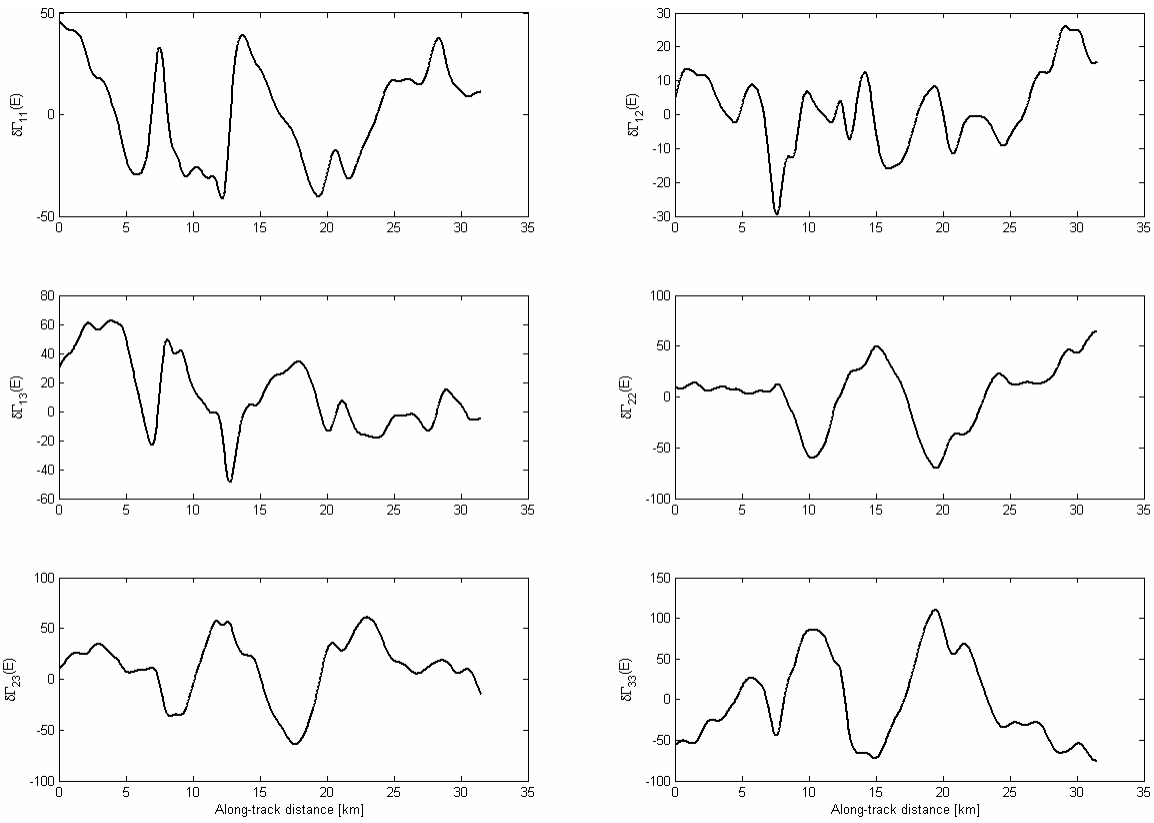

Figure 4.21: Residual gradient disturbances on the test profile in the southern California.

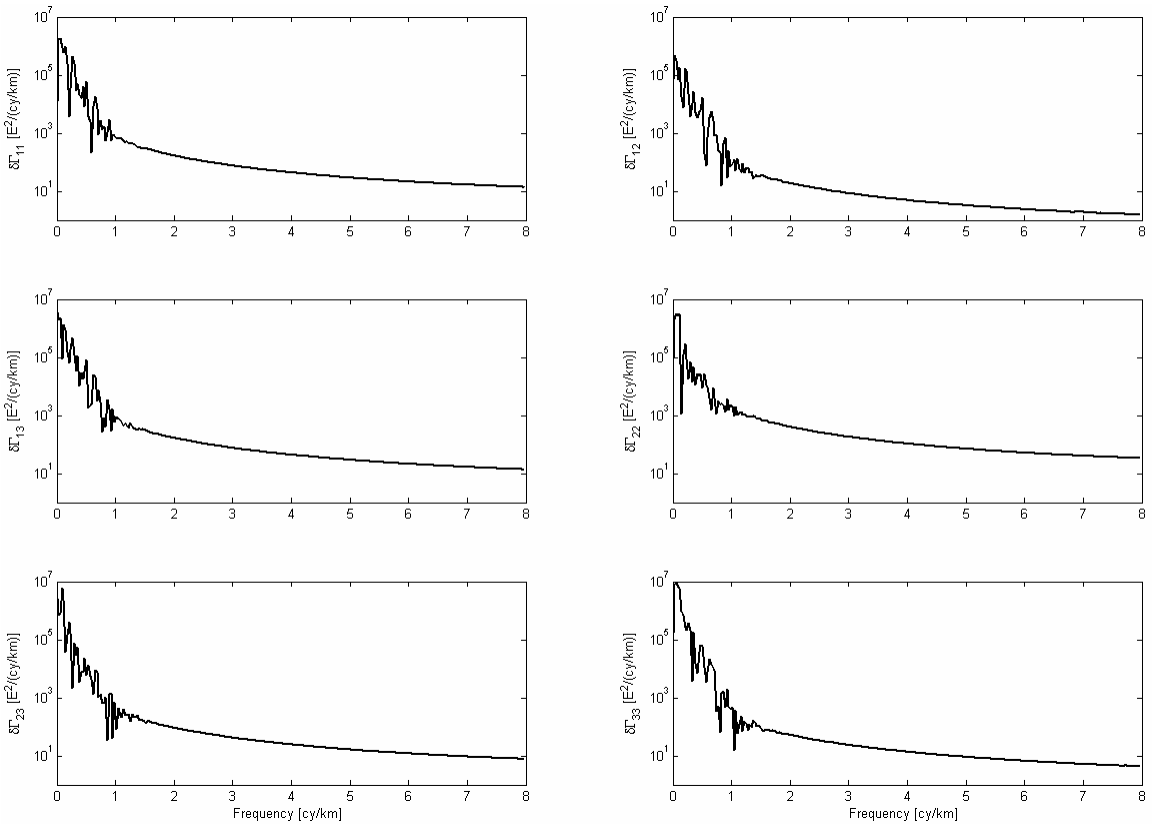

Figure 4.22: Spectra of gradient disturbances along the test profile in the southern California.

4.7 Conclusion

We have developed a consistent gradient disturbance model from the combination of gravity anomaly and DEM data. Through the remove-restore technique applied to the terrain reduction and the Helmert condensation procedure, we can determine the gradient disturbances at altitude. The cross-over point analysis of the FTG data consistently yields its internal accuracy at ±8 E level. We modeled the gravity gradient and compared it to actual FTG data. The results show differences between them are as large as 10-20 E.

Stokes' integral models the larger wavelengths of the gradient disturbances and DEM can be used to model the shorter wavelengths of the gradient disturbances. Clearly, as it is well known, the upward continuation acts as a low-pass filter. The comparison between the gradients due to a constant density and a varied density topographic mass shows that high-frequency variations in density do not affect the high-frequency spectrum of the gradients at altitude. The energy of gradients due to each density distribution only focuses on the frequencies below 2 cy/km, due to the attenuation of upward continuation.

Knowing the cut-off of this natural filter of the signal, airborne gradiometer systems can be better tuned with appropriate filters to remove high frequency errors due to aircraft dynamics and other systematic sources. For example, the airborne gradiometer survey over the San Andreas fault area (as indicated) needs to implement a 500 m filter as part of its data processing. Conversely, any significant spectral content (PSD>10^2 $E^2/(cy/km)$) in such airborne gradiometer data with frequencies higher than 2 cy/km is suspected as being erroneous.

The model incorporated the geoid or the mean topographic surface as the reference for heights and gravity anomalies. All quantity reductions refer to this reference. Choosing the geoid as the reference yields better results with respect to the FTG data than choosing the 500 m mean surface because the change of layer effect is much larger than the changes of gravity-derived gradients and topographic effect when the reductions refer to the mean elevation surface. The changes of all quantities due to the change of reference surface are not consistent in this case.

CHAPTER 5

CONCLUSIONS

In this study we developed the forward gravity gradient model based on gravity and DEM data for the purpose of validating an airborne or ground gradiometry survey. This study generally includes two parts, one is to generate the gradient disturbances due to topographic masses, and the other is to determine gradient disturbances from gravity data. Usually the density of topographic masses is assumed constant since the density information is largely unknown or in poor resolution. Since the gradients are more sensitive to the local topography, the flat-earth approximation is applied on the topography data. Finite elements (right rectangular prisms), including the polyhedral method, as well as direct numerical integration and two FFT-methods are used to determine the gradient disturbances due to the topographic masses represented by the DEM. Petrovic's polyhedral method depends on the triangulation of the data points, where the Delauny triangulation could be the best to represent the characteristics of the DEM. Parker's FFT method yields large errors when compared to the numerical integral and the right rectangular prism methods due to its analytical representation of the Fourier transform. Forsberg's method converges to the numerical integral method as the order of the corresponding Taylor series expansion increases. The extent of the DEM is also considered showing that 30 arcmin is necessary to achieve 1 E accuracy for a rough topographic area with 2000 m variations in the terrain elevation. The reference surface can be a constant mean elevation surface, or a spherical harmonic mean elevation surface. Choosing a different constant reference surface only impacts the in-line gradients, not cross gradients. The topographic masses enclosed by a spherical harmonic elevation surface smoothly affect the gradients in a local area by a few Eötvös. The analysis of these methods shows that the right rectangular prism and the numerical integration methods should be used to compute the DEM-derived gravity gradient, while Forsberg's FFT method is an efficient way if many points of computation are needed and the computation altitude is constant.

Since we neglect the density anomaly existing in the topographic masses, we need to compensate it using other data. Gravity anomalies reflect the mass anomalies in the topography and below the geoid, so the gradient disturbances determined by gravity anomalies also reflect the masses anomalies. The gravity-derived gradient disturbances are based on solving the boundary value problem of the potential field. We developed three different methods to model the gradient disturbances from gravity anomalies. Among these, Stokes' integral and least-squares collocation have the same level of accuracy when compared to the true data generated from a synthetic field. In the case of

computing gradients at the altitude of 1200 m using 1 arcmin simulated gravity anomaly data, the modeled gradients achieve ±3 E accuracy when compared to the "true" simulated gradients. Furthermore, the spherical generalized Stokes function can be simplified using a planar approximation. The error due to this simplification is of the order of 0.1 E or smaller. The accuracy of the Stokes' integral method at low altitude is worse than that at high altitude due to the low resolution of the gravity anomaly data. Since the singularity of Stokes integral at ground level is very strong, in this case the gradients are evaluated by the numerical differentiation of gravity anomaly. The least-squares collocation method is slightly more accurate than Stokes' integral method for the lower computation altitude. A numerical investigation on the model parameters based on the comparison of Stokes' integral and synthetic field data was carried out. The results verify that altitude, data spacing and magnitude are critical factors that one needs to take account into account in the gravity gradient model. Generally, the accuracy of the modeled gradients depends on the resolution of gravity data and the computation altitude.

Besides these three methods, spherical wavelets can also be used to model gradients from gravity data. The wavelet functions are separated for different frequency bands using banded Legendre coefficients, but the spherical spline glues all bands together with a converged series of numbers being Legendre coefficients. The wavelet modeling is also based on the Stokes' integral. The only difference is the way of computing the gradient in the spectral domain, instead of the spatial domain. The wavelet modeling can help us understand how the gradient signal is composed from different spectral bands. It might aid us to formulate a procedure to smooth and analysis the real gradiometry survey. However, this type of modeling was considered outside the present scope of investigation.

The gradient disturbances so far are separately modeled from DEM and gravity data; we need to combine them together in a consistent model. Starting from the reduction of gravity anomalies, we remove the terrain effect from free-air anomalies, and apply the Helmert condensation procedure to restore the terrain mass on the geoid as a condensed layer. This process yields Faye anomalies; and we then refer them to EGM96 and obtain residual Faye anomalies, which are used to model the residual gradient disturbances. After that, we restore the terrain effect, remove the layer effect and include the EGM96 model in order to get the final gradient disturbances. This mechanism was applied to model the gradient disturbances over an area of the San Andreas fault. The actual gradient disturbance (FTG) data from Bell Geospace were used to assess the gradient model. An analysis of the cross-over points of the FTG data shows that the internal accuracy of the FTG data is about 8 E. The difference of modeled data and FTG data is between 10 E and 20 E, which also indicates the accuracy of FTG data to some extent. A spectral analysis of DEM-derived gradients and high-resolution gravity-derived gradients shows that the significant spectral content of the modeled gradients at 400 m aircraft altitude above the terrain appears to be limited to about 2-3 cy/km (300-500 m resolution). Similarly, the potential high-frequency variation in the density of the DEM masses has no impact on the high-frequency gradient signal at the flight altitude. This conclusion can lead to more appropriate low-pass filters to process the airborne gravity gradient measurement. Also a study on gradient modeling with respect to the mean elevation surface shows that the Helmert condensation on the mean surface is not as good as on geoid. The layer effects are highly amplified on a reference surface closer to the

measurement surface and yields much worse results than if the geoid is the reference surface.

Further developments need to be carried out to validate a gradiometer system practice. One may need higher resolution data for both gravity and DEM. Using terrain structures with known density anomalies can be used to test the forward model with respect to the real FTG data. However, the method of gradient modeling using both gravity and DEM can be implemented for optimum comparisons.

REFERENCES

Agarwal, B.N.P. and Lal, T., 1972, A generalized method of computing second derivative of gravity field: Geophysical Prospecting, 20, 385-394.

Albertella A, F. Migliaccio, F. Sansò, 2002, GOCE: The Earth Field by Space Gradiometry: Celestial Mechanics and Dynamical Astronomy, 83:1-15.

Arabelos, D. and C.C. Tscherning, 1998, Calibration of satellite gradiometer data aided by ground data: Journal of Geodesy, 72:617-625.

Asgharzadeh, M. F., R. R. B. von Frese, H. R. Kim, T. E. Leftwich, J. W. Kim , 2007, Spherical prism gravity effects by Gauss-Legendre quadrature integration: Geophysical Journal International, 169 (1), 1–11. doi:10.1111/j.1365-246X.2007.03214.x.

Asten, Michael W., 2000, A technical review of the FALCON AIRBORNE gravity gradiometer: Technical Consultant's report, Section 6, Gravity Capital Limited, http://www.gravitydiamonds.com.au/masten.pdf.

Balmino G., F. Perosanz, R. Rummel, N. Sneeuw, H. Sünkel, P. Woodworth, 1998, European Views on Dedicated Gravity Field Missions: GRACE and GOCE, An Earth Sciences Division Consultation Document, ESA, ESD-MAG-REP-CON-001.

Bell Geospace, 2004, Final report of acquisition and processing on Air-FTG survey in Parkfield earthquake experiment area, September 2004, Rice University, Houston, Texas.

Bod, L., Fischbach, E., Marx G. and NÁRAY-ZIEGLE, M., 1990, One hundred years of the Eotvos experiment, http://www.kfki.hu/eotvos/onehund.html.

Bracewell, R., 1965, The Fourier transform and its applications, McGraw-Hill, New York.

Chinnery, M.A., 1961, Terrain corrections for airborne gravity gradient measurements: Geophysics, 26, No. 4, P. 480-489.

Cordell, L. and Henderson, R. G., 1968, Iterative three-dimensional solution of gravity anomaly data using digital computer: Geophysics, vol. 33, No. 4, P. 596-601.

Dampney, C.N.G., 1969, The equivalent source technique: Geophysics, Vol. 34, No. 1, P. 39-53.

Dransfield, M.H., 1994, Airborne Gravity Gradiometry: Doctoral Dissertation, Department of Physics, University of Western Australia, Australia.

Dyn, N., Levin, D. and Rippa, S., 1989, Algorithms for the constrcution of data dependent triangulations, in Algorithms for Approximation II, eds Cox, M.G. &Mason, J.C. Clarendon Press, Oxford, pp.185-192.

Forsberg, R., 1984, A study of terrain reductions, density anomalies and geophysical inversion methods in gravity field modeling, Report 355, Department of Geodetic Science and Surveying, The Ohio State University.

Forsberg, R., 1985, Gravity field terrain effect computations by FFT: Bull. Geod, 59, 342-260.

Forsberg, R., 1987, A new covariance model for inertial gravimetry and gradiometry, J.G.R., Vol. 92, No. B2, 1305-1310.

Freeden, W., 1981, On spherical spline interpolation and approximation, Math. Methods Appl. Sci., 3, 551-575.

Freeden, W. 1987, A spline interpolation method for solving boundary value problems of potential theory from discretely given data: Numer. Methods Partial Differential Equations, 3, 375-398.

Freeden, W., Gervens, T., and Schreiner, M., 1998, Constructive approximation on the sphere, with applications in Geomathematics, Clarendon Press, Oxford.

Freeden, W., and Schneider, F., 1998, An integrated wavelet concept of physical geodesy: Journal of Geodesy, 72, 259-281.

Gunn, P.J., 1975, Linear transformations of gravity and magnetic fields: Geophysical Prospecting, 23, 300–312.

Haagmans, R., de Min, E., and van Gelderen, M., 1993, Fast evaluation of convolution integrals on the sphere using 1D FFT, and a comparison with existing methods for Stokes' integral: Manuscripta Geodaetica, 18(5), 227-241.

Hammond, S. and Murphy, C., 2003, Air-FTG: Bell Geospace's Airborne Gravity Gradiometer- A Description and Case Study: http://www.bellgeo.com/products/air.html.

Heiskanen, W.A. and Moritz, H., 1967, Physical Geodesy: W. H. Freeman and Co., San Francisco.

Jekeli, C., 1988, The Gravity Gradiometer Survey System (GGSS): EOS, Transactions of the American Geophysical Union, v. 69, p. 105, 116–117.

Jekeli, C.,1998, Error analysis of padding schemes for DFT's of convolutions and derivatives, Report No.446, Geodetic Science, Ohio State University, Columbus, Ohio.

Jekeli, C., 2003. Statistical analysis of moving-base gravimetry and gravity gradiometry, Report No.466,Geodetic Science, Ohio State University, Columbus, Ohio.

Jekeli, C., 2005, Spline representations of functions on a sphere for geopotential modeling: Report No.475, Department of Civil and Environmental Engineering and Geodetic Science, The Ohio State University.

Jekeli, C. and L. Zhu, 2006, Comparison of methods to model the gravitational gradients, from topographic data bases: Geophysical Journal International, 166, 999-1014.

Jekeli, C., 2005, Fourier Geodesy, Lecture notes, Department of Civil Environmental Engineering and Geodetic Science, Ohio State University, Columbus, Ohio.

Koop, R., P.Visser, and C.C. Tscherning, 2001, Aspects of GOCE Calibration: Proceedings Int. GOCE Users Workshop, ESTEC, 23-24 April, 2001.

Lee, J.B., 2001, Falcon gravity gradiometer technology: Exploration Geophysics, 32,247-250.

Lemoine, F.G. et al., 1998. The development of the joint NASA GSFC and the National Imagery and Mapping Agency (NIMA) geopotential model EGM96, NASA Technical Paper NASA/TP-1998-206861, Godard Space Flight Center, Greenbelt.

Li, X, and Chouteau, M., 1998, Three-dimensional gravity modeling in all space: Surveys in Geophysics, 19: 339-368.

Li, X., 2001, Vertical resolution: gravity versus vertical gravity gradient: The Leading Edge, 20, no.8, 901-904.

Loncarevic, B. D., Best, M. E., and Kanters, W. A., 1992, Modeling of gravity anomalies in three dimensions using nonlinear optimization: Canadian Journal of Exploration Geophysics, Vol. 28, No. 2, P. 81-95.

Matthews, R., 2002, Mobile Gravity Gradiometer: PhD Thesis, Department of Physics, University of Western Australia.

Mautz, R., Schaffrin, B., Kaschenz, J., 2005, Biharmonic Spline Wavelets versus Generalized Multi-quadrics for Continuous Surface Representations, in: A Window on the Future of Geodesy, International Association of Geodesy Symposia, Vol. 128, pp.500-505.

Mickus, K.L. and Hinojosa, J.H., 2001, The complete gravity gradient tensor derived from the vertical component of gravity: a Fourier transform technique: Journal of Applied Geophysics, 46, 159-174.

Moritz, H., 1978, Least-square collocation: Reviews of geophysics, Vol. 16, No.3, 421-430.

Nagy, D., Papp, G., and Benedeck, J., 2000, The gravitational potential and its derivatives for the prism: Journal of Geodesy, 74, 552-560.

Papp, G., 1996, Gravity field approximation based on volume element model of the density distribution: Acta Geod. Geoph. Hung., 31, 339-358.

Parker, R.L., 1972, The rapid calculation of potential anomalies: Geophysical Journal of. the Royal Astronomical Society, v.42, 315-334

Petrovic, S., 1996, Determination of the potential of homogeneous polyhedral bodies using line integrals: Journal of Geodesy, 71, 44-52.

Quak, E. and Schumaker, L.L., 1990, Cubic spline fitting using data dependent triangulations: Computer Aided Geometric Design, 7, 293-301.

Rodriguez, E., C.S. Morris, J.E. Belz, E.C. Chapin, J.M. Martin, W. Daffer, S. Hensley, 2005, An assessment of the SRTM topographic products, Technical Report JPL D-31639, Jet Propulsion Laboratory, Pasadena, California, 143 pp.

Roland, M. and Denker, H., 2005, Stokes integration versus wavelet techniques for regional geoid modeling: International Association of Geodesy Symposia, 128, Springer Berlin, pp. 368-373.

Rummel, R., 1997, Spherical Spectral Properties of the Earth's Gravitational Potential and its First and Second Derivatives. In: Geodetic Boundary Value Problems in View of the One Centimeter Geoid, eds.: F. Sansò and R. Rummel, Lecture Notes in Earth sciences 65, pp. 359–404.

Salem, A., Ravat, D., Mushayandebvu, M.F. and Ushijima, K., 2004, Linearized least-squares method for interpretation of potential-field data from sources of simple geometry: Geophysics, Vol. 69, No. 3, P. 783-788.

Schmidt, M., Fabert, O. and C.K. Shum, 2002, Multi-Resolution Representation of the Gravity Field Using Spherical Wavelets: Proc. Weikko A. Heiskanen Symposium In Geodesy: Celebrating 50 years in Geodetic Science at the Ohio State University, eds.: C. Jekeli and C. Shum, The Ohio State University, Columbus, Ohio.

Schreiner,M., 1997, Locally supported kernel for spherical spline interpolation: Journal

of Approximation theory, Volume 89, No.2, pp.172-194.

Schwarz, K.P., Sideris, M.G. and Forsberg, R., 1990, The use of FFT techniques in physical geodesy: Geophysical Journal International, 100, 485-514.

Smith, D.A., Robertson, D.S. & Milbert, D.G., 2001. Gravitational attraction of local crustal masses in spherical coordinates: Journal of Geodesy, 74**,** 783–795.

Strykowski, G., 1998, Experiences with a detailed estimation of the mass density contrasts and of the regional gravity field using geometrical information from seismograms: Phys. Chem. Earth, 23, No. 9, pp. 845-856.

Sünkel, H. (ed.) (2002). http://www.inas.tugraz.at/forschung/e2mgp/e2mgp_fr.pdf . From Eötvös to mGal+, Final Report, ESA/ESTEC Contract No. 14287/00/NL/DC.

Talwani, M., 2004, Airborne Gravity Gradiometer Survey over the San Andreas Fault: Eos Trans. AGU 85(47), Fall Meet. Suppl., Abstract T13A-1348.

Toth, G., 1996, Topographic-isostatic models fitting to the global gravity field: Acta Geod. Geoph. Hung., Vol. 31(3-4), pp. 411-421.

Toth, G. and Volgyesi, L., 2003, Importance of Eotvos Torsion Balance measurements and their geodetic applications: Geophysical Research Abstracts, Vol. 5, 13217.

Tryggvason, B., Brian M. and Barry F., 2004, A high resolution airborne gravimeter and airborne gravity gradiometer, in R.J.L. Lane, editor, Airborne Gravity 2004 Abstracts from the ASEG-PESA Airborne Gravity 2004 Workshop: Geoscience Australia Record 2004/18, 41-44.

Tscherning, C.C. (1976): Covariance Expressions for Second and Lower Order Derivatives of the Anomalous Potential, Reports of the Department of Geodetic Science No. 225, The Ohio State University, Columbus, Ohio.

Tscherning, C.C., R. Forsberg, and P. Knudsen (1992): The GRAVSOFT Package for Geoid Determination: Proceedings First Workshop on the European Geoid, Prague, May, 1992.

Tsoulis, D., 1999, Spherical harmonic computations with topographic/isostatic coefficients, Reports in the series IAPG / FESG (ISSN 1437-8280), Rep. No. 3 (ISBN 3-934205-02-X), Institute of Astronomical and Physical Geodesy, Technical University of Munich, 33 pp.

Tsoulis, D., 2001, Terrain correction computations for a densely sampled DTM in the Bavarian Alps: Journal of Geodesy, 75, 291– 307.

Tsoulis, D., 2003, Terrain modeling in forward gravimetric problems: a case study on

local terrain effects: Journal of Applied Geophysics 54, 145-160.

Tsoulis, D. and Petrovic, S., 2001, On the singularities of the gravity field of a homogeneous polyhedral body: Geophysics, 66(2), 535-539.

Tziavos, I.N., Sideris, M.G., Forsberg, R. and Schwarz, K. P., 1988, The effect of the terrain on airborne gravity and gradiometry: J. G. R., 93, 9173-9186.

Tziavos, I.N, Sideris, M.G., and Sünkel, H., 1996, The effect of surface density variations terrain modelling - a case study in Austria: Report 96.2, Finnish Geodetic Institute, 99-110.

USGS, 2006, Shuttle Radar Topography Mission (SRTM)-"Finished", http://eros.usgs.gov/.

van Kann, F., 2004, Requirements and general principles of airborne gravity gradiometers for mineral exploration, in R.J.L. Lane, editor, Airborne Gravity 2004 Abstracts from the ASEG-PESA Airborne Gravity 2004 Workshop: Geoscience Australia Record 2004/18, 1-5.

Wahba, G., 1981, Spline interpolation and smoothing on the sphere: SIAM J. Sci. Stat. Comput. 2, 5-16, also errata, SIAM J. Sci. Stat. Comput., 3,385-386.

Wahba, G. 1984, Surface fitting with scattered noisy data on Euclidean d-space and on the sphere: Rocky Mountain J. Math., 14, 281-299.

Wang, Y. and Rapp, R., 1990, Terrain effects on geoid undulation computation: Manuscripta geodaetica, 15, 23-29.

Xu, P., 1998, Truncated SVD methods for discrete linear ill-posed problems: Geophysical Journal International, 135, 505-514.

Zhu, L and. Jekeli, C., 2007, Combining Gravity and Topographic Data for Local Gradient Modeling. In: Tregoning, P. and Rizos, C.(eds.), Dynamic Planet, IAG Symposium, Cairns, Australia, 22-26 August, 2005, Springer Verlag, p.288-295.

Zieliński, J. B. and M. S. Petrovskaya, 2003, The possibility of the calibration/validation of the GOCE data with the balloon-borne gradiometer: Adv. Geosci., 1, 149-153.

APPENDIX A

THE RELATION OF THE PARTIAL DERIVATIVES

Since Stokes' function is in terms with r and ψ, we need to transform the derivatives of Stokes' function with respect to spherical coordinates to its derivatives with respect to r and ψ. This part describes this relation. As shown in Figure 3.1, the relations between the polar coordinates, ψ, α, and the spherical coordinates, $\theta, \lambda, \theta', \lambda'$ are given (Heiskanen and Moritz, 1967),

$$\cos\psi = \cos\theta\cos\theta' + \sin\theta\sin\theta'\cos(\lambda - \lambda'), \tag{A.1}$$

$$\cot\alpha = \frac{\sin\theta\cos\theta' - \cos\theta\sin\theta'\cos(\lambda' - \lambda)}{\sin\theta'\sin(\lambda' - \lambda)}, \tag{A.2}$$

and

$$\sin\alpha = \frac{\sin(\lambda' - \lambda)\sin\theta'}{\sin\psi}. \tag{A.3}$$

Taking the derivative with respect to λ on both sides of (A.1), we get

$$-\sin\psi\frac{\partial\psi}{\partial\lambda} = -\sin\theta\sin\theta'\sin(\lambda - \lambda'), \tag{A.4}$$

$$\frac{\partial\psi}{\partial\lambda} = \frac{\sin\theta\sin\theta'\sin(\lambda - \lambda')}{\sin\psi} = -\sin\theta\sin\alpha. \tag{A.5}$$

Taking the derivative with respect to λ on both sides of (A.4), we get

$$\cos\psi\left(\frac{\partial\psi}{\partial\lambda}\right)^2 + \sin\psi\frac{\partial^2\psi}{\partial\lambda^2} = \sin\theta\sin\theta'\cos(\lambda - \lambda'). \tag{A.6}$$

Therefore, we have

$$\begin{aligned}\frac{\partial^2\psi}{\partial\lambda^2} &= \frac{\sin\theta\sin\theta'\cos(\lambda - \lambda') - \cos\psi\sin^2\theta\sin^2\alpha}{\sin\psi} \\ &= \sin\theta\frac{\sin\theta'\cos(\lambda - \lambda') - \cos\psi\sin\theta}{\sin\psi} + \cot\psi\sin^2\theta\cos^2\alpha\end{aligned}. \tag{A.7}$$

Since we have

$$\sin\theta'\cos(\lambda' - \lambda) = \cos\psi\sin\theta - \cos\alpha\cos\theta\sin\psi, \tag{A.8}$$

inserting (A.8) into (A.7), we have

$$\frac{\partial^2\psi}{\partial\lambda^2} = \sin\theta\frac{-\cos\alpha\cos\theta\sin\psi}{\sin\psi} + \cot\psi\sin^2\theta\cos^2\alpha \quad . \tag{A.9}$$
$$= \cot\psi\sin^2\theta\cos^2\alpha - \cos\alpha\sin\theta\cos\theta$$

Taking the derivative with respect to θ on both sides of (A.1), we get

$$-\sin\psi\frac{\partial\psi}{\partial\theta} = -\sin\theta\cos\theta' + \cos\theta\sin\theta'\cos(\lambda-\lambda') \,, \tag{A.10}$$

$$\frac{\partial\psi}{\partial\theta} = \frac{\sin\theta\cos\theta' - \cos\theta\sin\theta'\cos(\lambda-\lambda')}{\sin\psi} = \cos\alpha \,. \tag{A.11}$$

Taking the derivative with respect to θ on both sides of (A.10), we have

$$-\cos\psi\left(\frac{\partial\psi}{\partial\theta}\right)^2 - \sin\psi\frac{\partial^2\psi}{\partial\theta^2} = -\cos\theta\cos\theta' - \sin\theta\sin\theta'\cos(\lambda-\lambda') \quad . \tag{A.12}$$
$$= -\cos\psi$$

Furthermore, we get

$$\frac{\partial^2\psi}{\partial\theta^2} = \cot\psi - -\cot\psi\left(\frac{\partial\psi}{\partial\theta}\right)^2 = \cot\psi(1-\cos^2\alpha) \quad . \tag{A.13}$$
$$= \cot\psi\sin^2\alpha$$

Taking the derivative with respect to λ on both sides of (A.10), we have

$$\cos\psi\frac{\partial\psi}{\partial\theta}\frac{\partial\psi}{\partial\lambda} + \sin\psi\frac{\partial^2\psi}{\partial\theta\partial\lambda} = \cos\theta\sin\theta'\sin(\lambda-\lambda') \,, \tag{A.14}$$

$$\frac{\partial^2\psi}{\partial\theta\partial\lambda} = \frac{\cos\theta\sin\theta'\sin(\lambda-\lambda') + \cos\psi\cos\alpha\sin\alpha\sin\theta}{\sin\psi} \quad . \tag{A.15}$$
$$= \cot\psi\cos\alpha\sin\alpha\sin\theta - \cos\theta\sin\alpha$$

Taking the derivative with respect to θ on both sides of (A.2), we get

$$-\csc^2\alpha\frac{\partial\alpha}{\partial\theta} = \frac{\cos\theta\cos\theta' + \sin\theta\sin\theta'\cos(\lambda'-\lambda)}{\sin\theta'\sin(\lambda'-\lambda)} \,. \tag{A.16}$$

Inserting (A.2) into (A.16), we have

$$\frac{\partial\alpha}{\partial\theta} = -\frac{\cos\psi\sin^2\alpha}{\sin\alpha\sin\psi} = -\cot\psi\sin\alpha \,. \tag{A.17}$$

Taking the derivative with respect to θ on both sides of (A.17), we get

$$\frac{\partial^2\alpha}{\partial\theta^2} = \csc^2\psi\frac{\partial\psi}{\partial\theta}\sin\alpha - \cot\psi\cos\alpha\frac{\partial\alpha}{\partial\theta}$$
$$= \csc^2\psi\cos\alpha\sin\alpha - \cot\psi\cos\alpha(-\cot\psi\sin\alpha) \,. \tag{A.18}$$
$$= (\csc^2\psi + \cot^2\psi)\cos\alpha\sin\alpha$$

Taking the derivative with respect to λ on both sides of (A.2), we have

$$\cos\psi\frac{\partial\psi}{\partial\lambda}\sin\alpha + \sin\psi\cos\alpha\frac{\partial\alpha}{\partial\lambda} = -\cos(\lambda'-\lambda)\sin\theta' \,. \tag{A.19}$$

Inserting (A.5) and (A.8) into (A.19), we have

$$\frac{\partial\alpha}{\partial\lambda}=\frac{\cos\psi\sin\theta\sin^2\alpha-\cos\psi\sin\theta+\cos\alpha\cos\theta\sin\psi}{\cos\alpha\sin\psi}. \tag{A.20}$$
$$=\cos\theta-\cot\psi\sin\theta\cos\alpha$$

Taking the derivatives with respect to λ on both sides of (A.20), we get

$$\frac{\partial^2\alpha}{\partial\lambda^2}=\sin\theta\cos\alpha\csc^2\psi\frac{\partial\psi}{\partial\lambda}+\sin\theta\cot\psi\sin\alpha\frac{\partial\alpha}{\partial\lambda}. \tag{A.21}$$

Inserting (A.5) and (A.20) into (A.21), we have

$$\frac{\partial^2\alpha}{\partial\lambda^2}=\sin\theta\cos\theta\cot\psi\sin\alpha-\sin^2\theta\cos\alpha\sin\alpha\left(\csc^2\psi+\cot^2\psi\right). \tag{A.22}$$

Taking the derivative with respect to θ on both sides of (A.20), we get

$$\frac{\partial^2\alpha}{\partial\lambda\partial\theta}=-\sin\theta+\csc^2\psi\frac{\partial\psi}{\partial\theta}\sin\theta\cos\alpha-\cot\psi\cos\theta\cos\alpha+\cot\psi\sin\theta\sin\alpha\frac{\partial\alpha}{\partial\theta}$$
$$=-\sin\theta+\csc^2\psi\sin\theta\cos^2\alpha-\cot\psi\cos\theta\cos\alpha+\cot^2\psi\sin\theta\sin^2\alpha \tag{A.23}$$
$$=\cot^2\psi\sin\theta-\sin\theta\sin^2\alpha-\cot\psi\cos\theta\cos\alpha$$

Now we need the derivatives with respect to the spherical coordinates. We have

$$\frac{\partial}{\partial\lambda}=\frac{\partial}{\partial\psi}\frac{\partial\psi}{\partial\lambda}+\frac{\partial}{\partial\alpha}\frac{\partial\alpha}{\partial\lambda}, \tag{A.24}$$

and

$$\frac{\partial^2}{\partial\lambda^2}=\frac{\partial\left(\frac{\partial}{\partial\psi}\frac{\partial\psi}{\partial\lambda}+\frac{\partial}{\partial\alpha}\frac{\partial\alpha}{\partial\lambda}\right)}{\partial\lambda}$$
$$=\frac{\partial^2\psi}{\partial\lambda^2}\frac{\partial}{\partial\psi}+\frac{\partial\psi}{\partial\lambda}\left(\frac{\partial}{\partial\psi}\left(\frac{\partial}{\partial\psi}\right)\frac{\partial\psi}{\partial\lambda}+\frac{\partial}{\partial\alpha}\left(\frac{\partial}{\partial\psi}\right)\frac{\partial\alpha}{\partial\lambda}\right) \tag{A.25}$$
$$+\frac{\partial^2\alpha}{\partial\lambda^2}\frac{\partial}{\partial\alpha}+\frac{\partial\alpha}{\partial\lambda}\left(\frac{\partial}{\partial\psi}\left(\frac{\partial}{\partial\alpha}\right)\frac{\partial\psi}{\partial\lambda}+\frac{\partial}{\partial\alpha}\left(\frac{\partial}{\partial\alpha}\right)\frac{\partial\alpha}{\partial\lambda}\right)$$
$$=\frac{\partial^2\psi}{\partial\lambda^2}\frac{\partial}{\partial\psi}+\frac{\partial^2\alpha}{\partial\lambda^2}\frac{\partial}{\partial\alpha}+\left(\frac{\partial\psi}{\partial\lambda}\right)^2\frac{\partial^2}{\partial\psi^2}+\left(\frac{\partial\alpha}{\partial\lambda}\right)^2\frac{\partial^2}{\partial\alpha^2}+2\left(\frac{\partial^2}{\partial\psi\partial\alpha}\right)\frac{\partial\psi}{\partial\lambda}\frac{\partial\alpha}{\partial\lambda}$$

Similarly, one can get

$$\frac{\partial}{\partial\theta}=\frac{\partial}{\partial\psi}\frac{\partial\psi}{\partial\theta}+\frac{\partial}{\partial\alpha}\frac{\partial\alpha}{\partial\theta}, \tag{A.26}$$

$$\frac{\partial^2}{\partial\theta^2}=\frac{\partial^2\psi}{\partial\theta^2}\frac{\partial}{\partial\psi}+\frac{\partial^2\alpha}{\partial\theta^2}\frac{\partial}{\partial\alpha}+\left(\frac{\partial\psi}{\partial\theta}\right)^2\frac{\partial^2}{\partial\psi^2}+\left(\frac{\partial\alpha}{\partial\theta}\right)^2\frac{\partial^2}{\partial\alpha^2}+2\left(\frac{\partial^2}{\partial\psi\partial\alpha}\right)\frac{\partial\psi}{\partial\theta}\frac{\partial\alpha}{\partial\theta}, \tag{A.27}$$

and

$$\frac{\partial^2}{\partial\theta\partial\lambda}=\frac{\partial^2\psi}{\partial\theta\partial\lambda}\frac{\partial}{\partial\psi}+\frac{\partial^2\alpha}{\partial\theta\partial\lambda}\frac{\partial}{\partial\alpha}+\left(\frac{\partial\psi}{\partial\theta}\frac{\partial\psi}{\partial\lambda}\right)\frac{\partial^2}{\partial\psi^2}+\left(\frac{\partial\alpha}{\partial\theta}\frac{\partial\alpha}{\partial\lambda}\right)\frac{\partial^2}{\partial\alpha^2}$$
$$+\left(\frac{\partial^2}{\partial\psi\partial\alpha}\right)\left(\frac{\partial\psi}{\partial\lambda}\frac{\partial\alpha}{\partial\theta}+\frac{\partial\psi}{\partial\theta}\frac{\partial\alpha}{\partial\lambda}\right) \tag{A.28}$$

Inserting (A.5) and (A.20) into (A.24), one has

$$\frac{\partial}{\partial \lambda} = -\sin\theta \sin\alpha \frac{\partial}{\partial \psi} + \left(\cos\theta - \cot\psi \sin\theta \cos\alpha\right) \frac{\partial}{\partial \alpha}. \tag{A.29}$$

Inserting (A.5), (A.7), (A.9) and (A.22) into (A.25), one gets

$$\begin{aligned} \frac{\partial^2}{\partial \lambda^2} &= \sin^2\theta \sin^2\alpha \frac{\partial^2}{\partial \psi^2} + \left(\cot\psi \sin^2\theta \cos^2\alpha - \cos\alpha \sin\theta \cos\theta\right) \frac{\partial}{\partial \psi} \\ &-2\sin\theta \sin\alpha (\cos\theta - \cot\psi \sin\theta \cos\alpha) \frac{\partial^2}{\partial \psi \partial \alpha} + (\cos\theta - \cot\psi \sin\theta \cos\alpha)^2 \frac{\partial^2}{\partial \alpha^2}. \\ &+\left(\sin\theta \cos\theta \cot\psi \sin\alpha - \sin^2\theta \cos\alpha \sin\alpha \left(\csc^2\psi + \cot^2\psi\right)\right) \frac{\partial}{\partial \alpha} \end{aligned} \tag{A.30}$$

Similarly, using (A.9), (A.11), (A.17), (A.18), (A.20) and (A.21), we have

$$\frac{\partial}{\partial \theta} = \cos\alpha \frac{\partial}{\partial \psi} - \cot\psi \sin\alpha \frac{\partial}{\partial \alpha}, \tag{A.31}$$

$$\begin{aligned} \frac{\partial^2}{\partial \theta^2} &= \cot\psi \sin^2\alpha \frac{\partial}{\partial \psi} + \cos^2\alpha \frac{\partial^2}{\partial \psi^2} + (\csc^2\psi + \cot^2\psi) \cos\alpha \sin\alpha \frac{\partial}{\partial \alpha} \\ &+\cot^2\psi \sin^2\alpha \frac{\partial^2}{\partial \alpha^2} - 2\cos\alpha \cot\psi \sin\alpha \frac{\partial^2}{\partial \psi \partial \alpha} \end{aligned}, \tag{A.32}$$

and

$$\begin{aligned} \frac{\partial^2}{\partial \theta \partial \lambda} &= \left(\cot\psi \cos\alpha \sin\alpha \sin\theta - \cos\theta \sin\alpha\right) \frac{\partial}{\partial \psi} - \sin\theta \sin\alpha \cos\alpha \frac{\partial^2}{\partial \psi^2} \\ &+\left(\cot^2\psi \sin\theta - \sin\theta \sin^2\alpha - \cot\psi \cos\theta \cos\alpha\right) \frac{\partial}{\partial \alpha} \\ &-\cot\psi \sin\alpha \left(\cos\theta - \cot\psi \sin\theta \cos\alpha\right) \frac{\partial^2}{\partial \alpha^2} \\ &+\left(\cot\psi \sin\theta (\sin^2\alpha - \cos^2\alpha) + \cos\alpha \cos\theta\right) \frac{\partial^2}{\partial \psi \partial \alpha} \end{aligned} \tag{A.33}$$

Also we get

$$\frac{\partial^2}{\partial \lambda \partial r} = -\sin\theta \sin\alpha \frac{\partial^2}{\partial r \partial \psi} \tag{A.34}$$

and

$$\frac{\partial^2}{\partial \theta \partial r} = \cos\alpha \frac{\partial^2}{\partial \psi \partial r} \tag{A.35}$$

APPENDIX B

The GRADIENT DISTURBANCES FROM EGM96

The global spherical harmonic gravitational model, EGM96 (Lemoine et al., 1998) is a low degree model that we use it as a reference to model the local gradient disturbances. Here we introduce the gradient disturbance model from EGM96. The disturbing potential corresponding to the EGM96 model at point, (r,θ,λ) is given by

$$T^{egm}(r,\theta,\lambda)=\frac{GM}{R}\sum_{n=2}^{360}\sum_{m=0}^{n}\left(\frac{R}{r}\right)^{n+1}\left(C_{nm}\cos m\lambda+S_{nm}\sin m\lambda\right)\overline{P}_{nm}\left(\cos\theta\right), \tag{B.1}$$

where GM is Newton's gravitational constant times Earth's total mass, R is the mean Earth radius, C_{nm} and S_{nm} are the disturbing potential coefficients of EGM96, $\overline{P}_{nm}$ are the normalized associated Legendre function.

Letting $T_{nm}=\left(\frac{R}{r}\right)^{n+1}\left(C_{nm}\cos m\lambda+S_{nm}\sin m\lambda\right)\overline{P}_{nm}\left(\cos\theta\right)$, from (3.7) we get the gradient disturbance:

$$\Gamma_{11}^{egm}=\frac{\partial^2 T_{egm}}{\partial x_1^2}=\frac{GM}{R}\sum_{n=2}^{360}\sum_{m=0}^{n}\left(\frac{1}{r}\frac{\partial T_{nm}}{\partial r}+\frac{1}{r^2}\frac{\partial^2 T_{nm}}{\partial\theta^2}\right),$$

$$\Gamma_{12}^{egm}=\frac{\partial^2 T_{egm}}{\partial x_1\partial x_2}=\frac{GM}{R}\sum_{n=2}^{360}\sum_{m=0}^{n}\left(-\frac{\cot\theta}{r^2\sin\theta}\frac{\partial T_{nm}}{\partial\lambda}+\frac{1}{r^2\sin\theta}\frac{\partial^2 T_{nm}}{\partial\theta\partial\lambda}\right),$$

$$\Gamma_{13}^{egm}=\frac{\partial^2 T_{egm}}{\partial x_1\partial x_3}=\frac{GM}{R}\sum_{n=2}^{360}\sum_{m=0}^{n}\left(-\frac{1}{r^2}\frac{\partial T_{nm}}{\partial\theta}+\frac{1}{r}\frac{\partial^2 T_{nm}}{\partial\theta\partial r}\right),$$

$$\Gamma_{22}^{egm}=\frac{\partial^2 T_{egm}}{\partial x_2^2}=\frac{GM}{R}\sum_{n=2}^{360}\sum_{m=0}^{n}\left(\frac{\cot\theta}{r^2}\frac{\partial T_{nm}}{\partial\theta}+\frac{1}{r}\frac{\partial T_{nm}}{\partial r}+\frac{1}{r^2\sin^2\theta}\frac{\partial^2 T_{nm}}{\partial\lambda^2}\right),$$

$$\Gamma_{23}^{egm}=\frac{\partial^2 T_{egm}}{\partial x_2\partial x_3}=\frac{GM}{R}\sum_{n=2}^{360}\sum_{m=0}^{n}\left(-\frac{1}{r^2\sin\theta}\frac{\partial T_{nm}}{\partial\lambda}+\frac{1}{r\sin\theta}\frac{\partial^2 T_{nm}}{\partial\lambda\partial r}\right),$$

$$\Gamma_{33}^{egm}=\frac{\partial^2 T_{egm}}{\partial x_3^2}=\frac{GM}{R}\sum_{n=2}^{360}\sum_{m=0}^{n}\left(\frac{\partial^2 T_{nm}}{\partial r^2}\right). \tag{B.2}$$

Because the highest degree of EGM96 is 360, which can only recover the signal with the resolution of 50 km, the gradient disturbance derived from EGM96 is very smooth over

local regions, behaving like a cyclic signal. The partial derivative of T_{nm} with respect to the spherical coordinates can be derived as follows,

$$\frac{\partial T_{nm}}{\partial r} = -\frac{n+1}{R}\left(\frac{R}{r}\right)^{n+2}\left(C_{nm}\cos m\lambda + S_{nm}\sin m\lambda\right)\overline{P}_{nm}\left(\cos\theta\right),$$

$$\frac{\partial T_{nm}}{\partial \theta} = \left(\frac{R}{r}\right)^{n+1}\left(C_{nm}\cos m\lambda + S_{nm}\sin m\lambda\right)\frac{d\overline{P}_{nm}\left(\cos\theta\right)}{d\theta},$$

$$\frac{\partial T_{nm}}{\partial \lambda} = m\left(\frac{R}{r}\right)^{n+1}\left(S_{nm}\cos m\lambda - C_{nm}\sin m\lambda\right)\overline{P}_{nm}\left(\cos\theta\right),$$

$$\frac{\partial^2 T_{nm}}{\partial \theta^2} = \left(\frac{R}{r}\right)^{n+1}\left(C_{nm}\cos m\lambda + S_{nm}\sin m\lambda\right)\frac{d^2\overline{P}_{nm}\left(\cos\theta\right)}{d\theta^2},$$

$$\frac{\partial^2 T_{nm}}{\partial \lambda^2} = -m^2\left(\frac{R}{r}\right)^{n+1}\left(C_{nm}\cos m\lambda + S_{nm}\sin m\lambda\right)\overline{P}_{nm}\left(\cos\theta\right),$$

$$\frac{\partial^2 T_{nm}}{\partial \lambda \partial \theta} = m\left(\frac{R}{r}\right)^{n+1}\left(S_{nm}\cos m\lambda - C_{nm}\sin m\lambda\right)\frac{d\overline{P}_{nm}\left(\cos\theta\right)}{d\theta},$$

$$\frac{\partial^2 T_{nm}}{\partial \lambda \partial r} = -\frac{m\left(n+1\right)}{R}\left(\frac{R}{r}\right)^{n+2}\left(S_{nm}\cos m\lambda - C_{nm}\sin m\lambda\right)\overline{P}_{nm}\left(\cos\theta\right),$$

$$\frac{\partial^2 T_{nm}}{\partial \theta \partial r} = -\frac{n+1}{R}\left(\frac{R}{r}\right)^{n+2}\left(C_{nm}\cos m\lambda + S_{nm}\sin m\lambda\right)\frac{d\overline{P}_{nm}\left(\cos\theta\right)}{d\theta},$$

$$\frac{\partial^2 T_{nm}}{\partial r^2} = \frac{\left(n+1\right)\left(n+2\right)}{R^2}\left(\frac{R}{r}\right)^{n+3}\left(C_{nm}\cos m\lambda + S_{nm}\sin m\lambda\right)\overline{P}_{nm}\left(\cos\theta\right), \tag{B.3}$$

where $\frac{d\overline{P}_{nm}(\cos\theta)}{d\theta}$ and $\frac{d^2\overline{P}_{nm}(\cos\theta)}{d\theta^2}$ are respectively the first and second derivative of Legendre functions, $\overline{P}_{nm}\left(\cos\theta\right)$, with respect to the variable θ. We start from the ordinary Associated Legendre functions. From

$$P_{nm}\left(\cos\theta\right) = \sin^m\theta\frac{d^m}{d\left(\cos\theta\right)^m}P_n\left(\cos\theta\right), \tag{B.4}$$

we have

$$\begin{aligned}&\frac{dP_{nm}(\cos\theta)}{d\theta}\\ &= m\sin^{m-1}\theta\cos\theta\frac{d^m}{d\left(\cos\theta\right)^m}P_n(\cos\theta) + \sin^m\theta\frac{d^{m+1}}{d\left(\cos\theta\right)^{m+1}}P_n(\cos\theta)\frac{d\left(\cos\theta\right)}{d\theta},\\ &= m\cot\theta P_{nm}(\cos\theta) - P_{n(m+1)}(\cos\theta)\end{aligned} \tag{B.5}$$

and

$$\frac{d^2 P_{nm}(\cos\theta)}{d\theta^2}$$
$$= -m\csc^2\theta P_{nm}(\cos\theta) + m\cot\theta\left(m\cot\theta P_{nm}(\cos\theta) - P_{n(m+1)}(\cos\theta)\right) \quad , \quad \text{(B.6)}$$
$$-\left(m+1\right)\cot\theta P_{n(m+1)}(\cos\theta) + P_{n(m+2)}(\cos\theta)$$
$$= P_{n(m+2)}(\cos\theta) - (2m+1)\cot\theta P_{n(m+1)}(\cos\theta) + \left(m^2\cot^2\theta - m\csc^2\theta\right)P_{nm}(\cos\theta)$$

Now we convert ordinary Legendre functions in (B.5) and (B.6) to the fully normalized Legendre function, $\overline{P}_{nm}(\cos\theta)$.

Since we have

$\overline{P}_{n0}(\cos\theta) = \sqrt{2n+1}P_{n0}(\cos\theta)$,

and $\overline{P}_{nm}\left(\cos\theta\right) = \sqrt{\frac{2\left(2n+1\right)\left(n-m\right)!}{\left(n+m\right)!}}P_{nm}\left(\cos\theta\right)$ for $m \neq 0$. (B.7)

substituting (B.7) into (B.5) and (B.6), we have

$$\frac{d\overline{P}_{n0}(\cos\theta)}{d\theta} = -\sqrt{\frac{\left(n+1\right)n}{2}}\overline{P}_{n1}(\cos\theta),$$
$$\frac{d^2\overline{P}_{n0}(\cos\theta)}{d\theta^2} = \sqrt{\frac{\left(n+2\right)\left(n+1\right)n\left(n-1\right)}{2}}\overline{P}_{n2}(\cos\theta) - \sqrt{\frac{\left(n+1\right)n}{2}}\cot(\theta)\overline{P}_{n1}(\cos\theta), \quad \text{(B.8)}$$
$$\frac{d\overline{P}_{nm}(\cos\theta)}{d\theta} = m\cot(\theta)\overline{P}_{nm}(\cos\theta) - \sqrt{\left(n+m+1\right)\left(n-m\right)}\overline{P}_{n(m+1)}(\cos\theta),$$
$$\frac{d^2\overline{P}_{nm}(\cos\theta)}{d\theta^2} = \sqrt{\left(n+m+2\right)\left(n+m+1\right)\left(n-m\right)\left(n-m-1\right)}\overline{P}_{n(m+2)}(\cos\theta)$$
$$-(2m+1)\cot\theta\sqrt{\left(n+m+1\right)\left(n-m\right)}\overline{P}_{n(m+1)}(\cos\theta) \quad , \text{for } m \neq 0 \quad \text{(B.9)}$$
$$+\left(m^2\cot^2\theta - m\csc^2\theta\right)\overline{P}_{nm}(\cos\theta)$$

Thus we can use normalized associated Legendre functions to derive the gradient according to (B.2).